PETRA IV.
NEW DIMENSIONS

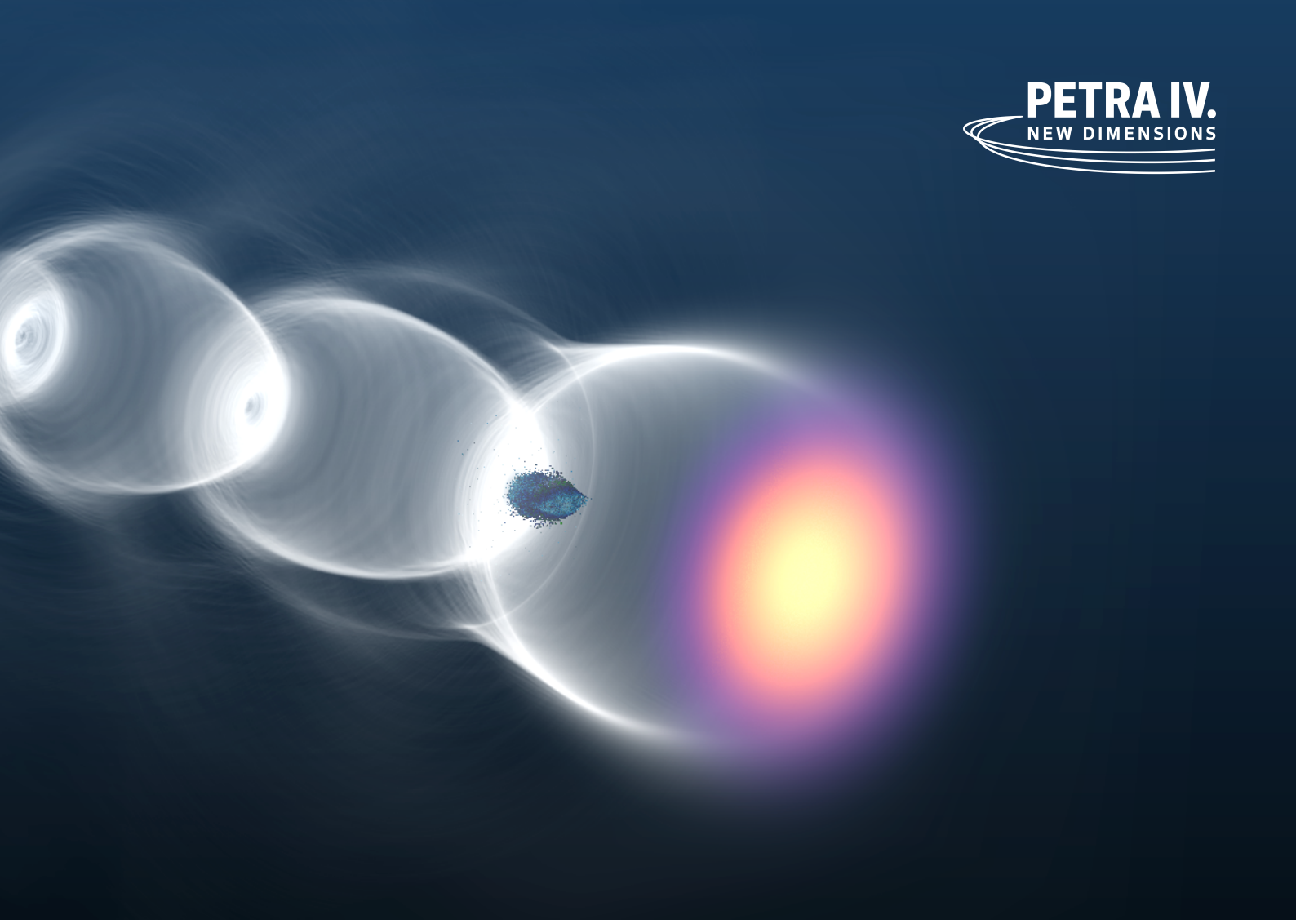

The Plasma Injector for PETRA IV.

Enabling Plasma Accelerators for Next-generation Light Sources
Conceptual Design Report

Deutsches Elektronen-Synchrotron DESY
A Research Centre of the Helmholtz Association

DESY.

Deutsches Elektronen-Synchrotron DESY

The Plasma Injector for PETRA IV

Enabling Plasma Accelerators for Next-generation Light Sources

Conceptual Design Report

Abstract

We present the conceptual design of an alternative injector system based on laser-plasma accelerator technology, to deliver high-quality electron bunches to PETRA IV – the future 4th generation synchrotron light source at DESY. The design consists of a laser-plasma accelerator to produce electron bunches at 6 GeV with state-of-the-art energy spread and stability (∼1%), and an X-band energy compressor beamline to further reduce the overall beam energy deviations down to a sub-permille level, thus maximizing the charge injection throughput into the PETRA IV storage ring. Driven by the Petawatt upgrade of DESY's new flagship laser KALDERA, the plasma injector system could be used to top up the PETRA IV storage ring, significantly lowering the load on the RF injector chain. Ultimately, upon further development of high-efficiency, high-power laser drivers that operate at high repetition rates, the plasma injector could replace the RF-based system in the future to reduce the spatial footprint and energetic cost of the whole injector complex.

List of Authors

Ilya Agapov (MPY), Sergey A. Antipov (MPY), Reinhard Brinkmann (MPY),
Ángel Ferran Pousa (MPA), Sören Jalas (MLS), Manuel Kirchen (MLS), Wim P. Leemans (M),
Andreas R. Maier (MLS), Alberto Martinez de la Ossa† (MPA), Jens Osterhoff (MPA),
Rob Shalloo (MPA), Maxence Thévenet (MPA), Paul Winkler (MLS).

†E-Mail: alberto.martinez.de.la.ossa@desy.de

Imprint

Deutsches Elektronen-Synchrotron DESY
Notkestraße 85, 22607 Hamburg, Germany
DOI: 10.3204/PUBDB-2024-06078
ISBN 978-3-945931-52-3

Submitted: October 18, 2023
Edition: February 12, 2025

Contents

1. Executive summary

PETRA IV will be the future flagship synchrotron light source at DESY [1], upgrading the beam quality of the current PETRA III by a factor 100 in emittance and enabling the production of photon beams with a spectral brightness between 100 to 1000 times higher than achievable today. Operating as a user facility for about 5000 hours per year, PETRA IV will allow thousands of scientists and engineers to conduct exceptional research in many diverse areas, ranging from physics, chemistry, biology and biomedicine to geological, environmental and materials sciences as well as nanoscience and technology. The transformative potential of PETRA IV is outstanding, guaranteeing world-class analytical opportunities for an interdisciplinary and international user community [2]. Thanks to the large circumference of the storage ring, PETRA IV is set to surpass all similar facilities currently planned or in operation, placing it in a prime position to drive scientific progress and innovation [3]. Moreover, the ambitions of PETRA IV extend beyond technical excellence; it will also integrate comprehensive sustainability concepts and foster the development of new technologies that can further enhance its capabilities in the future. As envisioned with DESY's *Moonshot* proposal [4], laser-plasma accelerator technology could notably decrease the spatial footprint and the power requirements of the PETRA IV injector complex and could, by doing so, contribute to a more affordable and sustainable operation of the world's primary analytical instrument.

Laser-plasma accelerators use highly intense laser pulses to generate large electric fields in plasma, suitable for the acceleration of electron bunches to multi-GeV energies over distances of only a few centimeters [5]. The laser-plasma accelerator (LPA) outperforms radio frequency (RF) technology in accelerating gradient by several orders of magnitude, and it has the potential to become a readily accessible and affordable source of high-energy electrons. Over the past two decades, LPAs have demonstrated remarkable progress in many important aspects, including achieving GeV energies [6–8], narrow energy spectra [9–11], and low emittances [12–15]. Furthermore, the march towards their practical usability has gained substantial momentum, with DESY taking a leading role in this endeavor [16–18]. This ongoing advancement strongly advocates considering LPAs as a practical alternative to RF particle accelerators, particularly for applications in free-electron lasers [19–23], and as injectors for storage rings [24, 25].

The demands placed on a plasma injector system to meet the high operational requirements of a world-class 4th generation synchrotron light source like PETRA IV are significant. A competitive injector system must be capable of providing 6 GeV electron beams with a narrow bandwidth while ensuring high reliability and availability. Furthermore, it must operate with high stability and at a relatively high repetition rate. Meeting these challenges presents a unique opportunity to leverage LPA technology for cutting-edge scientific applications, such as operating the brightest synchrotron radiation source worldwide. In this conceptual design of a Plasma Injector for PETRA IV (PIP4), we propose innovative solutions to address these challenges and enhance the LPA performance to the necessary levels.

To provide a high-quality 6 GeV beam that can be injected into the PETRA IV ring, a state-of-the-art LPA is needed. Specifically there are two key technologies that will be combined to achieve the required beam parameters: controlled beam injection and laser guiding. On the one hand, our design for the PIP4 builds upon successful LPA development at DESY (LUX) for controlled injection, to achieve the required beam quality [17, 18], reliability and operational performance [16]. On the other hand, to reach 6 GeV energy, we will guide the drive laser pulse using hydrodynamic optical-field-ionized (HOFI) plasma channels [26, 27]. This technique allows for the best laser-to-beam energy transfer efficiencies in the range of interest and is ideally

suited to LPAs operating at high repetition rates and for extended periods of time.

Another crucial aspect of the plasma injector is a stable performance at a relatively high repetition rate. The KALDERA project at DESY [28] sets the basis for the needed technological advance in this direction, aiming to develop a kHz laser system for plasma wakefield acceleration. The automatic control over the sources of drift and jitter [16] by means of active feedback methods, to be implemented in future high repetition LPAs, promises to deliver electron beams with sub-percent energy spread and jitter. Yet for the conceptual design of the plasma injector, we have considered a more conservative 1% level of energy spread and stability, achievable in state-of-the-art LPAs today. With the purpose of reducing the remaining energy fluctuations of the LPA beam and effectively increase the net charge injection throughput and stability into the PETRA IV storage ring, we have adopted for the design an energy compression and stabilization strategy, recently proposed for LPAs [29], that will enable unprecedented levels of relative energy spread and stability ($\sim 10^{-4}$). Such low energy bandwidth and high stability, joint to the comparably low emittance of the LPA beams, will allow for a clean and efficient injection into the storage ring.

Our conceptual design for PIP4 has been accurately simulated and benchmarked using state-of-the-art computing capabilities for precise modeling, and optimized with advanced machine-learning algorithms. Start-to-end simulations for a particular working point demonstrate the production of electron beams with 80 pC charge at 6 GeV with $< 0.1\%$-level energy deviations, by employing laser pulses in the 10–20 J energy range and considering the realistic jitters of the LPA. While these simulations showcase competitive beam parameters for injection, satisfying the high operational demands of PETRA IV for filling the storage ring at an average charge injection rate of 2.6 nC/s would require running the plasma injector at a relatively high repetition rate: 32 Hz. Higher bunch charges and thus lower repetition rates are possible with higher laser pulse energies. The development of a laser system capable to perform the rapid fillings of the ring is therefore central to achieve a competitive plasma injector for PETRA IV. Using KALDERA [28] as the foundation of the future drive laser for the plasma injector is a promising path that will allow us to save cost and benefit from an exceptional laser beam quality and a well-established operational performance.

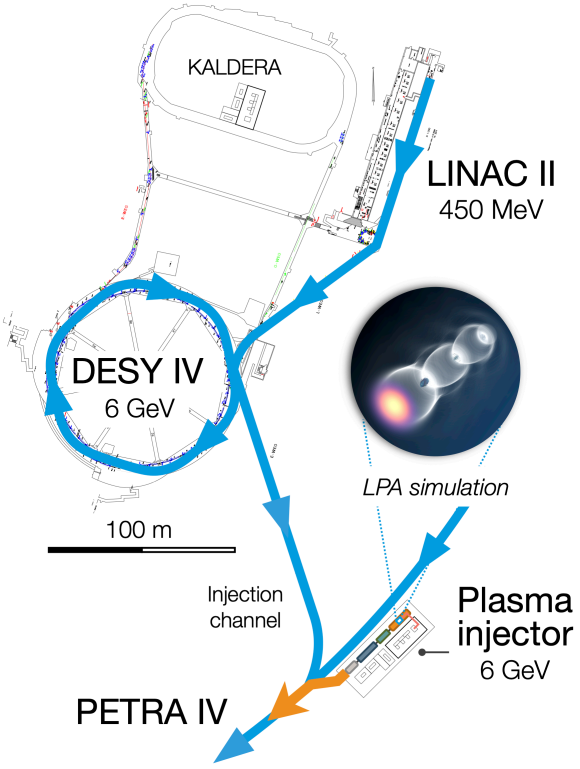

Figure 1. PIP4 conceptual schematic. Thanks to its compact footprint, the plasma injector can be located directly next to the ring, eliminating the need for an extended beam transport line. Alternative options, such as placing the plasma injector next to the current KALDERA facility, are also considered for near-term implementation. The footprint of the RF injector complex is also shown for comparison. It consists of a refurbished S-band linac (LINAC II) and a new booster ring (DESY IV).

Figure 1 depicts a possible schematic layout of the plasma injector. Located next to the storage ring, as enabled by its compact footprint, it would eliminate the need for an extended beam transport line. Other locations for the plasma injector are also being considered. For example, placing the plasma injector near the current KALDERA laser would seamlessly integrate the system with the main injection infrastructure and minimize the need for civil engineering interventions, thus enabling near-term implementation.

This innovative plasma injector system can be used to top up the PETRA IV storage ring, significantly lowering the load on the RF injector chain. Upon further devel-

opment of high-efficiency, high-power laser drivers that operate at high repetition rates, the plasma injector could replace the RF injector system in the future to reduce significantly the spatial footprint and the energetic cost of the whole injector complex.

This document is structured as follows. PETRA IV and the operation requirements of the injector system are described in Sec. 2. The core of the conceptual design of the plasma injector is Sec. 3, where a selected design solution for the PIP4 is described in detail with the support of start-to-end simulations. The expected performance and power consumption of the plasma injector are evaluated and compared with those of the RF injector. In Sec. 4, the roadmap for the implementation of the plasma injector is presented and discussed. Extended simulation details and additional supporting studies are reported in Appx. A. Appendix B is dedicated to a review of the most relevant aspects of the physics of LPAs for the purpose of this document.

2. PETRA IV

The PETRA ring at DESY was built in 1976-1978, originally as a positron-electron collider. It contributed to human understanding of particle physics with a breakthrough discovery of the gluon in 1979 [30]. Later, it served as a pre-accelerator for the proton-electron collider HERA [31], Germany's largest research instrument at the time. Nowadays the PETRA tunnel hosts a 3rd generation synchrotron light source PETRA III [32]. As a light source, it serves an international user community, covering a broad range of scientific fields, from physics [33, 34], chemistry [35, 36], material science [37, 38] to biology and medicine [39, 40]. Its key strength is in performing experiments in situ that provide insight into the dynamics of processes. Recent research activities at PETRA include massive drug screening searches for anti-viral drugs [41] and searches for synthetic nanobodies [42] during the SARS-CoV-2 pandemic.

PETRA IV will be the future upgrade of the ring to a 4th generation light source. Providing ultra-low-emittance electron beams at 6 GeV [1–3], PETRA IV will be a substantial upgrade in terms of beam quality (two orders of magnitude smaller beam emittance) with respect to the present machine. The exquisite beam quality and performance of PETRA IV will enable a new X-ray source with unprecedented spatio-temporal resolution, allowing for the analysis of material synthesis at the atomic level with the highest precision ever: PETRA IV will become the world reference in 3D X-ray microscopy, driving innovation and ground-breaking discoveries in health, energy, mobility, information technology, and earth and environment [1, 3].

The PETRA IV facility consists of the storage ring itself, its injector complex, and the photon science complex: beamlines and experiments [3]. The storage ring will provide electron beams for 30 few-meters-long undulator insertions (these photon beamlines can be further split to allow for more experimental stations), of which 16 will be hosted in the new Extension West hall (Fig. 2). The

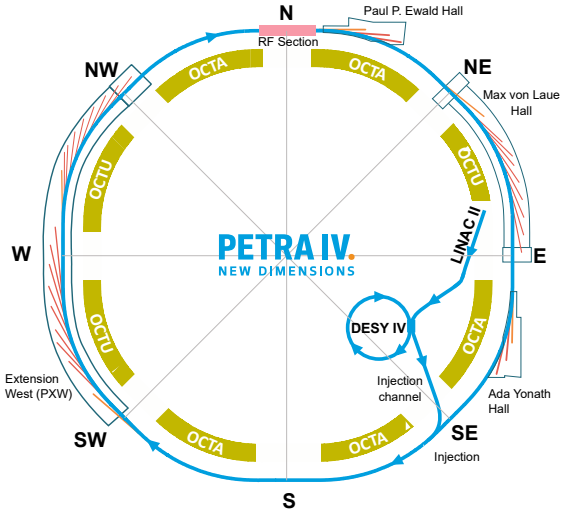

Figure 2. Layout of the PETRA IV facility. Existing experimental halls (Max von Laue, Peter P. Ewald, and Ada Yonath) will be reused. An additional experimental hall ("Extension West") will be constructed.

PETRA IV design employs a novel multi-bend achromat focusing lattice [43] to achieve the lowest possible beam emittance. With a horizontal (vertical) geometric emittance of 20 pm (4 pm), PETRA IV would reach the theoretical diffraction limit [44, 45] for production of X-rays up to 10 keV. PETRA IV is estimated to exceed PETRA III spectral brightness by about a factor 500 for 10 keV and by a factor 1000 for 60 keV photons [3].

Inheriting its geometry from the High Energy Physics programme of PETRA in the 1970s, the light source has a four-fold symmetry with eight arcs, four long straight sections of approximately 108 m in length, and four short straight sections of approximately 64 m in length (Fig. 2). Each arc is composed of nine specially designed hybrid six-bend achromat (H6BA) cells [46, 47]. The straight sections house injection, collimation, feedback, damping wiggler, and radiofrequency (RF) systems. Additionally, the unconventional geometry allows PETRA IV to host special 10-m-long, so-called 'Flagship', insertion devices in some of its long straight sections with a dedicated triplet optics to focus the beam into these insertions. The storage ring circumference totals to 2304 m (Tab. 1).

The optimized H6BA focusing lattice of PETRA IV features a remarkably large dynamic aperture and momentum acceptance. This results in a long Touschek lifetime [48] and high stability of the stored electron beam, enabling operation with off-axis injection and accumulation.

Design parameter	PETRA IV	
Energy / GeV	6	
Circumference / m	2304	
RF frequency / MHz	500	
	Brightness	**Timing**
Emittance (x/y) / pm	< 20/4	< 50/10
Number of bunches	1920	80
Bunch spacing / ns	4	96
Bunch charge / nC	0.8	8.0
Total charge / nC	1536	640
Beam current / mA	200	80
Beam lifetime / h	10	5

Table 1. PETRA IV storage ring and beam parameters.

The PETRA IV beam: The storage ring will operate in two modes: Brightness mode with 1920 stored bunches (4 ns spacing) and 200 mA average current, and Timing mode with 80 bunches (96 ns spacing) and 80 mA average current [46, 47], as shown in Tab. 1. The total stored charge is 1536 nC and 640 nC for Brightness and Timing modes, respectively. Other, non-baseline, operation modes are presently being considered, such as a 2-ns Brightness mode or a 40-bunch Timing mode.

2.1. Injection requirements

PETRA IV will utilize an off-axis accumulation injection scheme both for the initial filling and for compensating beam losses in operation. In an off-axis injection scheme, the bunches are not exchanged completely, but rather topped up by an accumulation process. As a consequence, the amount of charge that has to be provided by the injector per shot during the top-up can be rather low (a fraction of a bunch charge). A notable exception is the initial filling, when delivering the full bunch charge is beneficial for a rapid filling of the ring, thus increasing its availability for experiments.

Beam quality: In the standard off-axis accumulation injection procedure, the stored beam is moved by a closed kicker bump near the septum bar, thus moving part of the transverse acceptance of the ring across the bar and creating (phase) space for the newly injected bunch. The injected bunch then performs oscillations within the ring acceptance, which decay with a characteristic damping time of about $\tau_d = 20$ ms due to synchrotron radiation [46, 47]. Considering a transverse acceptance of 0.5 µm rad (Tab. 2), the total phase space volume available for the (off-axis) injected beam will be about 10 times smaller: 50 nm rad. This translates into a geometric (normalized) rms emittance requirement of < 1 nm rad (< 12 µm) for high injection efficiency[1]. Since the transverse acceptance drops with momentum deviation, the energy spread of the injected beam must stay well below the ring momentum acceptance: both the rms energy spread and the central energy jitter of the beam need to be at the per-mille level[2] to enable an efficient injection into the ring.

PETRA IV acceptance	Value	
Momentum acc.	2 %	
Transverse acc.	0.5 µm rad	
Beam parameter	**Requirement**	
Average energy	6 GeV	
Energy spread*	< 0.3 %	
Geom. emittance	< 1 nm rad	
Operation mode	**Injection rate**	
	Brightness	Timing
Initial filling	> 2.6 nC/s	> 1.1 nC/s
Top up	> 43 pC/s	> 36 pC/s

*including jitter.

Table 2. PETRA IV injection requirements.

Initial filling: The minimum required charge injection rate, $\mathcal{Q}_{\mathrm{inj}}^{\mathrm{min}}$, is determined by the ratio of the total charge to store initially in the ring, $\mathrm{Q}_{\mathrm{R},0}$, over the time required to fill the ring from scratch, $\mathrm{T}_{\mathrm{fill}}$,

$$\mathcal{Q}_{\mathrm{inj}}^{\mathrm{min}} = \mathrm{Q}_{\mathrm{R},0}/\mathrm{T}_{\mathrm{fill}}\,. \tag{2.1}$$

Typically, operating PETRA IV at the desired performance prescribes filling times no larger than 10 minutes, otherwise the machine availability will be reduced by 1% or

[1] High injection efficiency requires that both the rms beam size and divergence is 7 times smaller than the available geometrical aperture. This condition implies that the beam rms geometric emittance was 49 times smaller that the available phase-space area.

[2] The rms spread in beam energy is required to be 7 times smaller than the acceptance.

more just by the time to inject the beam every time the machine has to be refilled[3]. Considering the Brightness (Timing) operation mode, filling the ring in less than 10 minutes requires a charge injection rate higher than 2.6 (1.1) nC/s (Tab. 2).

Top-up operation: Once the ring has been filled, new charge needs to be injected to compensate for the losses from (mainly) Touschek scattering of the stored beam. We refer to this process of injecting new charge as *top-up* operation. For top-up operation we need to consider the beam lifetime, τ_b. The charge stored in the ring decays over time according to

$$Q_R(t) = Q_{R,0} \exp(-t/\tau_b). \quad (2.2)$$

Thus, after a time $T_{1\%} = -\ln 0.99\,\tau_b$, the initial beam charge is reduced by 1%. Current simulations with the new lattice design for PETRA IV [46, 47] yield a beam lifetime of 10 (5) hours in the Brightness (Timing) mode of operation (Tab. 1): 1% of the charge is lost every 6 (3) minutes in Brightness (Timing) mode. Hence, the average charge injection rate during top-up operation should be at least 43 (36) pC/s in Brightness (Timing) mode (Tab. 2).

Injection sequence: Considering a relatively low charge per injector shot, Q_s, in comparison with the total bunch charge stored in PETRA IV, Q_B, the different PETRA IV beam modes need to be built up following an accumulation process. The circumference of PETRA IV spans a total of $N_{RF} = 3840$ RF buckets (harmonic number). In principle, it is possible to generate as many regular bunch patterns as divisors of N_{RF}. We call N_B to the number of stored bunches, e.g., $N_B = 1920$ (80) for Brightness (Timing) mode. To target a specific bunch filling sequence, the injection period can be set to

$$T_{inj} = (N_r N_B + k) T_{BS}. \quad (2.3)$$

Here T_{BS} is the bunch spacing in time, e.g., $T_{BS} = 4$ (96) ns for Brightness (Timing) mode. N_r is the number of complete revolutions between injections and k is an integer that controls the injection sequence. Thus, after N_r turns around the ring, a new injector shot is injected k RF buckets behind the previous shot (two consecutive injector shots are spaced by kT_{BS} in the ring). We will refer to k as the bunch delay factor. If we enumerate the RF buckets to be filled in the ring from 0 to $N_B - 1$, the n-th element in the filling sequence is given by $n\,k \mod N_B$. To ensure that all the selected RF buckets are replenished during the filling sequence, k can be either 1 or any other odd integer smaller than N_B that does not share any divisor with N_B. This sequence does a total of k filling loops around the ring before every selected RF bucket has been hit.

Sweep, loop and fill time: The time to sweep the whole ring with one bunch in each selected bucket is given by $T_{sweep} = N_B T_{inj}$, which correspond to exactly k filling loops. The total number of sweeps, N_{sweep}, required to fill the ring from scratch is given by the integer ratio between the ring's bunch charge, Q_B, and the injector bunch charge – also called shot charge, Q_s, i.e. $N_{sweep} = \mathrm{round}(Q_B/Q_s)$.

Minimum injection rate: As previously mentioned, the minimum charge injection rates for the filling and top-up operations of the ring are essentially determined by the time required to fill the ring and the beam lifetime, respectively. For a certain injector shot charge, Q_s, the minimum injection rate is simply obtained by dividing the average charge injection rates by Q_s.

Maximum injection rate: In an off-axis injection scheme, injecting a new bunch in a certain RF bucket is only possible after the stored bunch has been damped. This sets a limit on the minimum shooting period on a particular RF bucket to at least $4\tau_d$. For a characteristic damping time of $\tau_d = 20$ ms [46, 47], the maximum shooting frequency into the same RF bucket is 12.5 Hz. Considering a finite kicker duration, T_{kicker}, this condition also applies to other bunches sitting on nearby RF buckets at a time distance smaller than T_{kicker}. If the kicker duration is greater than the bunch spacing, a value of k such that $kT_{BS} > T_{kicker}$, ensures that the injection kicker time window will not disturb a previously injected bunch before a loop time, i.e. $T_{loop} = T_{sweep}/k$. Thus, by sequencing appropriately the RF buckets to fill, the maximum

[3] Assuming 24 h average time intervals between refills.

injection rate can be increased significantly to

$$\mathcal{R}^{\max} = \mathrm{N_B}/(4\tau_\mathrm{d}\, k)\,. \qquad (2.4)$$

Because the bunch spacing in Brightness mode is rather short (4 ns), it might be necessary to use $k = 7$ or higher in the definition of the injection period (Eq. (2.3)). For $k = 7$, $\mathcal{R}^{\max} = 3428$ (143) Hz for Brightness (Timing) mode.

2.2. The RF injector system

The existing PETRA III injector complex – consisting of a 450 MeV S-band linac (LINAC II) and a fast-cycling booster synchrotron (DESY II) for acceleration to 6 GeV – cannot be used for PETRA IV, since the emittance of DESY II is by far too large, and cannot reasonably be sufficiently improved. Therefore, for the new complex, it is foreseen to use a significantly refurbished LINAC II together with a new low-emittance booster ring, DESY IV [49] (Fig. 1).

The RF injector chain will be capable of providing bunches of up to 1 nC charge at a 5 Hz repetition rate. This will allow for filling the machine in less than 7 min for all modes of operation (6 min 24 sec and 2 min 8 sec in Brightness and Timing modes, respectively). The electron bunches will have a transverse geometrical emittance of 20 nm rad and an rms relative energy spread of 0.26% [49]. Due to a limited dynamic aperture of the storage ring, special beam manipulation schemes such as bunch rotation or aperture sharing are required to achieve high injection efficiency [50]. Table 3 summarizes the operational parameters of the RF injector in Brightness and Timing modes.

Operational parameter	Brightness	Timing
Number of bunches	1920	80
Bunch charge / nC	0.8	8.0
Total charge / nC	1536	640
	Initial filling	
Shot charge / pC	800	1000
Injection frequency / Hz	5	5
Number of shots	1920	640
Filling time / s	384	128
	Top up	
Shot charge / pC	80	800
Injection frequency / Hz	5	5
Number of shots	192	8
Top-up time / s	38	2
Top-up period / s	360	180
Duty cycle	1/10	1/90

Table 3. Operational injection parameters of the RF injector in Brightness and Timing modes.

2.2.1. Power consumption

An estimation of the average power consumption of the RF injector is given based on actual measurements done at DESY during operation of PETRA III. During the year 2018, a total energy of 46.2 GWh was consumed by PETRA III, 5.8 GWh by LINAC II and 7.5 GWh by DESY II [51]. Assuming a total effective running time of roughly 6000 hours, or 250 days a year, we estimate the average power consumption of the injector complex (LINAC II + DESY II) to be about 2.22 MW[4].

The energy consumption of PETRA III could be broken down into the following components [51]: RF – 50%, magnets – 25%, water cooling – 10%, and 15% for other miscellaneous sources. One can assume that similar breakdown ratios will also apply to DESY II and LINAC II. The RF transmitter in DESY II consumes 500 kW average power [52, 53]. Assuming that the latter dominates the RF power consumption and that this in turn amount to 50% of the total consumption, we estimate an average power consumption of about 1 MW for DESY II. Considering that in 2018 the energy consumption of LINAC II was 80% that of DESY II, we reached another, slightly lower estimate for the power consumption of the injector complex at approximately 1.8 MW. Therefore, the available data suggest that the average power consumption of the RF injector complex operating for PETRA III was around 2 MW. It should be noted that both LINAC II and DESY II operate with plenty of redundancies in order to guarantee high availability in 24/7 user operation, which has a sizeable impact in the total power consumption.

For PETRA IV, the power consumption of LINAC II is expected to be significantly lower due to specific refurbishment of various components. Currently, LINAC II operates at a reduced power of 580 kW, and there are prospects to further reduce the power

[4] During a significant fraction of their total running time in 2018, LINAC II and DESY II provided test beams rather than directly injecting into PETRA III. However, the average power consumption remains consistent across different applications.

consumption substantially by refurbishing the magnets, the RF stations, and the cooling system [54]. Therefore, a more realistic estimate for the power consumption of LINAC II, operating for PETRA IV in the future, would be 0.5 MW. On the other hand, the new synchrotron booster, DESY IV, is expected to have higher peak power consumption. This is primarily due to the need to produce lower-emittance beams for PETRA IV, which requires a higher voltage in the RF cavities and increasing the number and strength of the magnets of the synchrotron booster. Based on current prospects, the peak power consumption of the future DESY IV is expected to be around 2.2 MW, from which approximately 1.0 MW would be consumed by the RF, 1.0 MW by the magnets and 0.2 MW by the water cooling. In total, adding the consumption of LINAC II, the projected peak power consumption of the future RF injector system for PETRA IV is estimated to be around 2.7 MW, approximately 35% greater than that of the current injector used for PETRA III.

A separate and substantial contribution to the total power consumption of the injector complex comes from the 6 GeV transfer line, which transports the electron beam from the synchrotron booster to the storage ring. With about 200 m in length, the expected power demands of the transfer line amounts to 320 kW: 290 kW for the magnets, 20 kW for the vacuum and 10 kW on miscellaneous sources [55].

Top-up operation: It is important to note that the power consumption figures provided here pertain to full-power operation of the injector, particularly during demanding tasks such as filling the storage ring from scratch. We have referred to this as peak power consumption. In the top-up operation mode, a notable reduction in average power consumption is expected, as only a small fraction of the stored charge needs to be replenished. Consequently, during top-up operation, the peak power is only necessary for a reduced duty cycle. The remainder of the time, the injector system can be in standby mode, prepared to provide beams for top-up as needed. It is yet to be studied which elements of the injector system can be switched off between top-ups. In principle, potential savings of up to 25% could be achieved by turning off the magnets of the synchrotron booster. In case of LINAC II, the low energy accumulator ring PIA could be bypassed during top-up operation entirely, as it is mainly used for high-bunch-charge operation during the ring's fillings. Switching off PIA's magnets would save around 100 kW. It is not clear yet how much RF power could be saved in standby mode.

3. The Plasma Injector

3.1. Introduction

Since the early 2000s, LPAs have shown significant experimental progress on several important fronts, including the demonstration of ever-increasing energies in the GeV range [6–8], narrow energy spectra [9–11], and low emittances [12–15]. Today, the LPA beam quality has been proven sufficient to demonstrate free-electron lasing [22] and progress towards their practical usability is accelerating rapidly with DESY taking a leading role: around 2020, few-percent levels of electron beam energy stability were demonstrated during a 24-hour-long operation run [16] as well as machine-learning-supported auto-alignment and beam control [17, 18, 56, 57]. This exciting progress encourages considering LPAs as a practical alternative to RF particle accelerators for free-electron lasers [19–23] and as injectors for storage rings [4, 24, 25]. In particular, we propose to equip PETRA IV with a modern plasma injector system to fill and top up the storage ring, significantly reducing the spatial footprint and energetic cost of the whole injector complex (see Fig. 1).

As of today, the laser-plasma technology is not quite ready yet for this ultimate step since the operational stability is not yet sufficient, and the drive laser technology needs to be matured to achieve the desired levels of reliability. For this reason, we discuss a step-wise implementation roadmap in Sec. 4. Optimal PETRA IV operation demands filling the entire PETRA IV ring from scratch in an acceptable time[1], providing an average charge rate of up to 2.6 nC/s inside the ring's acceptance with a mean time between failures that is commensurate with its exceptional availability standards. However, it is expected that this level of maturity can be reached during the machine's lifetime. Thus, PETRA IV is conceived and prepared not only to take advantage of application-ready, high-average-current LPAs, but also to actively accelerate their development by providing a plasma-based injector beamline to finesse the technology. In this way, PETRA IV demonstrates technological leadership in the field and, at the same time, acts as the catalyst for plasma technology and its application in user facilities with an impact that will be felt far beyond the confines of DESY.

The key challenges for the plasma injector are outlined in the following sections before the design of an operation-ready plasma injector is presented. The demands on a PETRA IV injector to produce a high charge rate within a narrow energy acceptance window are substantial. It is key for the LPA to efficiently convert energy from the laser to the electron beam and, simultaneously, provide a sufficient beam quality to ensure a high injection throughput. To achieve this task, not only has the quality (emittance and the energy spread) of single electron bunches from the LPA to be excellent, but also the accelerator must perform stably, with high availability and long mean time between failures, and at a relatively high repetition rate. Finally, the LPA must accelerate the beams up to the full 6 GeV as required for direct injection into the PETRA IV ring.

Energy gain: Beams up to 8 GeV in energy have been demonstrated in LPA experiments at LBNL by guiding the Ti:Sa BELLA Petawatt laser using a capillary discharge waveguide in conjunction with a laser heater [8]. The deployment of laser guiding technology is essential in LPAs to achieve reliable multi-GeV energy gains. Capillary discharge waveguides for guiding high-power lasers with sufficiently small spot sizes to enable energy-efficient acceleration are technically challenging. Besides, operating these capillary-based systems at high repetition rate without performance degradation is yet another open challenge[2]. An alternative approach for guiding high-power lasers with

[1] Operating PETRA IV at the desired performance prescribes filling times no larger than 10 minutes.

[2] Generating waveguides of sufficient strength requires using small diameter capillaries, which may experience wall-erosion/damage during operation preventing their long-term utilization.

smaller spot sizes has been recently developed [26, 27, 58, 59], and demonstrated the production of multi-GeV electron beams using lasers of reduced energy [60, 61]. These hydrodynamic optical-field-ionized (HOFI) plasma channels utilize an auxiliary low-energy laser to ionize and heat a long (and thin) column of plasma. This column undergoes a radial hydrodynamic expansion over several nanoseconds forming a plasma structure suitable for laser guiding just prior to the arrival of the main drive pulse. This technique is ideally suited to LPAs with operating lengths of hundreds of millimeters in plasma, at high repetition rates and for extended periods of time since wall erosion cannot occur (a *fresh* waveguide is formed in free space on each shot). The PETRA IV plasma injector will build on and advance this concept.

Quality, control and stability: Recent LPA experiments conducted at LUX (DESY) have shown enormous progress towards enhanced beam quality and application readiness, demonstrating few-percent-level energy spread [17] and operational stability over 29 hours [16]. Additionally, these experiments identified correlations between energy variations in the LPA bunches and laser jitter-induced bunch charge fluctuations. Exploiting these correlations by means of advanced machine learning techniques such as Bayesian optimization [18, 56, 57] allows for enhanced control over the parameters governing the LPA, and thus, for further improving the bunch energy stability down to 1%. Looking ahead, as LPA systems evolve to operate at higher repetition rates ($\gtrsim$ 100 Hz) with automated optimization and AI-based stabilization, we can anticipate achieving a sub-percent level of energy spread and jitter in the long term. The KALDERA project at DESY will be the epicenter of these technological advances with its goal of developing a 1 kHz, 100 TW laser system for plasma wakefield acceleration with ultimate quality and stability. Yet, for the PIP4 conceptual design, we have adopted an energy compression and stabilization strategy recently proposed for LPAs [25, 29], which promises to deliver unprecedented levels of relative energy spread and stability ($\sim 10^{-4}$) from current state-of-the-art LPAs, thus making it possible to operate the injector with the required quality and stability for PETRA IV.

Performance: Filling the ring from scratch at an average injection charge rate of 2.6 nC/s is the most demanding task for the PETRA IV injector. Besides, the performance of the plasma injector needs to be on par with the exceptional standard foreseen for PETRA IV, ensuring high availability (> 98%) and long mean time between failures (> 50 hours). The development of a laser system capable to operate the plasma injector in this regime is a crucial challenge to achieve a competitive technology-replacing plasma injector for PETRA IV. Designed to deliver up to 3 kW (3 J pulses at 1 kHz) of average optical power, KALDERA will be the foundation on which the laser system of the PETRA IV plasma injector is built.

Conceptual design: Our design for the plasma injector of PETRA IV comprises two key components – Fig. 3 (a): a laser-plasma accelerator (LPA) and an energy compression beamline (ECB) [25, 29]. Utilizing an upgraded version of the KALDERA laser, the LPA produces electron beams at 6 GeV energy with state-of-the-art beam quality and stability, while the ECB further reduces the beam energy fluctuations and spread to the sub-permille level, maximizing the net charge injection throughput into the PETRA IV storage ring. Initially, this plasma injector could be employed for top-up operation of the storage ring, significantly reducing the load on the RF injector system. In the future, with the continued advancement of high-efficiency, high-power laser drivers, the plasma injector could potentially replace the RF injector system altogether, enabling a substantial reduction of both the spatial footprint and energetic consumption of the entire injector complex.

In what follows, we describe in detail the different parts of the design and provide results from numerical start-to-end simulations performed for a particular optimized setup (Secs. 3.2 and 3.3). In light of these results, we then report on the expected performance of the plasma injector (Sec. 3.5) and discuss the prospects of the power consumption (Sec. 3.6).

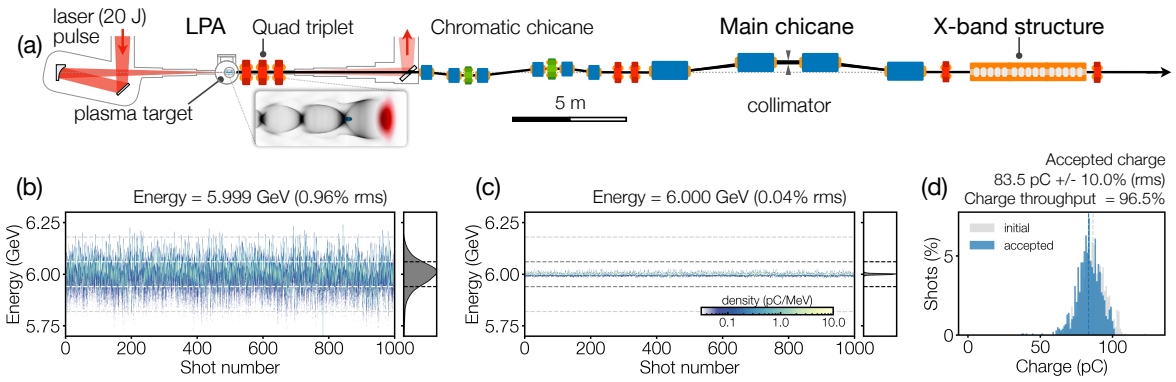

Figure 3. Schematic layout of the plasma injector for PETRA IV (a): the LPA produces electron beams at 6 GeV with 1% (projected) energy spread. A quadrupole triplet (red) captures the beam and matches it to a dispersive section (chromatic chicane), made up of dipoles (blue) and sextupoles (green), that corrects the chromatic emittance growth. The beamline continues with the main chicane that induces a large longitudinal decompression and a linear energy-time correlation over the beam. The energy correlation is then canceled out by a 5-meter-long X-band RF structure (orange). The integrated spectrum of the beam is compressed by a factor 24, enabling an efficient injection into the storage ring. Electron beams spectra before (b) and after (c) energy compression. Distribution of the initial and accepted beam charge (d).

3.2. Laser-Plasma Accelerator

Laser-plasma accelerators are driven by highly-intense laser pulses, which excite wakefields in a plasma by means of the ponderomotive force [5, 62, 63]. The *unperturbed* plasma density, n_p, sets the spatio-temporal scale of the wakefield structure, defined by the plasma wavelength $\lambda_p = 2\pi/k_p$, with $k_p = (n_p e^2/m\epsilon_0 c^2)^{1/2}$ the plasma wavenumber, m the rest mass of the electron, e the elementary charge, c the speed of light in vacuum and ϵ_0 the vacuum permittivity (see Appx. B.2). For efficient wakefield excitation, the plasma shall be driven in the blowout regime [64, 65] by laser pulses with a high peak normalized vector potential amplitude, $a_0 \gtrsim 2$, and *resonant* in duration, $\tau \sim 1/k_p c$ (see Appx. B.3). The intensity of the laser pulse is related to a by $I = (mc^2 k_0/e)^2\ (c\epsilon_0/2)\ a^2$, with k_0 the laser wavenumber. For typical laser wavelengths around 1 µm, reaching the high peak intensities to drive a plasma blowout ($I_0 \gtrsim 5 \times 10^{18}$ W/cm^2) requires tight focusing of the laser pulse to a spot size, w_0, comparable but smaller than the plasma wavelength. The plasma density also sets the scale of the accelerating gradient present in the wakefield which, in the blowout regime, is given approximately by $E_z \sim a_0^{1/2}\,(mc^2/e)\,k_p \propto a_0^{1/2}\,n_p^{1/2}$ [66]. The acceleration of a *witness beam* of electrons at this rate is ultimately limited by the depletion length of the drive laser [63], which scales as $L_{\mathrm{depl}} \propto n_p^{-3/2}$ (see Appx. B.5). Thus, the energy gain of a single-stage LPA [63] in the depletion-limited regime scales inversely with the plasma density, i.e. $\Delta\mathcal{E}_{\mathrm{depl}} \sim eE_z L_{\mathrm{depl}} \propto n_p^{-1}$. Operating at lower plasma densities to achieve high beam energies requires, in turn, increasing the laser pulse size by a factor $\propto n_p^{-1/2}$ in every dimension while keeping its peak intensity, which results in an increase of the laser peak power as n_p^{-1} and the energy as $n_p^{-3/2}$.

Drive Laser

The Ti:Sapphire (Ti:Sa) laser technology is the most commonly used in LPA research as it allows for ultra-short laser pulses (down to 30 fs) and high peak power. With a central wavelength of 800 nm, achieving the appropriate laser parameters for a 6 GeV energy gain with a Ti:Sa system requires operating plasma densities in the 2×10^{17} cm^{-3} range, with lasers of up to few tens of Joules per pulse and peak powers near the Petawatt level [67] (see Appx. B.5). Successfully proven in multiple LPA experiments (see Table 11), Ti:Sa laser technology provides good laser pulse quality with a high degree of spatial coherence and is therefore still today the technology of choice. Over the past two decades, laser-plasma accelerators have shown rapid development and impressive performance demonstrating electron beam parameters of quality similar to modern RF-based accelerators. However, the reproducibility and reliability of the generated electron beams has been until recently considered insufficient to drive user

applications. As shown in experiments at LUX (DESY) [16, 17] the bulk of the variations in electron beam properties can be traced to shot-to-shot variations in the drive laser pulse, which in turn can be connected to short-term variations in the power grid, air turbulences, or vibrations. A clear path towards enhanced control, reliability and performance is the deployment of active stabilization and feedback systems running at a sufficiently high repetition rate. As we will see in Sec. 3.4, running the LPA at a relatively high repetition rate (~32 Hz) will be also necessary to fulfill the PETRA IV demands to fill the storage ring in a sensible time. Lower laser repetition rates are possible, but would require higher laser pulse energies. A timely implementation of a plasma-injector could be based on KALDERA as a frontend in combination with an additional future Petawatt amplifier, which would benefit from the very high repetition rates of KALDERA to implement active stabilization and feedback throughout the whole amplification chain, thus providing a significantly more stable system. Building the plasma injector as the sole driver of the PETRA IV synchrotron would require development of a new, dedicated drive laser which would also include redundancies.

Operating high-energy laser pulses at high repetition rate with Ti:Sa technology presents a challenge due to the higher stress on the thermal properties of the compression gratings and heat dissipation problems in different components of the laser system. Besides, the commonly used flashlamp-based pump lasers used in high-power amplifiers at the Petawatt-level feature low wall-plug energy efficiency of the order of 0.1%, which is detrimental for the energetic demands of PIP4 (in Sec. 3.6). Diode-pumped laser technology, on the other hand, uses laser diodes to directly pump the gain medium (usually a solid-state crystal or glass) of the laser, which eliminates the need for a separate pump laser and allows for a much higher efficiency ($\gtrsim$ 1%) and repetition rate [68]. Therefore, diode-based pump lasers are considered for a future PW-class PIP4 drive laser (see Sec. 4.2), in order to deliver full charge injection rate to fill the PETRA IV ring at a largely reduced average power consumption.

Plasma source

Provision of a high-quality 6 GeV beam compatible with injection into the PETRA IV ring requires a state-of-the-art LPA. Specifically there are two key technologies – controlled injection and laser guiding – that will be combined to achieve the required beam parameters. Both of these techniques rely on careful tailoring of the 3D plasma density structure within the LPA. Controlled injection requires longitudinal structuring to accurately localize the trapping of a low-emittance electron beam at the start of the accelerator, while plasma waveguides utilize transverse plasma density tailoring to guide a high-intensity laser over long distances commensurate with efficient multi-GeV acceleration.

A crucial aspect for the design of the LPA is to provide beams with sufficiently low energy spread and high stability together with precise control and operational reliability. In this regard, the LPA setup deployed in LUX at DESY has demonstrated its state-of-the-art capabilities for energy spread optimization [18] and stable operation around the clock [16], and it is therefore selected as the basis of the PIP4 plasma target design: the plasma source at the heart of the PETRA IV plasma injector will incorporate controlled injection in the form of density down-ramp assisted ionization injection [17], a robust technique pioneered in LUX, together with HOFI laser guiding [26]. A key concern for LPA reliability and robustness is the lifetime of the plasma source. This is particularly important as the average-power of the laser increases. In this context HOFI waveguides are advantageous as their structure is immune to damage, with a new waveguide being formed on every shot of the laser. Critically, compared to other guiding technologies, HOFI waveguides offer the ability to generate plasma channels with relatively small matched spot sizes at low plasma densities, consistent with the required multi-GeV acceleration [27, 61, 69]. This is a critical requirement for improving the efficiency of the accelerator.

Simulation and optimization

The injection and subsequent acceleration of electrons in the LPA was extensively modeled with the particle-in-cell (PIC) code

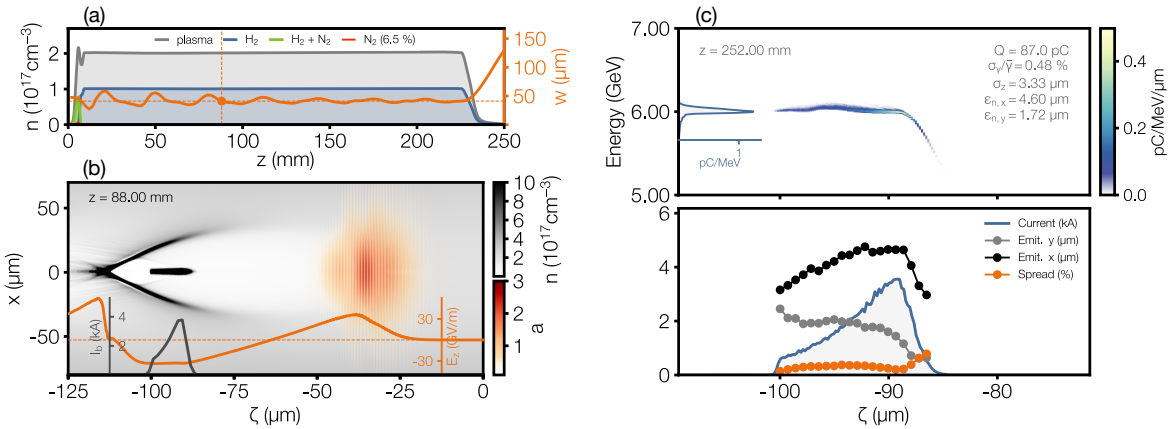

Figure 4. Longitudinal profile of the different gaseous components forming the plasma target used in particle-in-cell simulations (a). FBPIC simulation snapshot showing the drive laser, the wake of plasma electrons and the injected bunch after 88 mm of propagation (b). Longitudinal phase space and sliced properties of the electron bunch at the exit of the plasma target (c).

FBPIC [70], utilizing machine-learning-based tools such as Bayesian optimization to find optimal working points to evaluate performance [18, 71, 72]. In the optimization process, the key parameters of the laser and plasma source of the LPA were varied within realistic boundaries to find a design which maximizes the beam spectral density around 6 GeV and minimizes the laser energy, thus maximizing the quality and the efficiency of the injection in the storage ring. More details about this optimization process are given in Appx. A.1. We refer to this optimized setup as working point one (WP1), which we will use throughout this section as the reference case to assess the performance and feasibility of the design of the plasma injector. Other working points with different starting configurations for the laser and the plasma guiding channel have been explored as well. In Appx. A.2, we report on a set of configurations considering narrower guiding channels and less energetic laser pulses. We refer to this set as working point two (WP2). The limits of the LPA design in terms of laser energy and energy efficiency are explored in Appx. A.3.

Plasma profile: The resulting plasma profile for WP1 is depicted in Fig. 4(a). With a nominal plateau density of $n_p = 2.0 \times 10^{17}$ cm^{-3}, the profile counts on a doped density spike at the beginning, to trigger density downramp assisted ionization injection [17], followed by a 22-cm-long plateau to accelerate the injected electron bunch to 6 GeV energy. The doped plasma spike is formed from a mixture composed of hydrogen doped with nitrogen at 6.5%. The long plateau consists of pure hydrogen. By independently adjusting the pressures of the two gaseous sources, the height and shape of the spike can be tuned. Injection is triggered by the high-intensity core of the laser that ionizes the two inner electronic levels (K shell) of nitrogen. With much lower ionization thresholds, the other electrons present in the gas mixture were previously ionized by the laser forefront to form the background plasma. The plasma density downramp of the spike facilitates the trapping of the nitrogen K-shell electrons and allows for a certain tunability of the current profile of the witness beam. The plasma profile ends with a tailored plasma-to-vacuum transition which reduces the divergence of the electron beam and contributes to mitigate the chromatic emittance growth during the free drift in vacuum [73–75] (see Appx. B.7).

Transversely, the profile follows a perfectly parabolic distribution suitable for matched guiding of a low-intensity Gaussian laser with spot size $w_m = 50$ µm (see Appx. B.6). The choice of this value for the matched spot size is in good agreement with measurements performed for HOFI channels [27] at plasma densities around 2×10^{17} cm^{-3} (see Appx. B.6.2).

Laser pulse: In the simulations, the laser pulse was modeled with a flattened Gaussian beam [76] (order 100) with $\lambda_0 = 0.8$ µm wavelength and linearly polarized in the horizontal direction. This analytical laser beam approximates accurately the radial intensity evolution produced by actual com-

mercial Ti:Sa laser systems commonly used for laser-plasma acceleration [17]. For the optimization, we kept approximately constant the laser focal spot size, $w_0 = 50\ \mu$m, and the laser peak power, $P_0 = 345$ TW, which correspond to a peak normalized vector potential of $a_0 = 2.0$; and varied the laser focal position and the pulse duration (see Appx. A.1). At the optimal point, the laser is focused at $z = 6.0$ mm and has a duration of 53 fs (fwhm). The initial pulse energy is therefore 19.6 J. In practice, a laser focal spot of 50 μm can be achieved using a 8.8 m focal length off-axis parabolic (OAP) mirror at $f/55$.

Figure 4(a) also shows the evolution of the laser spot size (fwhm in intensity) along the propagation through the plasma. Despite the initial oscillations, the laser is effectively guided through the plasma target: the spot size undergoes damped oscillations with a period of $\sim$ 3 cm (see Appx. B.6). Consequently, an oscillating laser intensity results in a oscillating wakefield strength along the witness beam. On top of this, the depletion and dephasing effects (see Appx. B.4) contribute to a varying wakefield scenario through the acceleration process. Figure 4(b) shows the drive laser intensity profile, the plasma wake and the injected bunch around the middle point of the acceleration. At this particular point of the acceleration, the space-charge field of the electron beam acts on the plasma electrons, flattening the variation of the accelerating gradient (see Appx. B.3). However, due to the evolution of the wakefield, this effect, known as beam loading, varies over the entire propagation.

Electron beam: The optimization process for WP1 found configurations where the witness beam has a negligible energy-position correlation (chirp) after acceleration – Fig. 4(c). This is the result of an *average beam loading* effect. At the beginning of the propagation, when the laser is fresh and its spot-size oscillations are stronger, the laser-driven plasma wakefield is weaker on average. At this point, the injected beam overloads the wakefield and develops a positive chirp. As the laser spot size stabilizes and the laser pulse compresses longitudinally, the increase in laser intensity intensifies the wakefields [77]. From this point on, the witness beam underloads the wakefield, which progressively compensates for the previously accumulated positive chirp while further accelerating the beam towards the target energy of 6 GeV. The evolution of key beam parameters such as its average energy, energy spread and chirp, throughout the acceleration process are shown in Fig. 15. This optimal working point enables the generation of a 6 GeV electron bunch with 87 pC charge and 0.5% energy spread (Fig. 4(c)). The energy spread is defined here as $\sigma_\gamma \equiv 1.48$ MAD, with MAD being the median absolute deviation of the beam's spectrum[3]. The normalized emittance in the horizontal plane (4.6 μm) is significantly higher than in the vertical plane (1.7 μm) due to the linear polarization of the laser, which induces a higher electron temperature in the horizontal direction. The beam divergence is 0.22 and 0.12 mrad in the horizontal and vertical planes, respectively. The total laser-to-beam energy transfer efficiency is 2.7%. More details on the optimization process are given in Appx. A.1.1.

Other working points explored in Appx. A.2 demonstrate the production of beams of comparable quality (energy spread and emittance) with charges in the 50–100 pC range, employing laser pulses energies between 13 and 17 J. Table 8 summarizes the parameters of a set of selected working points. While these working points show the possibility to operate the PIP4 with lower laser pulse energy, WP1 was chosen as a conservative reference in the following sections.

Beam jitter: In experimental conditions, the optimal working point will be affected by fluctuations in both the laser and the plasma profile. As shown in Ref. [17], the laser focal position correlates with the amount of injected charge, and thus, the operation at optimal beam loading conditions, consequently leading to changes in the beam energy spread and final energy (see Appx. A.1.2). Variations in the plasma guiding channel will additionally affect the net beam loading. This combination of different sources of jitter results in a wider

[3] Note that with this definition the energy spread coincides with the rms value in case of a Gaussian distribution.

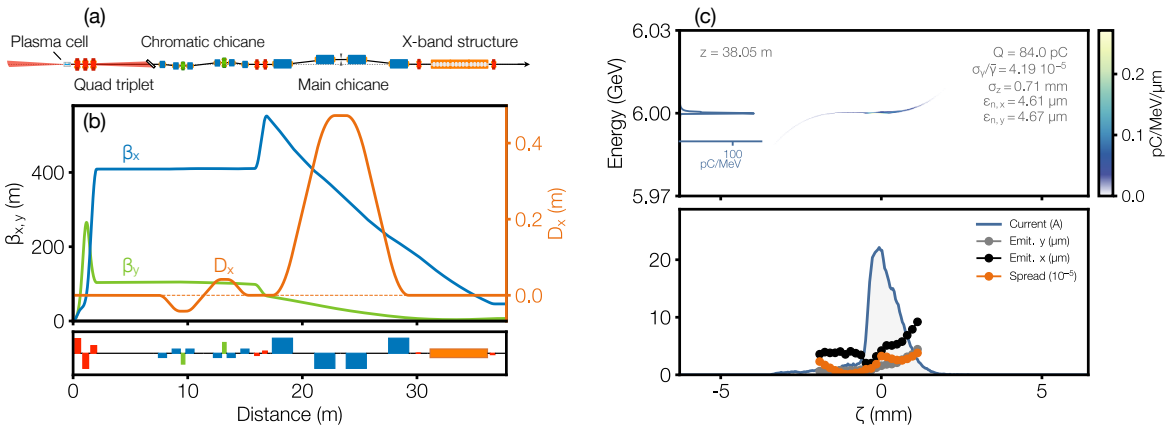

Figure 5. Schematic of the ECB (a) – Dipoles are shown in blue, quadrupoles in red, sextupoles in green, and the X-band RF in orange. Twiss optics functions from the plasma cell through the ECB. The relative strengths of the different beamline elements are shown in bottom panel (b). Phase space and sliced quantities of the beam after the ECB (c).

beam spectrum when integrated over many laser shots, which ultimately translates into a significant fraction of the beam missing the momentum acceptance of the ring and, as a consequence, into a low laser-to-stored-beam energy conversion efficiency and higher bunch charge variations. In Fig. 3 (b) we show a collection of spectra from 1000 LPA acceleration events including jitter in the most relevant parameters. Triggered by realistic fluctuations in the laser focal position (0.75 mm rms), the laser energy (0.75% rms) and the plasma density (0.75% rms), with respect to the optimal case for WP1, the total projected spectrum of the beam yields a central energy of 5.999 GeV (0.96 % rms) with an average bunch charge of 86.5 pC varying by 9.8 % rms. More details about this approach can be found in Appx. A.1.2.

Direct injection of this beam into the storage ring without additional manipulation would lead to significant degradation and beam losses owing to the mismatch of its phase space to the acceptance of the storage ring. Therefore, an additional component is introduced to enable beam capture after the LPA with minimum chromatic emittance degradation, energy spread and stability compression to a sub-permille level, and finally, a matching of the Twiss optics functions to those at the injection point of PETRA IV. These three functions are performed by the energy compression beamline, which we describe in the following section.

3.3. Energy Compression Beamline

In order to reduce the overall energy fluctuations of the LPA beam and increase the net charge injection throughput into PETRA IV, we adopt an energy compression and stabilization strategy proposed recently [29]. The method requires a magnetic chicane to stretch the bunch and create a linear correlation between particles' energies and their longitudinal positions (chirp), and an active dechirper that applies a linearly varying kick to adjust all particles to the design energy. The effect of a dispersive section (e.g. a chicane) on the phase space of the beam is described to first order by the R_{56} element, which relates shifts in the longitudinal position of the beam's particles with relative shifts in energy with respect to a certain reference energy, E_{ref}. Considering a beam with initial length, σ_{ζ_i}, relative energy spread, σ_{δ_i}, and no correlation in its longitudinal phase space, through the dispersive section the beam is stretched to a length $\sigma_\zeta = R_{56}\sigma_{\delta_i}$, while developing a chirp given by $\chi = E_{\mathrm{ref}}/R_{56}$ (up to linear order). Thus, by applying a linear voltage with slope $V' \equiv \partial_\zeta V = -\chi/e$ the induced chirp can be virtually removed. After dechirping, the final *uncorrelated* energy spread of the beam is

$$\sigma_\delta^u = \frac{\sigma_{\zeta_i}}{R_{56}}\,. \tag{3.1}$$

We shall note that these expressions hold when the stretching factor $S \equiv \sigma_\zeta/\sigma_{\zeta_i} \simeq R_{56}\sigma_{\delta_i}/\sigma_{\zeta_i} \gg 1$. The final mean relative energy deviation is given by $\bar{\delta} = (\zeta_0 - \zeta_{\mathrm{ref}})/R_{56}$, with ζ_0 the zero crossing of the applied volt-

age and $\zeta_{\rm ref}$ the position of a virtual reference particle with energy $E_{\rm ref}$. Therefore, by adjusting $\zeta_0 = \zeta_{\rm ref}$, the final beam energy can be stabilized to the desired reference value, regardless an incoming energy jitter. Thus, the active dechirper compensates for both the beam energy spread and the jitter of the central energy. Provided the natural micron-short lengths of the LPA beams (Fig. 4(c)), it is clear from Eq. (3.1) that an R_{56} of a few centimeters would be enough to bring the final relative energy deviations of the beams down to a 10^{-4} level. Moreover, since the high peak currents naturally produced by LPAs are not desirable for injection into synchrotron light sources anyway, it is also convenient to induce a large longitudinal decompression and apply a matching dechirper based on RF technology [25]. Considering the sinusoidal voltage of an RF accelerating structure, $V_{\rm RF} = V^0_{\rm RF}\ \sin[k_{\rm RF}(\zeta - \zeta_0)]$, with $V_{\rm RF,0}$ the voltage amplitude and $k_{\rm RF} = 2\pi\, f_{\rm RF}/c$ the wavenumber of the RF signal, dechirping the beam after decompression using the linear part of the RF voltage around the zero crossing requires an amplitude of

$$V^0_{\rm RF} = \frac{E_{\rm ref}/e}{k_{\rm RF} R_{56}}\,. \tag{3.2}$$

In practice, the non-linearity of the RF voltage imprints a residual energy-phase modulation in the beam that results in a larger *correlated* energy spread, which can be calculated to leading order for a Gaussian beam [25] with initial mean energy, $E_{\rm ref}$, to be

$$\sigma^c_\delta \simeq 0.645\,(k_{\rm RF} R_{56})^2\,\sigma^3_{\delta_i}\,. \tag{3.3}$$

Therefore, the final projected energy spread of the beam is obtained as the quadratic sum of the uncorrelated (Eq. (3.1)) and correlated (Eq. (3.3)) components. The correlated contribution to the total energy spread is the dominant factor for beams with larger initial energy spreads, i.e., $k_{\rm RF} R_{56} \sigma_{\delta_i} \gtrsim 1$.

The final mean energy jitter is also affected by the correlated contribution arising from the non-linearity of the dechirper. A time-arrival jitter, $\sigma^{\rm tj}_t$, between the RF signal and the electron beam can further accentuate this effect when $k_{\rm RF} c \sigma^{\rm tj}_t \gtrsim 1$. In addition, the timing jitter would also result in a non-perfect compensation of the central energy deviations of the beam, i.e., $\sigma^{\rm tj}_\delta = c\sigma^{\rm tj}_t / R_{56}$. The performance of this scheme applied to a low-energy plasma injector prototype was recently demonstrated by means of start-to-end simulations [25].

The schematic of the proposed energy compressor beamline is shown in Fig. 5(a). Figure 5(b) shows the relative strengths of the different elements of the beamline (dipoles, quadrupoles, sextupoles and RF structure) and the design optic functions for a reference beam with the same statistical parameters as the one shown in Fig. 4. First, the LPA beam is captured by a triplet of strong quadrupole magnets situated as close as possible to the plasma cell to mitigate the chromatic emittance increase of the LPA beam. The capture triplet is followed by a drift space for laser beam removal and diagnostics. Next, an S-chicane with two sextupoles corrects the chromatic emittance increase in the horizontal plane, where the emittance of the beam is higher by construction. The large β-function in the horizontal plane allows for an efficient chromatic correction by a relatively weak chicane as the required sextupole strength, S, decreases with the product of the dispersion, D_x, and the β-function of the beam, $\hat{\beta}_x$, i.e. $S \propto 1/\hat{\beta}_x D_x$. At the same time, the small β-function in the vertical plane minimizes the detrimental nonlinear aberration of the vertical emittance (Fig. 5 (b)). With an $R_{56} = 5$ mm, this chicane also serves as a pre-stretcher, increasing the rms bunch length from ~ 3 to ~ 30 μm in order to mitigate coherent synchrotron radiation (CSR) effects in the main chicane (see Appx. A.4).

Element	Length	Strength
Capture quads.	50 cm	G ≤ 82 T/m
Optic quads.	40 cm	G ≤ 12 T/m
S-chicane dips.	70 cm	B = 1.00 T
Main chicane dips.	175 cm	B = 1.45 T
Chromatic sexts.	30 cm	S = 550 T/m^2
X-band structure	500 cm	V = 227 MV

Table 4. Parameters of key beamline elements.

The main chicane is composed of four strong dipoles with a collimator in the middle. The large horizontal dispersion allows for an efficient momentum collimation at ±3%, i.e. $\delta_{\rm col} = 0.03$. The R_{56} of the main chicane is 10 cm. The combined effect of both chicanes results in a net $R_{56} = 10.5$ cm, which induces a chirp of 57 MeV/mm on the beam. Then an X-band (12 GHz) RF dechirper corrects the energy deviation by

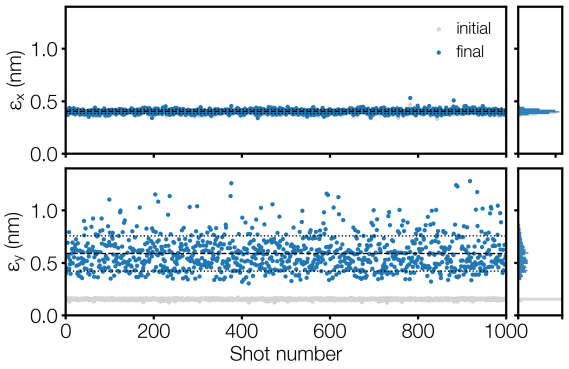

Figure 6. Geometric emittance of the simulated bunches in the horizontal (top) and vertical (botton) planes, before (grey) and after (blue) the energy compression beamline.

applying a voltage of 227 MV in amplitude (see Eq. (3.2)). Considering an accelerating gradient of 60 MV/m, such voltage amplitude would be reached by about 4 m of active length[4], for the purpose of this report we assume that the total physical length of the X-band module would not exceed 5 m. The wavelength of the RF signal, $\lambda_{RF} = 2.5$ cm, is long enough to accommodate all particles going through the collimator well inside the linear part of the RF signal, i.e. $\delta_{col}\, R_{56} \ll \lambda_{RF}/4$. Finally, the last two quadrupole magnets match the Twiss functions to those of the PETRA IV injection point. Including the laser in- and outcoupling segments (~ 18 m), the total length of the LPA and ECB is smaller than 50 m. Fig. 5 (b) shows the Twiss optic functions of the beam through the ECB. The design parameters of the main components of the beamline can be found in Tab. 4.

Beamline simulations: The simulated LPA beams are further tracked through the beamline using the particle tracking code OCELOT [79], taking into account up to second-order beam optics, RF, collimation, and CSR effects. Figure 5(c) shows the beam phase space after the ECB for the optimal bunch shown in Fig. 4(c). It showcases an extremely low relative energy spread of 4×10^{-5}. Figures 3 (b) and (c) display the beam spectra before and after the ECB, respectively, for the set of 1000 bunches with laser and plasma fluctuations included. In addition to these jitters, random pointing angle jitters of 0.2 and 0.1 mrad (rms) in the horizontal and vertical directions, respectively, were introduced in the LPA bunches right after the plasma exit. The magnitude of the pointing angle jitter is expected to be on the same order of the beam divergence [17]. Besides, a realistic timing jitter of 100 fs rms between the LPA beam and the RF signal was introduced in the beamline particle tracking simulations. This level of synchronization has been demonstrated at the Polarix TDS at FLASH [80]. As a result, the projected beam spectral bandwidth is compressed from an initial 0.96% down to 0.04% (Fig. 3 (c)), which is well below the momentum acceptance of PETRA IV. The average bunch charge after compression is 83.5 pC varying by 10.0% rms (Fig. 3 (d)). On average, only 3.5% of the initial charge is lost, mainly owing to its location outside the ± 3% energy-window of the collimator in the chicane. Thus, the total charge throughput is 96.5 %, which results in an overall laser-to-stored-beam energy transfer efficiency of 2.6%. The geometric emittance of the 1000 bunches is shown in Fig. 6. Thanks to the chromaticity correction performed by the S-chicane, the emittance is preserved in the horizontal plane. The emittance grows significantly in the vertical plane, but since it started at a lower value after the LPA, the final values are still well below the transverse acceptance of PETRA IV. Table 5 summarizes the collective electron beam properties before and after the ECB. More details about the beamline design and simulations are given in Appx. A.4.

Parameter	Plasma cell exit	After beamline
Charge	86.5 pC	83.5 pC
Charge spread	9.8%	10.0%
Energy	5.999 GeV	6.000 GeV
Energy spread	0.96%	0.04%
Emittance (x, y)	0.40, 0.16 nm	0.40, 0.58 nm

Table 5. Collective beam parameters at the plasma cell exit and after the ECB.

3.4. Injection into PETRA IV

After energy compression, the electron beam shall be delivered to the PETRA IV storage ring. This can be done using a standard transfer line consisting of a set of dipole and quadrupole magnets arranged in a sim-

[4] The required voltage can be created by one X-band RF module of CompactLight design, which consists of four 0.9-m-long X-band cavities and provides up to 234 MV of accelerating voltage when powered by a 50 MW RF system [78].

ple FODO lattice. The particular design for the transfer line will depend on the final location of the plasma injector and the exact geometry of the tunnel infrastructure connecting the plasma injector with PETRA IV. In Sec. 4.4, we provide more details about a concrete solution for the PIP4 location and its transfer line. After the beam transport, the Twiss functions of the beam have to be matched to those of the PETRA IV injection point, which can be done readily by tuning the last few quadrupoles in the transport line. In the current design, these are $\hat{\beta}_x = 46.0\,\text{m}$, $\hat{\beta}_y = 6.8\,\text{m}$, and $\hat{\alpha}_{x,y} = 0$. Since after the ECB the electron beams have been largely decompressed longitudinally and compressed in energy, no spurious effects such as CSR and chromatic emittance growth are expected along the transport. For this reason, in the start-to-end simulations, we proceed with the storage ring tracking simulation right after the ECB.

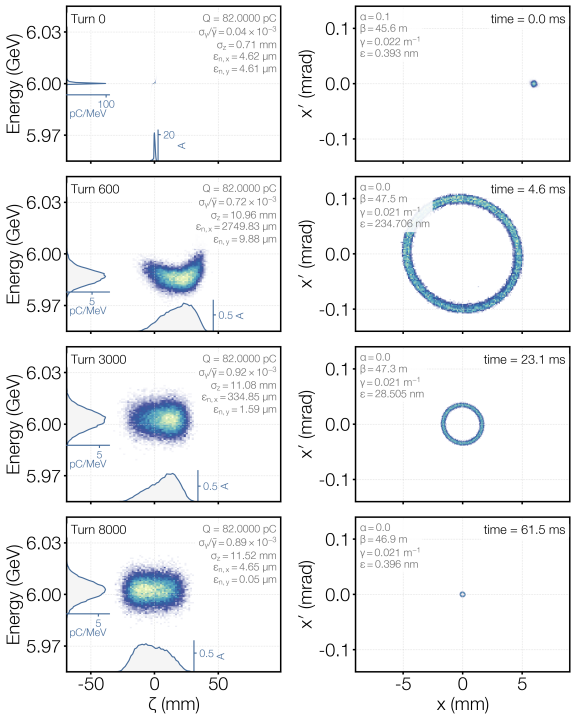

Figure 7. Phase-space evolution of the plasma injector beam in the PETRA IV ring.

PETRA IV ring simulation: The injection efficacy is verified by using element-by-element beam tracking in the storage ring with ELEGANT [81]. A comprehensive study with a realistic aperture model, wakefields, synchrotron radiation, and optics errors found no significant beam charge losses for a conservative 5% rms β-beating [82]. Thus, the simulations predict a 99.99% injection efficiency in the storage ring for the beams emerging from the plasma injector after energy compression. Figure 7 shows the phase-space evolution of the exemplary LPA beam (also shown in Fig. 5 (c) after the ECB) after injection into PETRA IV over 8000 turns, which corresponds to about 3 synchrotron radiation damping times (the radiation damping time of PETRA IV is 20 ms). Following the standard off-axis injection scheme foreseen for PETRA IV (see Sec. 2.1), the beam starts with a 6 mm injection offset in the horizontal plane. The particles are then rapidly brought to the reference orbit by synchrotron damping. In the longitudinal plane the injected beam quickly assumes an equilibrium distribution within the potential well. Compared to the RF injector chain, described in Sec. 2.2, the plasma injector could offer an order of magnitude lower transverse emittance: $\sim$ 1 vs 20 nm. This removes the need for further beam manipulation such as aperture sharing in the storage ring [50] (that could lead to injection losses, as mentioned in Sec. 2.2) or beam rotation in the transfer line.

3.5. Operational requirements

The start-to-end simulations for the plasma injector (LPA + ECB) shown throughout Secs. 3.2 and 3.3 demonstrate competitive beam parameters for injection into PETRA IV, with ~84 pC charge per bunch on average, an overall relative energy variation of 0.04% (rms) and ~0.5 nm emittance in both transverse planes, with all relevant sources of jitter considered. After the ECB, the integrated beam spectrum produced by the LPA is effectively compressed by a factor 24 (Fig. 3 (c)), elevating the charge injection throughput to 97%, accounting for realistic jitters. These simulation results showcase the expected efficacy of the ECB to compress the LPA beam energy output to maximize the injection efficiency. Besides, the ECB plays an important role preventing sizeable bunch charge fluctuations resulting from an aggressive acceptance cut for uncompressed LPA beams (see Fig. 3 (b)). There is however an intrinsic shot-to-shot LPA charge variation resulting from jitters on the laser and

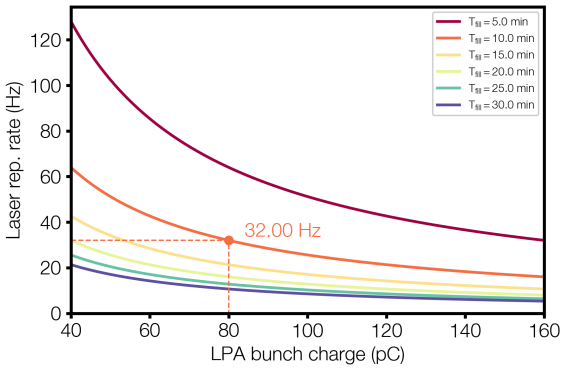

Figure 8. Laser repetition rate as a function of the LPA bunch charge for achieving different filling times in Brightness mode.

Operational parameter	Brightness	Timing
Number of bunches	1920	80
Bunch charge / nC	0.8	8.0
Total charge / nC	1536	640
	Initial filling	
Shot charge / pC	80	80
Injector frequency / Hz	32	32
Number of shots	19200	8000
Filling time / s	600	250
	Top up	
Shot charge / pC	80	80
Injector frequency / Hz	32	32
Number of shots	192	80
Top-up time / s	6	2.5
Top-up period / s	360	180
Duty cycle	1/60	1/72

Table 6. Operational injection parameters of the plasma injector in Brightness and Timing modes.

plasma parameters[5]. Fig. 3 (c) shows the distribution of the accepted bunch charge with 84 pC on average and 10% rms variation. In what follows, we discuss the details of operating PETRA IV for the initial filling and for top-up operation using the reported values of the average shot charge provided by the plasma injector.

Initial filling

As discussed in Sec. 2.1, filling the PETRA IV ring in Brightness (Timing) mode in $T_{fill} = 10$ min requires an average charge injection rate of $\mathcal{Q} = 2.6\ (1.1)$ nC/s. Considering for simplicity that the average charge per shot from the plasma injector is $Q_s = 80$ pC, the LPA drive laser would need to operate at a minimum of about 32.0 (13.3) Hz to fill the ring with 1536 (640) nC in Brightness (Timing) mode, in less than 10 minutes. Figure 8 shows different minimum injection rates for different filling times and LPA bunch charges, for the more charge-demanding Brightness mode. Filling the ring in Brightness mode thus sets the minimum repetition rate for the laser. Assuming a repetition rate of 32.0 Hz also for Timing mode, the ring would be filled in 4 minutes 10 seconds (250 s). Independently of the filling time and the injection frequency, the total number of shots during the initial filling is 19200 (8000) in Brightness (Timing) mode. Table 6 summarizes the main injection parameters for the initial filling.

The injection frequency needs to be fine-tuned to the desired injection sequence (see Sec. 2.1). For $Q_s = 80$ pC, the number of sweeps needed to fill the ring is $N_{sweep} = 10\ (100)$ in Brightness (Timing) mode. Because in Brightness mode the injection period (30 ms) is on the order of the beam damping time (20 ms) and the bunches are closely spaced in the ring (4 ns), it is necessary to select a bunch delay factor k such that $T_{kicker} < kT_{BS}$. Selecting $k = 7$ brings the condition on the kicker duration to be smaller than 28 ns. In Timing mode, the bunch spacing is sufficiently large (96 ns) to operate with $k = 1$. With k fixed, we can calculate from Eq. (2.3) the exact injection period (frequency) to complete the filling sequence in 10 minutes, which yields 31257628 ns (31.992190834 Hz) and 75002976 ns (13.332804288 Hz) for Brightness and Timing modes, respectively[6].

Top-up operation

The minimum injection rate would decrease substantially during top-up operation, as only 1% of the initial ring's charge needs be replenished as it decays (see Sec. 2.1). Considering a beam lifetime of 10 (5) hours in Brightness (Timing) mode [46, 47], the time it takes for the stored charge to decay by 1% is $T_{1\%} = 6\ (3)$ min in Brightness (Timing) mode. Thus, the average charge injection rate during top-up operation should be at least 43 (36) pC/s. Assuming that the same charge per shot is provided by the LPA, in principle, the plasma injector could be operated

[5] The shot-to-shot charge variations are ultimately limited by the stability of the laser.

[6] Because the PETRA IV storage ring operates with an RF frequency (period) of 500 MHz (2 ns), we keep decimals up to nanosecond level timing precision.

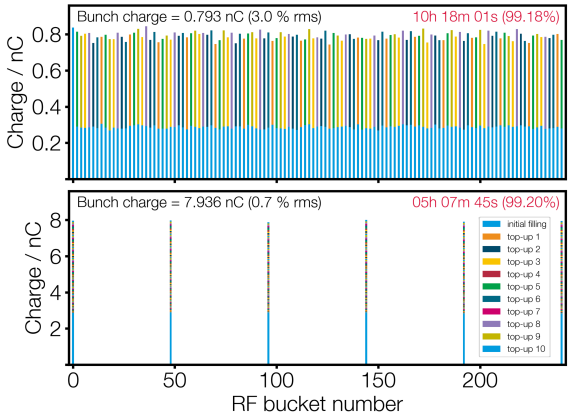

Figure 9. Simulated PETRA IV bunch charge distribution in Brightness (top) and Timing (bottom) modes after the initial filling and 100 additional top-ups, with a shot charge of 80 pC on average and 10% rms. The color code used for different top-up sequences cycles after 10 iterations.

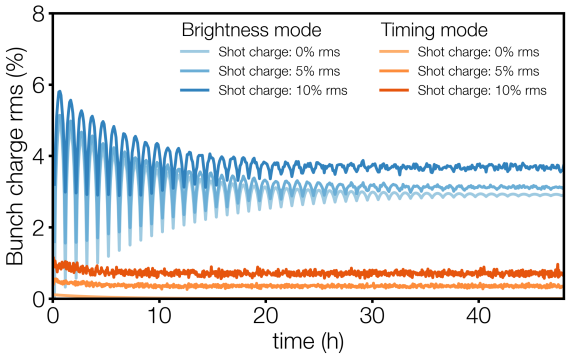

Figure 10. Simulated PETRA IV bunch charge rms variation in Brightness and Timing modes, for a shot charge of 80 pC on average and 0%, 5% and 10% rms.

at a rate as low as 0.5 (0.4) Hz in Brightness (Timing) mode. However, changing significantly the repetition rate of the laser system is not convenient in practice as it would dramatically affect its thermal properties and, in turn, the stability of the LPA. The repetition rate of the LPA during top-up, $\mathcal{R}_{top}$, shall not be much different to that used during the filling, $\mathcal{R}_{fill}$.

At least two strategies can be followed for top-up:

Continuous top-up: The shots are distributed over $T_{1\%}$ = 6 (3) minutes in Brightness (Timing) mode. This means that only one every $(100\,T_{1\%}/T_{fill}) \times (\mathcal{R}_{top}/\mathcal{R}_{fill})$ LPA shots goes to the ring. A downside of continuous top-up is that it leads to continuous perturbation of the stored beam.

Timed top-up: A different approach would consist in top-up every $T_{1\%}$. This would result in stronger, but shorter in time, perturbations to the users. In this case, all the LPA shots are injected during a reduced time, $(T_{fill}/100) \times (\mathcal{R}_{fill}/\mathcal{R}_{top})$, to complete the top-up sequence.

In both cases, the duty cycle, defined as the fraction of the time that the injector is shooting in the ring, is $1/[(100\,T_{1\%}/T_{fill}) \times (\mathcal{R}_{top}/\mathcal{R}_{fill})]$. With $\mathcal{R}_{top} = \mathcal{R}_{fill} = 32$ Hz, $T_{fill} = 600\,(250)$ s, and the duty cycle is 1/60 (1/72) in Brightness (Timing) mode. Table 6 shows the injection parameters in timed top-up operation at 32 Hz for Brightness and Timing modes.

Charge variations

After the initial filling, every bunch in PETRA IV comprises $n_s = Q_B/Q_s$ injector shots. Since the injector bunch charge fluctuations are random, the PETRA IV relative bunch charge variation will be a factor $\sqrt{n_s}$ lower than that of the injector shots. For an injector shot charge variation of 10% and using $n_s = 10\,(100)$ in Brightness (Timing) mode, the PETRA IV charge variation after the initial filling will be 3.2% (1.0%). This number slightly diminishes as more shots are injected during top-up operation.

During top-up operation, not every PETRA IV bunch needs to be replenished after $T_{1\%}$ to keep the total charge above 99%. For example, with Q_s = 80 pC, a top-up sequence would inject into 10 (100) % of the bunches available in Brightness (Timing) mode. This implies that there can be relative differences in charge from bunch to bunch up to a Q_s/Q_b factor. These differences are more pronounced in Brightness mode, where the relative rms (peak-to-peak) differences can reach a 5% (10%) of the total bunch charge, even when assuming a negligible injector shot charge variation. To quantify this effect we have calculated the evolution of the stored bunch charge (Fig. 9) and its variations (Fig. 10) during operation.

Bunch-to-bunch charge variations up to nearly 6% (rms) are computed for PETRA IV in Brightness mode when using an average injector shot charge of 80 pC with 10% rms fluctuation (Fig. 10). This is just slightly above the 5% (rms) obtained for a non-fluctuating injector shot charge. The oscillation in bunch charge variation in Brightness mode observed in Fig. 10 is the result of toping up different PETRA IV bunches at

different times. It reaches its maximum (minimum) when half (all) the PETRA IV bunches have been refilled. With a characteristic time given by the beam lifetime, the oscillation in bunch charge variations damps towards the equilibrium value, which for a non-fluctuating shot charge, yields $(Q_s/Q_B)/2\sqrt{3} = 2.9\%$, in Brightness mode. The contribution from a fluctuating shot charge to the total bunch charge variations can be added in quadrature. For 10% rms shot charge fluctuation, the bunch charge rms spread converges to 3.5% (Fig. 10).

In conclusion, although the plasma injector generally operates with less charge per shot than the RF injector, the required filling times can be achieved with a higher repetition rate. In top-up operation, also the RF injector operates with less charge per shot, and the performance of the plasma injector does not differ significantly. Despite an intrinsic shot charge variation in the plasma injector, the bunch-to-bunch charge variations of the storage ring are dominated by differences in the top-up time of different bunches.

3.6. Power consumption

The total energy consumption of the PETRA IV plasma injector can be broken down in its two essential components: the laser with the plasma accelerator module and the transport beamline with the energy compressor.

3.6.1. LPA power consumption

The LPA produces the required beam current at 6 GeV energy within the 3% energy acceptance of the energy compression beamline. As reported in Sec. 2.1, filling the PETRA IV ring in 10 minutes in Brightness mode sets the charge injection rate at $\mathcal{Q} = 2.6$ nC/s. For top-up operation, an injection rate as low as $\mathcal{Q} = 42$ pC/s would suffice. The total average beam power required to fill (top up) the ring is then $\mathcal{P}_{\text{beam}} = 6\ \text{GeV}\ \mathcal{Q}/e = 15.6$ W (0.25 W). The average power consumption of the LPA can be expressed then as

$$\mathcal{P}_{\text{LPA}} = \mathcal{P}_{\text{beam}}/\mathcal{E}, \tag{3.4}$$

where $\mathcal{E}$ stands for the total efficiency of the LPA system producing the beam. Considering that the vast majority of the energy invested for the LPA system is expended on the drive laser, the total efficiency can be further broken down in two contributing factors, the laser wall-plug efficiency $\mathcal{E}_{\text{wp}}$ and the laser-to-beam efficiency $\mathcal{E}_{\text{lb}}$. The former is the measure of how efficiently a laser source is converting electrical power into usable optical power. The latter refers to the percentage of the laser energy that is transferred to the electron beam which is finally stored in PETRA IV. Knowing the laser-to-beam efficiency, the required average laser optical power can be then simply calculated as $\mathcal{P}_{\text{laser}} = \mathcal{P}_{\text{beam}}/\mathcal{E}_{\text{lb}}$.

Laser-to-beam efficiency: Simulations for the described LPA design have shown laser-to-beam efficiencies of a few percent, comparable to the highest energy transfer efficiencies measured in LPA experiments [83, 84]. In particular, the start-to-end simulation shown throughout Secs. 3.2 and 3.3 for WP1 yielded $\mathcal{E}_{\text{lb}} = 2.7\%$. This case employed a laser pulse energy of 19.6 J to produce a 6-GeV electron bunch with 87 pC. Considering a realistic jitter and the energy collimation in the ECB, the final bunch charge injected into PETRA IV is 83.5 pC on average (Tab. 5), which results in a final average efficiency of 2.6%. Other working points have been explored in Appx. A.2 considering narrower guiding channels: Laser-to-beam efficiencies in the 2.6–3.6 % range were obtained in simulations employing laser pulses energies between 13 and 17 J. Additional simulation studies, performed to explore the efficiency limits of the LPA, reveal further optimization potential: by improving the laser matching to the plasma guiding channel, introducing the option of linear plasma channel tapering, and allowing for a tunability of the current profile of the accelerated beam by means of laser and plasma parameter changes, efficiencies up to 15% were obtained with laser energies as low as 10 J (250 pC bunches at 6 GeV) (see Appx. A.3).

Laser wall-plug efficiency: The laser wall-plug efficiency is subject of intense research and development [85]. Conventional Ti:Sa, flashlamp-pumped, high-peak-power lasers typical for LPAs such as BELLA and ANGUS, the LUX drive laser, feature a low wall-plug efficiency of order 0.1%. A path to higher ef-

ficiencies is the deployment of a new generation of diode-pumped lasers in Ti:Sa systems that allow to surpass the 1% [68] wall-plug efficiency threshold. Such systems are in operation, e.g., the High-repetition-rate Advanced Petawatt Laser System (HAPLS) [86] developed by Lawrence Livermore National Laboratory (LLNL) and installed in the Extreme Light Infrastructure (ELI) makes use of high-power diode array technology to deliver 30 J, 30 fs laser pulses at 10 Hz with a wall-plug efficiency of 1% [87]. According to our simulations, the pulse specifications of HAPLS surpass the requirements for producing 6 GeV bunches with about 80 pC charge within the acceptance, however the repetition rate would be insufficient to fill the ring in 10 minutes: the laser would need to operate at 32 Hz to achieve the required charge injection rate. To circumvent this limitation, either the filling time needs to be relaxed by a factor 3 (needing 30 minutes to fill the ring and lowering the availability of the ring by 1%) or the repetition rate increased by the same factor. For the latter, the HAPLS technology could still be used if the number of amplifiers is increased accordingly to operate in sync to provide the required repetition rate. A more interesting solution, adopted in the implementation plan (Sec. 4.2), is to develop new diode-pumped amplification stages for KALDERA [28] that directly run at 32 Hz. Using KALDERA as a seeder not only will benefit from its exceptional laser beam quality and operational performance, but will share construction and energy consumption costs: only 1 every 30 laser pulses produced by KALDERA will be amplified separately for PIP4.

Ring filling: Using $\mathcal{P}_{\text{beam}} = 15.6$ W for the average beam power needed to fill the ring in Brightness mode in 10 minutes, and $\mathcal{E}_{\text{lb}} = 2.6\%$ for the conservative laser-to-beam efficiency demonstrated in the simulations for WP1, the required average optical power is $\mathcal{P}_{\text{laser}} = 0.6$ kW. The baseline design of KALDERA aims to deliver 100 TW peak power (3 J in 30 fs) laser pulses at repetition rates up to the kHz level, i.e., 3 kW of average optical power. This is about 5 times higher than required to operate the plasma injector for the ring's fillings, albeit with substantially lower energy per pulse. Considering $\mathcal{E}_{\text{wp}} = 1\%$ for the wall-plug efficiency of a diode-pumped laser system, such as KALDERA or HAPLS, we obtain from Eq. (3.4) $\mathcal{P}_{\text{LPA}} = 60$ kW for the average power consumption of the LPA while filling the ring in Brightness mode. By keeping the same average power, in Timing mode, the plasma injector would complete the initial filling in about 4 minutes.

Top-up operation: During top-up, provided that the average beam power to deliver decreases substantially to only $\mathcal{P}_{\text{beam}} = 0.25$ W, the average power consumption of the LPA could be, in principle, as low as $\mathcal{P}_{\text{LPA}} = 1.2$ kW. However, as indicated in Sec. 3.5, the repetition rate of the laser in top-up mode shall not differ substantially from that used during the filling, in order to avoid stability issues. This implies that, during top-up operation, the plasma injector would run at full power during a short period of time, i.e., with a reduced duty cycle (see Tab. 6). As for the case of the RF injector in Sec. 2.2.1, it is yet to be investigated a low-power-consumption standby mode for the plasma injector, which allowed us to save energy between top-ups. Another possibility to take advantage of the reduced duty cycle between top-ups, is to use the LPA beam to feed another beamline to run parallel applications.

Cooling system: Apart from the electrical energy required to power the laser, a substantial contribution to the total power consumption comes from its cooling system (to operate at a stable temperature)[7]. In case of a diode-pumped laser system with an efficiency-optimized cooling solution, the estimated power consumption for cooling is 40 kW, about 66% of the total electric power employed by the laser system[8].

Laser laboratory: Another separated and substantial contribution to the total power consumption of the plasma injector is associated with the laser lab. This includes AC to stabilize air and humidity, and all the system-helper devices, such as racks, servers and motors. Based on the experience operating the ANGUS laser lab for

[7] This contribution to the total power consumption is separated from what is accounted through the wall-plug efficiency in Eq. (3.4).

[8] A similar ratio between cooling and electric power, ~60%, was employed during LPA experiments with the petawatt-class, flashlamp-pumped, BELLA laser at LBNL.

LUX and on the current commissioning of KALDERA, we estimate 50 kW for the average power consumption of the laser lab.

Redundancies: As in the case of the RF injector (Sec. 2.2.1), a number of redundancies would be required for the plasma injector to deliver high availability and long mean time between failures. However, this aspect of the design has not been studied yet, and it is not possible at the moment to estimate its influence on the average power consumption.

3.6.2. Beamline power consumption

The power consumption of the electron beamline can be estimated by analyzing the performance of similar systems already in operation at DESY. There are three major systems that have to be evaluated: magnets, vacuum, and RF. Overall, the plasma injector beamline will be comparable in size to and will have a similar number of magnets as the existing LUX beamline [16]. The latter utilizes between 2 and 4 kW for its dipoles and quadrupoles, when operating with electron energies between 200 and 400 MeV, or 10 kW per GeV. This number can be used as an estimate for the magnet power consumption, amounting to the total of 60 kW for the magnet system. Owing to a large pressure gradient from the plasma cell, the LPA beamline contains a differential pumping system with a relatively large number of vacuum pumps, most of which improve the vacuum in the vicinity of the plasma cell. It is expected that the plasma injector beamline will consume less than 20 kW for its vacuum pumps in full operation. The 50 MW peak power X-band RF system needed for the active energy compression is to consume about 40 kW on average, based on the available data from similar systems at FLASH and ARES at DESY [88]. Finally, there are a couple of minor power consumers that can also be accounted for. Temperature stabilization of the RF cavities and water cooling of magnet coils will take several kilowatt. As a conservative estimate, we can consider that the necessary cooling power might reach up to 15% of the electrical power, assuming cooling with 30° C water [89]. About 10 kW will be needed to power the control electronics: PCs, switches, etc. In total, the power consumption of the beamline can be estimated at about 145 kW.

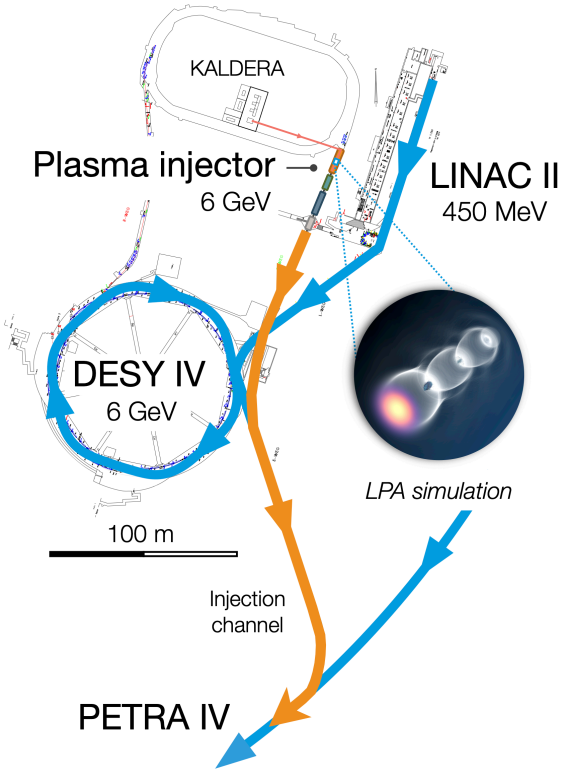

Figure 11. PIP4 alternative conceptual schematic. The plasma injector system would fit in an existing tunnel at DESY (G-weg), which can seamlessly connect with the main PETRA IV injection channel. This option minimizes the need for civil engineering interventions and enables near-term implementation. Ideally, locating the plasma injector next to the ring would eliminate the need for an extended beam transport line (compare Fig. 1)

Transfer line: Thanks to its comparably small footprint, a plasma injector would be ideally located directly next to the storage ring (Fig. 1). However, to implement a plasma injector without the need for significant new civil construction, we also consider locating the plasma injector next to the KALDERA laser lab, and reusing existing buildings to reduce expenses (Fig. 11). Transferring the beam from the suggested location at G-Weg to the PETRA IV injection point can take a substantial fraction of the energy consumption, depending on the number and strength of the magnets required to transport and steer the 6 GeV beam. Specifically, around 200 m needs to be covered by the transfer line before the beam reaches the PETRA IV storage ring. The exact path of the transfer line is not yet established, nor is the extent to which it can be shared with the RF injector. For reference, we quote the expected

power demands of the transfer line for the RF injector system, which amounts to 320 kW (Sec. 2.2.1). This value is comparable to the estimated power consumption of the whole plasma injector, including the laser system, the laser lab, and the X-band energy compression beamline.

Average power	
Laser system	60 kW
Laser cooling	40 kW
Laser lab	50 kW
Magnets	60 kW
RF system	40 kW
Magnets & RF cooling	15 kW
Vacuum system	20 kW
Miscellaneous	10 kW
Sum	**295 kW**

Table 7. Power consumption of the plasma injector when filling the PETRA IV storage ring at 32 Hz with a diode-pumped laser system.

Conclusion

Adding the LPA and beamline estimates, we expect the power consumption of the plasma injector, when filling the PETRA IV storage ring, to be around 295 kW (Table 7). Approximately half of this power would be used by the laser, including the lab and its cooling system. This value should be seen as a final attainable goal for a future Petawatt-class, diode-pumped laser system, which efficiently delivers the necessary optical power and repetition rate to fill the ring from scratch. In practice, the power consumption will be higher once the transfer line expenses and necessary redundancies to ensure high beam availability are factored in. Nevertheless, considering the 2.7 MW peak power consumption of the RF injector system for PETRA IV (Section 2.2.1), we conclude that the plasma injector has the potential to become an energy-efficient alternative.

4. Implementation roadmap

The simulations performed for the design of PIP4 described throughout Sec. 3 yielded promising results, demonstrating that the proposed design can be a competitive and compact solution for the future. For such a design, we rely on short-term perspectives for the technological development of the different components. The design thus extrapolates from what has been proven today to provide a promising solution for the future. To experimentally deliver the simulated beam parameters, it will be necessary to actively engage in the development of the key elements of the design, as well as to prepare the terrain for the implementation in the PETRA IV injection complex. In this chapter, we outline the roadmap for the development of the required technology and the implementation of the different components of the plasma injector for PETRA IV.

4.1. Project phases

The PIP4 implementation roadmap is organized into three progressive phases, each building upon the previous one and increasing in technological complexity. These phases are outlined in Fig. 12 and briefly described below:

Phase 1 — Technology demonstration: In this initial phase, the key components of the plasma injector will be demonstrated individually. The first models of the plasma target, integrating laser guiding and controlled injection, will be tested on a low-energy testbed system. This step serves as a precursor to the development of a scaled-down version of the PIP4 target, which will be driven by the KALDERA laser system. Additionally, a low-energy version of the energy compression beamline, utilizing an S-band RF structure, will be installed in the LUX system. This setup aims to reduce the energy spread and jitter of the electron beam by more than a factor of 10, achieving the energy bandwidth and stability levels necessary for the plasma injector.

Phase 2 — Plasma injector prototype: Building on the successes of Phase 1, the individual technologies will be integrated to form a complete plasma injector prototype, driven by the KALDERA laser system. Although this prototype will target a lower beam energy range (0.4 – 1.0 GeV), it will include all the critical components of the final PIP4 design. The plasma injector prototype could be installed in G-Weg. This strategic placement will allow it to be connected to the main beam transfer line from LINAC II to DESY II in L-Weg (see Fig. 13), enabling the possibility of early injection experiments in DESY II (see Fig. 12). As the commissioning of the plasma injector prototype progresses, operational injection tests would naturally follow, including running injection for extended periods of time. These operational tests will be key to providing further insight to assess the readiness of the technology for operation under realistic conditions.

Phase 3 — Plasma injector PETRA IV: The next step is to set up a dedicated plasma accelerator to directly inject electrons into PETRA IV at 6 GeV energy, with the ultimate goal of achieving full operational capability. The plasma injector for PETRA IV would be driven by a new laser system capable of delivering the required pulse energy, repetition rate and stability. This laser system, including the necessary redundancies to ensure high availability, shall be located in a dedicated new building next to the storage ring, as indicated in Fig. 1, thereby eliminating the need for an extended beam transport line. The preparatory phase for the development of this laser should start well in advance, running in parallel with Phase 2 (see Fig. 12). Alternatively, if more development time is required, we could upgrade KALDERA with a PW amplifier to meet the requirements of the plasma injector. This plasma accelerator would then be installed in G-Weg, and the 6 GeV beams would be transported, as shown later in Fig. 13, to the PETRA IV injection point. In any case, the plasma target would be upgraded to sup-

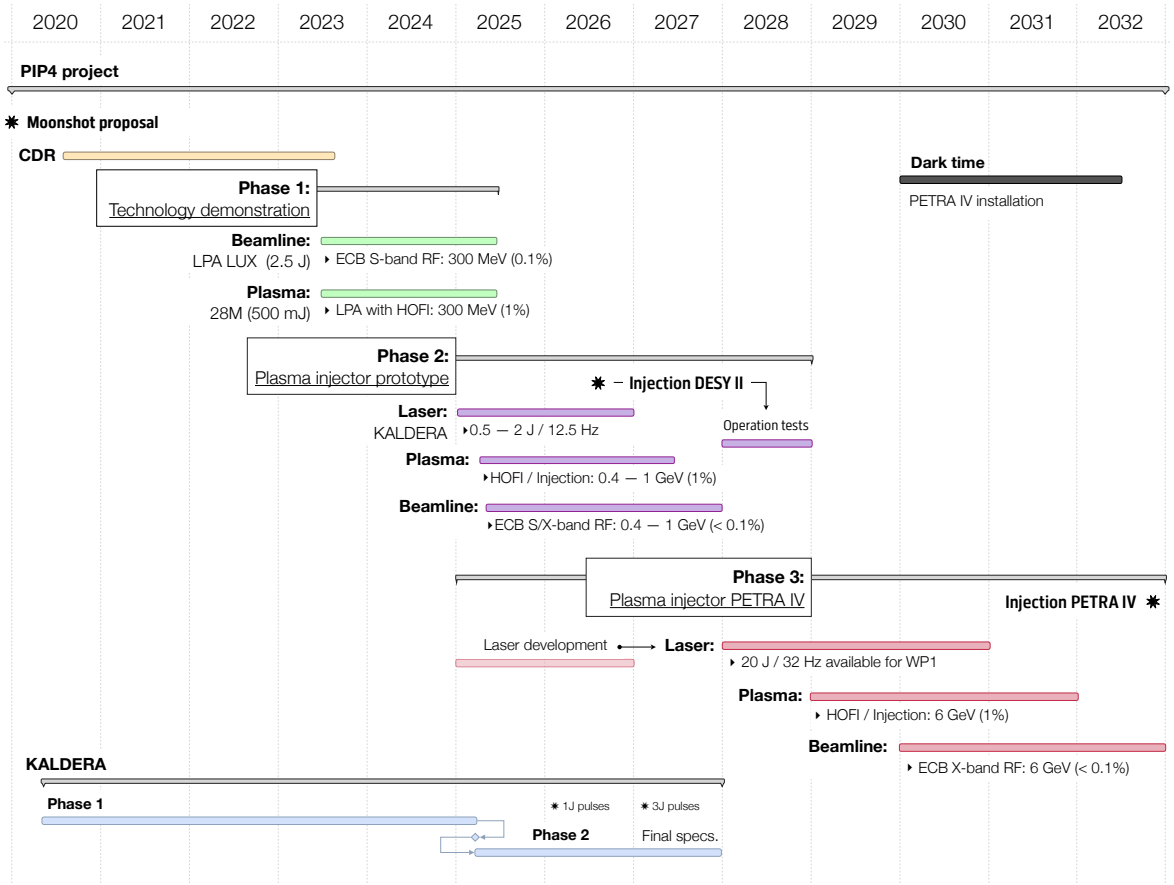

Figure 12. Preliminary timeline for the implementation of the PIP4 project (as of early 2024). External constraints such as the development of KALDERA and the PETRA IV installation shutdown are also shown.

port extended acceleration, and the energy compression beamline would be built using X-band RF technology to enable a compact setup.

4.2. Work packages

The tasks to develop throughout the different phases of the project are divided into three work packages: laser systems, plasma sources and beamline systems, that we discuss in the next sections.

Work package 1: laser systems

To achieve 6 GeV electron beams suitable for injection into PETRA IV, high-energy laser pulses with order 20 J are needed (Sec. 3.2). At those pulse energies, operating the plasma injector at a competitive level, capable of replacing the RF injector for rapid fillings of the storage ring, requires a relatively high repetition rate of 32 Hz (Sec. 3.5). Besides, the laser system must have a high wall-plug efficiency equal or greater than 1% to enable an energy-efficient plasma injector (Sec. 3.6). Last but not least, satisfying the high operational demands of PETRA IV requires exceptional stability to ensure high availability and long mean time between failures (MTBF)[1]. Such a system is not available today at DESY and developing a laser system capable of fulfilling all these requirements is one of the most challenging aspects of PIP4.

However, the KALDERA project sets the basis for the needed technological advance in this direction. KALDERA is DESY's new flagship LPA drive laser currently under development. It is based on Ti:Sa laser technology and will deliver 100 TW peak power (3 J in 30 fs) laser pulses, at repetition rates up to the kHz level. The very high repetition rates of KALDERA will allow the deployment of active stabilization and feedback systems, as they are commonly used in every modern accelerator today. KALDERA will be fully integrated into DESY's accelerator controls system. As a result, we expect laser

[1] The present storage ring, PETRA III routinely demonstrates 98–99% availability [90]. 99% availability and over 50 h MTBF seem reasonable goals for PETRA IV.

pulses of unprecedented reliability, reproducibility and quality, to drive application-ready, next-generation laser-plasma accelerators. In particular, KALDERA will be the driver of the first down-scaled version of PIP4, aiming to test the full-technology chain of the plasma injector during the Phase 2, culminating with the first injection performance tests in DESY II, with a reduced electron beam energy (0.4 – 1.0 GeV). For this reason, the development of the PIP4 project is closely entangled with that of KALDERA (see Fig. 12). Demonstrating injection into DESY II will be an outstanding milestone that will allow us to fully assess the performance of all the essential technology blocks of the PIP4. After this, the project will be ready to engage into the Phase 3: the development of the actual 6 GeV plasma injector for PETRA IV.

Ideally, upon successful completion of phase 1 and 2, a dedicated laser would be built to drive a plasma injector capable of supporting full PETRA IV operation, including filling and top up of the ring. To make this possible, a preparatory phase for the development of a future high peak power laser should start well ahead in time, aiming at being ready for the final implementation of the plasma injector for PETRA IV. This phase will push the boundaries of current laser technology, focusing on achieving the necessary pulse energy, repetition rate[2], and stability required for the final plasma injector.

However, if we find that even more development is required to address open questions discovered in earlier phases, we can also foresee to upgrade the existing KALDERA laser with an additional amplifier stage operating at a reduced repetition rate, using KALDERA as a seed laser. The Petawatt-class upgrade of KALDERA (KALDERA+) could take place in an extension of the current lab currently under development. Considering that the plasma injector will not necessitate the very high repetition rates of KALDERA (1 kHz), only a reduced fraction of the KALDERA pulses would be diverted to the KALDERA+ extension lab for further amplification at about 30 Hz. Nevertheless, the much higher repetition rates of KALDERA acting as frontend would allow us to implement active stabilization and feedback throughout the whole amplification chain, thus providing a significantly more stable system. The last laser pulse energy amplification stage would still be based on diode-pumping technology, in order to deliver the required levels of repetition rate and wall-plug efficiency.

[2]For example, 20 J pulse energy and 32 Hz repetition rate for the working point shown in Sec. 3.2

Work package 2: plasma sources

The experimental realization of the plasma source for PIP4 will require careful tailoring of the 3D plasma density structure. Shaping the longitudinal plasma density profile is crucial for initiating the injection of a high-quality electron beam at the start of the accelerator, while creating appropriate plasma waveguides for guiding the laser is necessary to reach multi-GeV acceleration. As discussed in 3.2, HOFI waveguides [26] provide a good foundational technology around which to base the plasma source owing to their ability to guide a spot of a few tens of microns over several hundred millimeters at densities of order 10^{17} cm^{-3} [91, 92]. There has already been promising results demonstrating the addition of a controlled injection structure into such an optically formed channel [60]. However, in the case of PIP4, significant further development will be required to increase the electron beam energy, quality, reliability and stability while also operating within a series of additional constraints such as the accelerator vacuum environment.

The plasma source for PIP4 will undergo staged development. Initially, a low energy 300 MeV prototype plasma source will be developed to test key concepts relating to accurately producing the plasma waveguide and injection structure. Several methods of tuning the plasma source will be investigated and compared before down-selecting. At this stage (Phase 1), the method of generating the injection structure will also be selected. Next, the most promising technologies will be incorporated into a scaled-down version of the PIP4 plasma source aiming at electron energies in the (0.4 – 1.0 GeV) range, using KALDERA as the drive laser (Phase 2). Finally, the full energy, 6 GeV, plasma source will be constructed building on the learnings from the two prototypes (Phase 3). In all cases, the LPAs associated to these

plasma sources will aim to generate electron beams with an energy spread of 1% of the peak energy. Combining robust operation at high repetition rates and developing improved tunability will be a central focus of these efforts, as this will allow us to leverage machine-learning-driven experimental optimization techniques, which have shown great promise for capitalizing on the full potential of LPAs [18, 56].

Work package 3: beamline systems

The energy compression beamline designed for the plasma injector will be tested prior to the start of the PETRA IV project during the technology demonstration Phase 1 (Fig. 12), in an independent proof-of-principle experiment that is currently in preparation at DESY. This demonstrator experiment will utilize the LUX LPA [17] to generate ~300 MeV average energy electron beams with a few per cent energy spread and stability. The demonstrator aims at validating the concept of energy spread reduction and stabilization by means of an active RF dechirper. It is expected from simulations that the addition of a chicane and an RF energy compressor to LUX will result in a permille-level of energy spread and energy stability, reducing the spectral bandwidth of the LPA beams by an order of magnitude. For convenience, we plan to utilize the readily available S-band (3 GHz) technology at DESY for the RF structure. Hardware installation is expected to start in spring 2024 with commissioning and data acquisition planned for 2025. This S-band RF based energy compression system could be reutilized in the low-energy plasma injector planed for Phase 2 of the project (see Fig. 12).

For the final 6 GeV plasma injector beamline (phase 3), we will use X-band technology due to its shorter wavelength and higher accelerating gradient, which enables the use of a comparably short RF structure (see Fig. 3). DESY already has experience operating X-band RF structures at ARES and FLASH [80]. Besides, additional experience could be gained by upgrading the RF structure to X-band for the plasma injector prototype of Phase 2. A setup using an X-band RF dechirper could make use of a 75-cm-long cavity similar to the CLARA-type 12 GHz accelerating structure [93, 94], powered by a 6 MW klystron and pulse compressor in a setup similar to the X-band TDS experiment at the ARES accelerator [95].

The 6 GeV plasma injector beamline will share the design of many components, such as magnets, instrumentation, kickers with the rest of the PETRA IV project. This approach allows saving the time and effort on the design of the hardware.

4.3. Risk assessment

Final laser performance: Developing an efficient, high-peak-power, high-repetition-rate laser system capable of operating the plasma injector during the fillings of the storage ring is one of the most challenging aspects of the project. Although laser systems with similar specifications are being developed today in some selected facilities such as the European Extreme Light Infrastructure (ELI) [86], the technology is not yet on par with the high operating demands of a world-class scientific instrument such as the proposed PETRA IV. However, with the development of KALDERA, DESY is taking a leading position to engage the development of the next generation of laser systems for plasma acceleration. Despite this progress, there remains a high risk in achieving the final laser performance required to completely replace the RF injector system. Considerable efforts, including collaboration with industrial partners, will be necessary to mature the laser system to a reliable operational state. For top-up operation, however, the risk is significantly lower because the requirements on the laser system are largely relaxed in terms of repetition rate, and laser systems with these characteristics are commercially available.

Plasma source: The development of a tailored plasma source is crucial to fulfill the minimum requirements of a high performance plasma injector. Generating a transverse plasma density structure suitable for guiding relatively small laser spot sizes will enable operation of the injector with lower energy pulses, which, in turn, will facilitate running the laser system at higher repetition rates. Besides, using an all-optical technique to generate the plasma structure will enable the accelerator to operate for

extended periods of time. For these reasons the plasma source development will be based around a HOFI plasma channel, as it is today the only technique that has demonstrated parameters compatible with the needs of PIP4. Currently, the development of HOFI channels is advancing at a high pace and encouraging milestones such as the acceleration of electrons to 5 GeV energy with <15 J energy pulses [61] have been recently demonstrated. There is a moderate risk, however, that the real laser guiding will differ from the idealized simulations, for example with higher-than-expected energy loss of the pulse during propagation due to leakage through the walls of the waveguide structure. Additionally, the fraction of energy coupled into the lowest order mode may differ from that in simulations. Both of these outcomes would necessitate a higher initial laser pulse energy to achieve the desired electron beam parameters. This effect has a direct impact on the overall energy efficiency of the system and on the feasibility of a plasma injector capable of filling the storage ring at a high repetition rate. Additionally, it is crucial to realize specific longitudinal profiles that allow for controlling the properties of the electron beams. Combining both transverse and longitudinal profiling with the desired performance is yet to be developed, and therefore, it brings an associated risk. However, first promising experimental results have already demonstrated the controlled injection of electron beams within a HOFI plasma waveguide [60]. With the development of PIP4, DESY engages a strong experimental program pursuing the development of optical plasma shaping technology, including HOFI plasma channels and profile tailoring for injection, which is designed to ensure that the required level of maturity for the plasma sources is achieved.

Beam charge fluctuations: Achieving sufficient beam charge stability from the LPA is of uttermost importance. For up to few percent energy fluctuations, the energy compression beamline (ECB) has been proven to be effective in simulations to significantly increase the charge throughput and reduce the bunch charge fluctuations, which would otherwise result from an aggressive momentum acceptance cut in the storage ring. The confidence on the conventional elements of the beamline is high and no significant risk is expected for this component of the plasma injector. However, while the ECB can significantly reduce the energy fluctuations of the beam, the intrinsic bunch charge variation resulting from jitters of laser and plasma parameters cannot be compensated, and mitigation can only be applied upstream. Thus, there is a moderate risk that the final performance of the LPA in terms of bunch-to-bunch charge fluctuations could be insufficient to comply with the PETRA IV requirements. The promising experimental results achieved recently at LUX for enhanced LPA beam stability and the prospects for yet better performing LPAs running at higher repetition rates and deploying active stabilization and feedback systems, offer great promise for a largely improved beam charge stabilization in the future.

Operating X-band RF: At the moment, DESY has a limited experience designing and operating X-band accelerating structures with the only exceptions being the TDS systems at FLASH and ARES. The cavities and RF hardware for these systems have been developed elsewhere, i.e. at CERN and PSI. Thus, using a relatively novel (for the laboratory) RF technology poses a minor technical risk. It can be mitigated by first gaining experience with commissioning and operating an X-band cavity in the scope of the plasma injector prototype for DESY II.

Laser-to-RF synchronization: Achieving the required 100 fs rms level of synchronization between the laser and the X-band RF system could be technically challenging in view of timing jitters and temperature fluctuations in the tunnel [96]. This poses a minor risk to the overall final beam quality and injection efficiency. A technical design of the subsystem that takes into account the positions of the laser and the RF systems, tunnel layout and infrastructure is needed to confirm attainability of the synchronization.

4.4. Integration into the PETRA IV complex

Since the PETRA IV baseline foresees injecting single electron bunches and not bunch

trains, operation with the plasma injector will not drastically differ from that with the RF injector chain. Yet, the low charge and high repetition rate of bunches from the plasma injector, when filling the ring, might pose additional requirements for the hardware of the synchrotron and its injection lines.

Injection stripline kickers: The design of PETRA IV fast stripline injection kickers seems optimal for injection of single plasma injector bunches into the storage ring. The baseline, commercial kicker pulsers are capable of operating at repetition rates higher than the required 32 Hz for filling the PETRA IV ring with the plasma injector. Due to the very short kicker pulse lengths of <3 ns no significant heat load on the injection kickers is to be expected at an increased repetition rate.

Injection septum: PETRA IV uses a series of two injection septa to achieve small beam separation and high injection efficiency: first, a DC Lambertson septum, and then a thin pulsed septum. The design of the DC magnet is not affected by the presence of the plasma injector option. The pulsed septum, on the other hand, has to be capable of withstanding the additional heat load on the septum blade when operated at 32 Hz repetition rate. It is foreseen that the PETRA IV pulsed injection septum design, which is currently under development, will include the possibility to provide sufficient cooling to handle such increased repetition rates. The pulse electronics of the septum are also foreseen to be capable of operating at a repetition rate of 32 Hz.

Physical aperture: Since the plasma injector beams are expected to have smaller transverse emittance than the beams from DESY IV there are no additional requirements on the physical aperture of the D-Weg transfer line and injection devices.

BPM resolution: Standard button BPMs are expected to be capable of measuring the 80 pC plasma injector bunches [97]. No additional beam diagnostics is therefore required in the D-Weg transfer line or the storage ring.

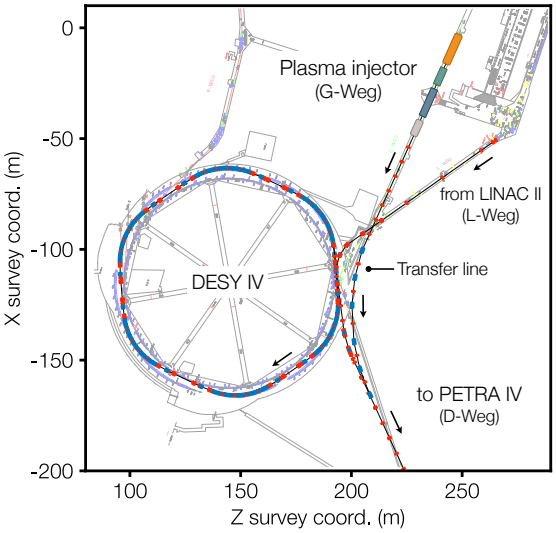

Figure 13. Preliminary layout of a transfer line for the 6 GeV LPA electron beam, when starting from its alternative position in G-Weg. Ideally, locating the plasma injector next to the ring would eliminate the need for an extended beam transport line (compare Fig. 1).

Location and transfer line: Ideally, the plasma injector would be located in its own building close to the storage ring to free up real estate on campus and save the energy-consuming electron beam transfer line (Fig. 1). Alternatively, the G-Weg tunnel at DESY has been identified as a possible location for the plasma injector (Fig. 13). The total length of G-Weg is ~90 m end to end, ample enough to accommodate both the LPA and the ECB plus the assisting components (diagnostics, cooling, electronics, X-band RF system, etc.). The drive laser can be transported into G-Weg from the nearby KALDERA laboratory, installed in the SINBAD hall. After the plasma injector, the transport beamline follows the G-Weg tunnel, bypasses DESY IV, and merges with the D-Weg beamline from DESY IV to PETRA IV – Fig. 13. The plasma injector beam would share the D-Weg transfer line and the injection hardware with the RF injector chain. Following the D-Weg line the beam can be injected into the storage ring using the same injection kickers as the electron beam from the RF injector chain. The LPA transfer beamline would not interfere with other beamlines or experiments. This solution for the location of PIP4 and the beam transfer line to the storage ring utilizes existing halls as much as possible and depends on a minimum amount of civil engineering. The necessary works to connect the plasma injector with the transfer line will need to be conducted during the PETRA IV

installation period, the so-called *dark time*, during which the whole PETRA III will be shutdown for the upgrade (see Fig. 12). The necessary magnets, bending dipoles and focusing quadrupoles, share the design with PETRA IV magnets to lower the costs. The standard PETRA IV diagnostics hardware is compatible with the LPA beam parameters and can be reused [97].

5. Summary and Conclusion

We have presented the conceptual design of a future injector for PETRA IV, based on plasma acceleration technology. The design relies on a state-of-the-art laser-plasma accelerator (LPA) to provide electron beams with ~80 pC charge at 6 GeV and 1%-level energy deviations, considering realistic jitters. Such design for the LPA combines precise longitudinal and transverse tailoring of the plasma profile to control the injection of suitable electron beams and guide the laser over extended distances to achieve high energy gain, respectively. The LPA is followed by a novel energy compression beamline (ECB) based on X-band RF technology to further reduce the overall energy fluctuations and the energy spread of the beam to an unprecedented sub-permille level, thus maximizing the charge stability and throughput into the storage ring. Altogether, the proposed plasma injector (LPA + ECB) takes less than 50 m and can be installed, ideally, in a dedicated building next to the injection point or, alternatively, in an existing tunnel at DESY, which conveniently connects with the PETRA IV storage ring.

Start-to-end simulations for a particular working point (obtained through Bayesian optimization), employing 20 J laser pulses to drive the LPA, demonstrate the feasibility and the performance of the design. We have estimated the average power consumption of the plasma injector running at 32 Hz to perform the most demanding task for PETRA IV: filling the ring from scratch with maximum charge. Considering the new generation of diode-pumped lasers in Ti:Sa systems with a wall-plug efficiency of 1%, we calculate 60 kW of average electric power consumed by the drive laser while filling the ring, just the 20% of the total 295 kW estimated for the power consumption of the entire plasma injector complex (Lab cooling, RF operation, magnets, vacuum system, etc.). In comparison with the RF injector system (LINAC + DESY IV), our design for the plasma injector could reduce significantly both the spatial and the energetic footprint of the injector complex, potentially enabling a more sustainable alternative for the future.

The operation of the plasma injector under optimal conditions relies on an efficient laser system to provide high-energy pulses at an elevated repetition rate. Although laser systems with similar specifications already exist, they are not yet ready for high-performance, routine operation as required for PETRA IV. For this reason, we first envision, as an intermediate step, the development of a plasma injector prototype – driven by KALDERA – capable of conducting first injection performance tests using DESY II as the target storage ring. These tests will provide further insight to assess the readiness of the technology for operation under realistic conditions.

Running the plasma injector at a high repetition rate with laser pulses around 20 J is identified as the most challenging aspect of the design. However, there is potential for improving the LPA parameters. By better matching the drive laser to narrow plasma channel waveguides and deploying optimized plasma density tapers, we have simulated working points that enable suitable electron beams with significantly improved efficiency, using only 10 J laser pulses. These reduced laser energy requirements will greatly facilitate the efficient operation at high repetition rates. Achieving competitive performance with the plasma injector will, therefore, require further advancements in high-power laser technology and additional optimization of the LPA. To address this, we plan to actively develop the key elements of the plasma injector through a dedicated R&D program following the conceptual design phase.

In conclusion, the hereby presented conceptual design of the plasma injector for PETRA IV demonstrates that high-accelerating-gradient LPA technology is at a stage where it warrants serious consideration as a compact and sustainable alternative to RF technology for cutting-edge scientific applications such as PETRA IV.

Acknowledgments

The authors would like to acknowledge the collaboration of many colleagues at DESY contributing with useful discussions and valuable information to the conception of the design, the organization and realization of the CDR, the power consumption estimates for the RF and the plasma injector, the considerations for the practical implementation of the plasma injector and its physical layout, as well as crucial information on the operation of the X-band RF system and the laser-to-RF synchronization. In particular and in alphabetical order: Ralph Aßmann, Karolin Baev, Riccardo Bartolini, Florian Burkart, Yong-Chul Chae, Heiko Ehrlichmann, Klaus Flötmann, Juan González Díaz, Matthias Hoffmann, Markus Hüning, Stephan Klumpp, Werner Kook, Gero Kube, Cédric Kula, Gregor Loisch, Rüdiger Onken, Kristjan Põder, Harald Reichert, Holger Schlarb, Kaja Schubert, Sven Sievers, Andreas Walker, Rainer Wanzenberg and Benno Zeitler. We also acknowledge the collaboration of Walter Wünsch and Alexej Grudiev from CERN who provided useful information on the X-band RF systems and cavities.

This research was supported in part through the Maxwell computational resources operated at Deutsches Elektronen-Synchrotron DESY, Hamburg, Germany. The authors acknowledge the Gauss Centre for Supercomputing e.V. [98] for funding this project by providing computing time through the John von Neumann Institute for Computing (NIC) on the GCS Supercomputer JUWELS at Jülich Supercomputing Centre (JSC).

A. Simulations

The scaling laws for LPAs operating in the blowout regime reviewed in Sec. B are useful expressions for quick design considerations. However, LPAs involve a range of physical processes, including laser-plasma interaction, ionization dynamics, electron beam injection, acceleration and transport, that are highly nonlinear and can be difficult to model analytically. Numerical simulations are therefore powerful and indispensable tools for modeling LPAs and understanding their complex physics. Specifically, particle-in-cell (PIC) simulations provide an adequate insight into the underlying mechanisms of LPAs, allowing us to optimize laser and plasma parameters, and predict the properties of high-energy electron beams. PIC simulations require high temporal and spatial resolution and are computationally expensive. Optimizing LPAs for the production of suitable beams under the right conditions requires a careful balancing of multiple parameters and, in principle, a large number of computationally demanding PIC simulation to converge to an optimum. Bayesian optimization (BO) is a method designed to reduce the number of simulations required to find the best-performing configuration and therefore is well suited to optimize the complex parameter space of particle accelerators. In recent times, BO has gained popularity within the accelerator community and, in particular, has been proven tremendously useful for optimizing LPAs with PIC simulations [18]. We have fully adopted this approach for the simulation studies performed for the PIP4 conceptual design and contributed in the process to further sharpen BO methods for the LPA community [71, 72].

In the following sections, we provide additional details on the simulations performed to assess the design of the PIP4. In Sec. A.1, we describe the process that led to the procurement of the simulated working point described through Sec. 3.2, which serves as the numerical basis of this conceptual design. In addition, we report in Sec. A.2 about additional working points obtained with narrow guiding channels compatible with the HOFI technique, which allow us to increase the energy transfer efficiency of the LPA and decrease the demands on laser pulse energy. In Sec. A.3, we further explore the limits of the energy transfer efficiency by performing extensive optimization scans under quasi-ideal conditions. Finally, Sec. A.4 includes additional details about the design of the energy compression beamline.

A.1. Working Point One (base case)

Working point one (WP1) is the baseline setup for the LPA described through Sec. 3.2. The procurement of WP1 starts by considering the setup implemented in LUX [17] as the best suited reference for the simulation studies for the PIP4. In order to achieve 6 GeV beams, the LPA setup needs to be scaled to lower densities, and laser guiding capabilities have to be added (Sec. B.5). According to Eq. (B.7b) for the electron energy gain in a depletion limited scenario, reaching 6 GeV energies would require to operate around $n_p \approx 2.0 \times 10^{17}$ cm^{-3} plasma density. Due to the increase of the plasma oscillation wavelength $\propto n_p^{-1/2}$ (Sec. B.3), the laser pulse length and spot size are scaled accordingly, while keeping the same laser peak intensity.

Plasma profile: The plasma target setup uses as a basis the design utilized at LUX for optimal beam-loading demonstration [17, 18]. This plasma target consists of two sections: first, a gas mixture of hydrogen and nitrogen forms a density spike where electron beam injection occurs, and second, a longer and uniform hydrogen gas section, which sustains the plasma wakefield for the acceleration of the beam up to the design energy. After the acceleration, the electron beam is released through a tailored plasma density downramp to reduce its divergence and mitigate the chromatic emittance increase during the free drift toward the beamline (Sec. B.7). As mentioned earlier, to reach 6 GeV, the plasma density is downscaled by

a factor 5. Accordingly, the length of the profile is scaled by a factor $\sqrt{5}$ (this affects the scale length of the density transitions, i.e. the ramps). In addition, the plasma plateau length was set to 28 cm to allow for reaching beyond laser pulse depletion at this plasma density (see Sec. B.4). This rescaling of the system provides an appropriate starting point, but the actual values of the plasma density and other plasma target parameters are determined through the optimization process described in Sec. A.1.1.

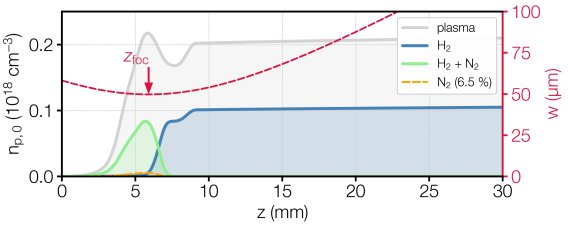

Figure 14. Configuration of the plasma target providing optimized electron beams at 6 GeV. The longitudinal distribution of the different gaseous species forming the target and the resulting plasma density are shown together with the laser spot size evolution in vacuum for the first 3 cm of the plasma target.

Guiding channel: A parabolic transverse modulation is added to plasma target profile according to the formula: $n_p(z,r) = n_{p,0}(z)[1 + r^2/(\pi r_e n_{p,0} w_m^4)]$, where r_e is the classical electron radius and w_m is the matched spot size. As discussed in Sec. B.6, this is the appropriate shape to match a Gaussian laser pulse driving a plasma wake in the linear regime. The matched spot size of the parabolic channel is set to $w_m = 50\,\mu\text{m}/\sqrt{n_{p,0}(2\times10^{17}\ \text{cm}^{-3})}$. This expression follows the scaling of w_m with the on-axis plasma density found experimentally for HOFI channels in [27] (see Sec. B.6.2).

Drive laser: The laser pulse is modeled with a flattened Gaussian beam [76] (order 100) with $\lambda_0 = 0.8\,\mu$m wavelength and linearly polarized in the horizontal direction. The starting values for the laser parameters are the result of rescaling the system to lower densities as described above. Thus, the laser pulse has peak power $P_0 = 345$ TW, spot size $w_0 = 50\,\mu\text{m} = w_m$, Rayleigh length $z_R = 9.8$ mm and peak vector potential at focus $a_0 = 2.03$. The starting laser duration was $\tau = 63.5$ fs (74.7 fs in fwhm) and the energy 27.5 J, but these will be varied during the optimization process.

Simulation configuration: Individual simulations are performed with the spectral, quasi-cylindrical PIC code FBPIC [70] in a Lorentz-boosted frame [99, 100] ($\gamma_{boost} = 13$) with two azimuthal modes. The grid resolution was fixed to $\Delta z = 0.15/k_0 = 0.02\,\mu$m in the longitudinal direction, with k_0 the laser wavenumber. In the transverse direction, the resolution was set to $\Delta r = 0.15/k_p$, depending on the plasma density. The hydrogen and nitrogen species were simulated using 24 and 384 macro-particles per cell respectively. The length of the simulation box was fixed to 134 μm in all simulations. Because the laser focal position, z_{foc}, will vary, the size of the box is set to 2.65 w_{start}, with $w_{start} = w_0\sqrt{1+(z_{foc}/z_R)^2}$, the laser spot at the start of the simulation and z_R the laser Rayleigh length.

A.1.1. Bayesian optimization

While the scaling discussed in the previous section provides correct orders of magnitude for laser and plasma parameters, it is necessary to tune the parameters of the simulation to provide beams with exactly 6 GeV energy, at optimal beam-loading conditions to achieve high efficiency and low energy spread. Also, in order to facilitate the operation at a relatively high repetition rate, it is important to minimize the laser energy employed in the LPA. To achieve this task, the key parameters of the plasma target and the drive laser have been subjected to a Bayesian optimization procedure [18] using FBPIC simulations and the highly scalable optimization library OPTIMAS [71, 72, 101], which uses Ax [102] for the Bayesian optimization algorithms and LIBENSEMBLE [103] to coordinate the simulation batches.

Five parameters were exposed as input parameters for the optimization: the reference plasma density value n_p, the peak density of the first plasma spike n_{peak}, the nitrogen dopant concentration N_{dop}, the focal longitudinal position z_{foc} and the energy of the drive laser pulse E_L, are scanned to find the point in parameter space which maximizes the objective function

$$f = S_\Delta/\hat{\sigma}_p/\hat{E}_L\,, \tag{A.1}$$

where $S_\Delta = Q_\Delta/\Delta p$ is the average spectral density of the beam, with Q_Δ the charge of the beam in the momentum interval Δp. The momentum interval Δp used in the analysis is defined as $\Delta p = 2.35\ \sigma_p$ with $\sigma_p = 1.48\ \sigma_p^{\mathrm{MAD}}$, and σ_p^{MAD} the median absolute deviation of the momentum distribution. It shall be noted that with this definition σ_p (Δp) coincides with the rms (fwhm) when the distribution is Gaussian. The relative average deviation with respect to the goal momentum $p_{\mathrm{goal}} = 6$ GeV/c is defined as $\hat{\sigma}_p = \sqrt{(\sigma_p/\bar{p})^2 + (1 - \bar{p}/p_{\mathrm{goal}})^2}$. Finally, $\hat{E}_{\mathrm{L}}$ is the laser energy relative to the base case, e.g., $\hat{E}_{\mathrm{L}} = 0.5$ means that the laser pulse has half the energy of the base case. With this definition for the objective function (Eq. (A.1)), the optimizer will search the parameters that yield beams with narrow and dense spectra peaked at 6 GeV, favoring a reduced laser energy.

Optimizing injection and plateau length: In a first optimization pass, the total length of the plasma plateau was set to a sufficiently large value (28 cm) so that the LPA beam would reach 6 GeV before the end of the plateau. No exit ramp was simulated in this case, and the simulations stopped at the end of the plasma plateau. For each simulation, the witness beam was analyzed at different z positions along the propagation to determine the point at which the objective function f is at its minimum. By construction, in all practical cases, this is the point at which the beam reaches 6 GeV. For this optimization task, we chose to minimize the laser energy by adjusting the laser duration while keeping the peak intensity. The laser peak intensity primarily governs the plasma wakefield excitation regime and, to some extent, the properties of the injected beam. Additionally, since the laser depletion length depends directly on the laser duration (see Sec. B.4), minimizing τ is an effective way to match the acceleration length to the depletion length, ensuring that all the laser energy available to efficiently drive the wakefield is exploited for the acceleration of the witness beam. For this pass, the parameter space was relatively wide with $n_p \in [1.97, 2.36] \times 10^{17}$ cm^{-3}, $n_{\mathrm{peak}} \in [1.05, 1.15]\ n_p$, $N_{\mathrm{dop}} \in [0.1, 20]$ %, $z_{\mathrm{foc}} \in [0, 18]$ mm and $\tau \in [31, 63]$ fs ($E_{\mathrm{L}} \in [13.8, 27.5]$ J). A suitable optimum was found after around 300 simulations with the following parameters: $n_p = 2.02 \times 10^{17}$ cm^{-3}, $n_{\mathrm{peak}} = 1.07\ n_p$, $N_{\mathrm{dop}} = 5.6$ %, $z_{\mathrm{foc}} = 7.4$ mm and $\tau_{\mathrm{fwhm}} = 53.3$ fs ($E_{\mathrm{L}} = 19.6$ J).

Fine tuning with plasma exit: In a second pass, the exit ramp is added to simulate the beam release into vacuum. This ramp is identical in shape to the LUX case, but its length was increased proportionally to the increase in betatron wavelength of the 6 GeV beam, i.e. $\propto \sqrt{\gamma/n_p}$. The length of the plasma plateau was added as an optimization parameter, varying around the previously found optimal value, to provide certain flexibility to reach the goal energy after the inclusion of the ramp. The rest of key parameters governing the LPA beam were further constrained around the optimal case found during the first pass: the laser focal position $z_{\mathrm{foc}} \in [3.9, 7.9]$ mm, the laser energy $E_{\mathrm{L}} \in [19, 21]$ J, the plasma density $n_p \in [1.95, 2.10] \times 10^{17}$ cm^{-3}, the plateau length $L_{\mathrm{plat}} \in [21.5, 21.8]$ cm and the dopant concentration $N_{\mathrm{dop}} \in [5.5, 7.5]$ %. The laser pulse duration was kept fixed to the previously found optimal value of 53.3 fs (fwhm), and thus, the laser energy variations in this optimization run are directly related with changes in the laser peak intensity. This optimization run performed a total of 480 simulations using the same Bayesian optimization algorithm as during the first pass. The values of the parameters at the optimum are: $z_{\mathrm{foc}} = 5.95$ mm, $E_{\mathrm{L}} = 19.6$ J, $n_p = 2.02 \times 10^{17}$ cm^{-3}, $L_{\mathrm{plat}} = 21.7$ cm and $N_{\mathrm{dop}} = 6.5$ %. Figure 14 shows the optimal plasma target profile and laser focal position for the first 3 cm.

Optimal beam: The phase space of the resulting beam is shown in Fig. 4(c). It features 87 pC of charge and 0.5% energy spread. Its normalized emittance in the horizontal (vertical) plane is 4.6 μm (1.7 μm). The beam divergence is 0.22 and 0.12 mrad in the horizontal and vertical planes, respectively. The total laser-to-beam energy transfer efficiency is 2.7%. As discussed in Sec. 3.2, the low energy spread of the optimal beam is the result of a net integrated beam loading effect after the acceleration, which result in a negligible energy-time correlation

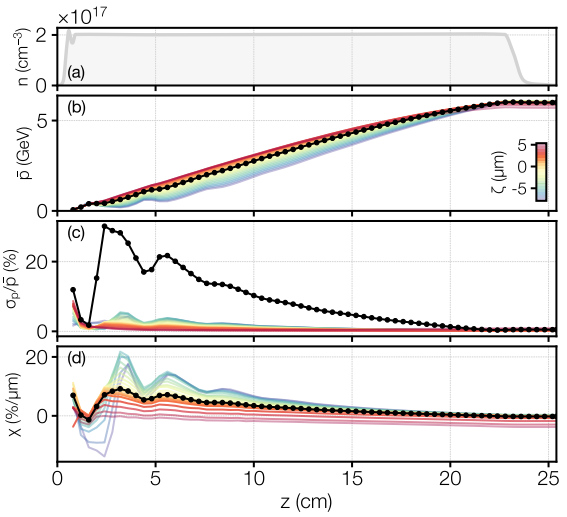

Figure 15. Plasma density profile (a). Average longitudinal momentum of the beam (b). Relative energy spread (c). Chirp (d). Sliced quantities are shown in colors, overall properties in black.

(chirp) in the longitudinal phasespace of the beam. The evolution of the average momentum, the relative energy spread and the chirp versus the propagation distance is shown in Fig. 15 (d). The beam accumulates a positive chirp in the early stages of the acceleration, which is progressively compensated for as the power amplification of the laser intensifies the plasma wakefield.

A.1.2. Jitter and tolerance analysis

By construction, the simulation data obtained during the optimization process offers a sensible and efficient sampling around the optimum. To implement jitter analysis capabilities, the information provided by the simulations was analyzed to obtain a functional dependency between the relevant beam parameters (average energy, energy spread, charge and chirp) and the varying input parameters. This relationship between inputs and outputs was modeled using Gaussian process regression [104]. The obtained surrogate models capture with high fidelity the response of the beam parameters to variations on the input parameters around the optimum, and hence, allow us to investigate the impact of different degrees of jitter on every possible combination of the input variables, without the need of performing additional costly PIC simulations.

To evaluate the effect of the input jitter on the LPA beam and estimate the tolerances of our setup, we proceeded first considering only the statistical moments of the beam spectra, as given directly by the surrogate models. By independently varying the jitter of each input parameter, we generated different random (Gaussian) sets of beam spectra to calculate the average charge throughput and bunch-to-bunch charge variation for each jitter set. On the one hand, the charge throughput is directly related with the overall energy efficiency of the plasma injector (see Sec. 3.6). On the other hand, the bunch-to-bunch charge variation has a direct impact on the bunch-to-bunch charge variation of the stored beam in PETRA IV (see Sec. 3.5).

This jitter analysis, enabled by the surrogate models, allowed us to determine a set of jitters on the most important input variables that represents the expected (and tolerable) beam stability of the LPA. The selected jitter sample consists on a multi-variate Gaussian distribution centered at the optimal values with standard deviations 0.75 mm, 0.75% and 0.75% in the laser focal position, the laser energy and the plasma density, respectively. Fig. 16 shows the result of evaluating the four surrogate models for the beam average energy, relative energy spread, charge and central chirp, over a generated jitter sample of 1000 points. Figure 16 also shows the models when only one input parameter is varied at a time. Variations in the laser energy and the plasma density have a similar effect: increasing (decreasing) their value with respect to that of the optimally beam-loaded case results in injecting more (less) charge in the witness beam. In turn, the excess (lack) of charge in the witness beam results in a higher (lower) degree of beam-loading, and thus, in a positive (negative) chirp, a lower (higher) net energy gain and a higher projected energy spread. Although the effect of the laser energy and plasma density jitter is qualitatively comparable, we observe a higher dependency of the energy of the beam on the plasma density, which dominates the fluctuations on the average energy of the beam for the jitter sample shown in Fig. 16. The effect of a varying laser focal position on the beam parameters is more intricate, as it affects the guiding of the drive laser, and thus, the average wakefield witnessed by the beam and, as a result, the integrated beam-loading effect over the acceleration length. The injected

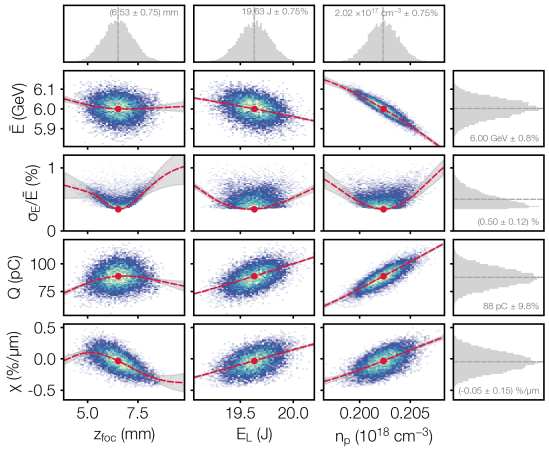

Figure 16. Surrogate models for the beam average energy, relative energy spread, charge and central chirp, evaluated over a random sample on three of the input parameters: the laser focal position, the laser energy and the plasma density. The dashed lines show the model when only the corresponding parameter is varied. The grey shades represent the uncertainty of the models. The position of the optimum is shown by the dot.

charge is maximum at the optimal point and decreases slightly when the focal position moves forward or backward. The opposite effect is observed in the beam energy and the energy spread, which reach a minimum at the optimal point. The central chirp, however, is slightly positive (negative) when the focal position is advanced (delayed).

The approach described above has also been used to model the effect of LPA jitters on the beam transport and injection into the ring, without resorting to expensive PIC simulations. To this end, the nominal WP1 beam is modified at the end of the LPA to artificially include the jitters on the four beam properties shown in Fig. 16 (based on the surrogate models). The total projected spectrum of the beam collection has an average energy of 5.993 GeV and 1.04 % rms, with an average bunch charge of 87.6 pC and 9.7 % rms. The generated beams are further tracked through the energy compression beamline as described in Sec. 3.3 to yield the final spectra of the beams that go to the PETRA IV ring. In the process, an additional pointing angle jitter of 0.2 (0.1) mrad rms was introduced in the horizontal (vertical) plane, and a timing jitter of 100 fs rms between the LPA beam and the RF signal. As a result of all the jitters at play, the simulated LPA bunch charge distribution inside the PETRA IV acceptance has 83.2 pC average and 10.7 % rms (see Sec. 3.3). The total charge throughput into PETRA IV is 95.0 %. This result is in agreement with the one obtained by just considering the statistical moments of the beam's spectra.

The results of the jitter analysis using surrogate models have been validated by performing a set of 1000 PIC simulations followed by their corresponding tracking simulations through the beamline. After the LPA, the total projected spectrum of the simulated beam collection has an average energy of 5.999 GeV and 0.96 % rms, with an average bunch charge of 86.5 pC and 9.8 % rms. Figure 3 (b) shows the spectra of the collection of 1000 beams simulated with FBPIC. After the ECB, the fully start-to-end simulation jitter sample result in an averaged injected charge of 83.5 pC with 10.0 % rms and a total charge throughput of 96.5 %, with all jitters included as before. These numbers are very close to those obtained with the surrogate modeling approach, thus validating its applicability to the jitter tolerance analysis. Figure 3 (c) shows the final spectra of the beams that go to the PETRA IV ring.

In summary, we have exploited existing simulation data from Bayesian optimization to build surrogate models for the beam parameters, using Gaussian processes. This approach allowed us to study the impact of the different combinations of jitters to determine a representative set for the expected performance of the setup. Encouragingly, all the selected values of jitter seem to be well in reach of what has been already demonstrated experimentally. At LUX, a focal position jitter of $\sim$ 150 μm (rms) was measured in experiments [17]. This jitter is expected to scale as the Rayleigh length of the laser, which will be about five times longer for the PIP4, matching the 0.75 mm that we considered. The laser pulse energy jitter measured at LUX was 0.6 % (rms), which is slightly smaller than the 0.75 % considered here. Finally, a jitter in plasma density <1 % will be required. The experimental jitter analysis performed for LUX indirectly suggests that variations in plasma density can be kept well below this limit.

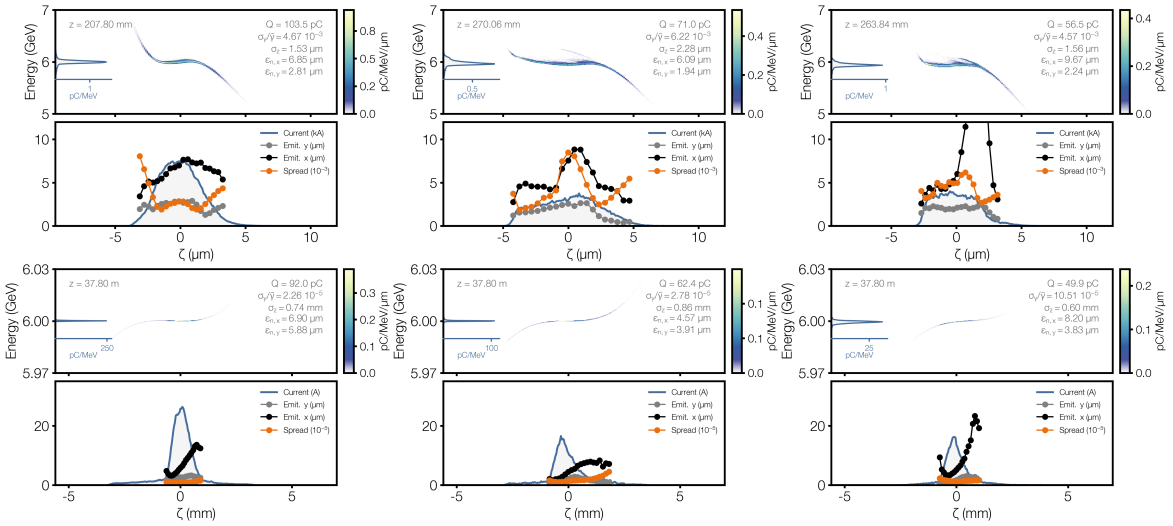

Figure 17. Optimized longitudinal phase-space of the beam right after the LPA (top) and after the ECB (bottom), for three different laser energies: 17.1 J (left), 14.8 J (middle) and 13.1 J (right).

A.2. Working Point Two (narrow channel)

Additional optimization runs were performed using FBPIC simulations for the same LPA setup of Sec. A.1, except for a narrower guiding channel of matched spot size $w_m = 40\,\mu m$. This choice is in good agreement with experiments exploring laser guiding with HOFI channels [27] for plasma densities around 2×10^{17} cm^{-3}. Accordingly, the drive laser focal spot size was adjusted to $w_0 = 40\,\mu m = w_m$. This allows for either maintaining a similar a_0 with reduced laser pulse energy or for increasing a_0 with equal laser energy[1]. In either case, a narrower guiding channel was chosen to reduce the laser energy required to reach 6 GeV and to improve energy-transfer efficiency. For this purpose, a new Bayesian optimization scan to optimize the injection and the plateau length was done as in Sec. A.1.1, with a relatively wide range of varying parameters: the laser focal position $z_{foc} \in [0, 10]$ mm, the laser energy $E_L \in [14, 20]$ J, the plasma density $n_p \in [1.8, 2.2] \times 10^{17}$ cm^{-3} and the dopant concentration $N_{dop} \in [0.1, 20]$ %. The peak density of the first plasma spike was fixed to $n_{peak} = 1.10\, n_p$ and the laser pulse duration was fixed to 53.3 fs (fwhm). For this optimization we changed the objective function to

$$f = \sqrt{Q_\Delta}/E_L^2/\hat{\sigma}_p\,. \tag{A.2}$$

We would like to note that the energy efficiency of the LPA goes as Q_Δ/E_L. However, in Eq. (A.2), we take the square root of the charge in the numerator and the laser pulse energy squared in the denominator. This choice for f maximizes the efficiency while prioritizing a reduced laser energy over an increased bunch charge. Operating with lower energy pulses would facilitate reaching the required average power to fill the ring (see Sec. 3.6.1). The factor $\hat{\sigma}_p$ in the denominator ensures maximizing the spectral density around 6 GeV, as in Sec. A.1.1.

This optimization run performed a total of 480 simulations. The best ranked simu-

Working points	WP1	WP2a	WP2b	WP2c
Laser				
Energy / J	19.6	17.1	14.8	13.1
Spot size / µm	49.8	39.1	41.6	39.2
Duration / fs	53.3	53.3	53.3	53.3
a_0	2.0	2.4	2.1	2.1
Focal pos. / mm	6.0	5.1	6.9	5.8
Plasma				
Density / 10^{17}cm^{-3}	2.0	2.1	1.9	2.1
Length / cm	21.7	16.9	23.1	22.5
Beam				
Energy avg. / GeV	6.0	6.0	6.0	6.0
Energy spread / %	0.48	0.47	0.62	0.46
Charge / pC	87	104	71	57
Emittance x / µm	4.6	6.9	6.1	9.7
Emittance y / µm	1.7	2.8	1.9	2.2
Efficiency / %	2.7	3.6	2.9	2.7

Table 8. Summary of parameters for the selected working points.

[1] To conveniently resolve the plasma wake of this narrow channel and potentially more intense regime (with higher a_0), the grid spacing in radial direction was set to $\Delta r = 0.06/k_p$.

lated beam is shown in Fig. 17 (left). With a score of $f = -2.6$, the beam features a relatively high charge 104 pC and a narrow energy spectrum at 6 GeV with relative spread equals to 0.5%. The employed laser energy is 17.1 J, which substantiates a considerable total laser-to-beam energy transfer efficiency increase to 3.6%, about 40% more than that of the working point shown in Sec. A.1. This optimal case is followed by another one scoring $f = -2.3$, and featuring significantly less laser energy, 14.8 J, albeit a reduced beam charge, 71 pC, and slightly higher relative energy spread, 0.6% (Fig. 17 (middle)). The efficiency is 2.9% in this case. Both beams have been tracked through the ECB to yield a highly compressed energy spectrum with 0.002% and 0.003% relative spread, respectively, and no significant emittance deterioration. The charge throughput is 88% in both cases.

A final optimization run was performed to push the laser energy to the minimum. In this case we changed the scanned laser energy range to $E_L \in [12, 18]$ J and added the plasma peak as a varying parameter, $n_{peak} \in [1.02, 1.12]\ n_p$, to give more flexibility to the witness beam injection. With a total of 480 simulations, the best scoring beam of this optimization run yielded $f = -3.1$, featuring 57 pC charge, 0.5% relative energy spread and 13.1 J laser energy (Fig. 17 (right)). The laser-to-beam energy transfer efficiency is 2.7%, which is at the same level than the working point in Sec. A.1, but using 35% less laser energy. The tracking simulation through the ECB yielded a final energy spread of 0.010% and a charge throughput of 88%.

These results substantiate that, by deploying narrow guiding channels, a significant reduction of the laser pulse energy requirements can be achieved, which will facilitate the operation at high repetition rates.

A.3. Limits of energy efficiency

The working points shown in Secs. A.1 and A.2 are the result of the optimization of the beam energy spread and the energy transfer efficiency of a specific LPA setup, representing the foreseeable state of the art. We have shown that, providing that effective HOFI plasma waveguides are deployed for the guiding of 13–20 J laser pulses under 40–50 μm matched spot sizes, suitable electron bunches with 50–100 pC charge could be produced and delivered to PETRA IV (Sec. A.2). However, the operational requirements of PETRA IV (see Sec. 3.5) would prescribe running such LPA at ∼30 Hz during the initial filling, which is a challenge from the laser technical side. The Petawatt-class laser HAPLS [86] installed at ELI, for example, is expected to deliver 30 J pulses at 10 Hz, but as of today, only about 3 Hz has been demonstrated. On the other hand, the KALDERA laser, currently being assembled at DESY, is designed to deliver 3 J energy pulses at up to 1 kHz. So it seems much more feasible to run lower energy laser pulses at high repetition rate with the current technology. For this reason, it is relevant to explore what could be improved in the LPA design to enable the use of lower-energy pulses that can be operated at a higher repetition rate.

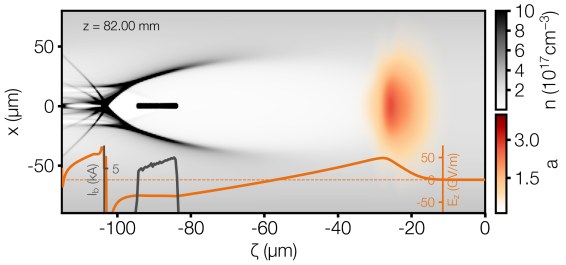

Figure 18. WAKE-T simulation snapshot showing the envelope of the drive laser, the wake of plasma electrons and the injected bunch after 82 mm of propagation. This case corresponds to a 19.5 J laser pulse and a matched spot size of 50 μm.

In this Section we report on dedicated optimization studies performed with WAKE-T [105], with the aim to study the theoretical limits of the LPA to provide suitable beams for PETRA IV at 6 GeV. WAKE-T is a fast particle tracking code for plasma-based accelerators that allows for inexpensive simulations (few minutes on a single CPU core) by using a gridless quasistatic plasma wakefield model with 2D cylindrical symmetry [106] and a laser envelope model [107]. Thus, extensive WAKE-T simulation scans and optimizations can be carried out in just a few hours on modern high-performance computing nodes, where 10s of simulations can be executed concurrently on the many CPU cores available.

Our case study consists of a Gaussian laser

driver focused down to the matched spot size of a perfectly parabolic plasma profile, transversely, and perfectly flat-top, longitudinally. With this configuration, the laser is expected to be optimally guided (matched) through the entire plasma target. The witness beam features a longitudinally trapezoidal profile with variable front and rear currents. The length of the beam is fixed to 10 μm. The witness beam is *artificially* injected at a variable phase position within the plasma wakefield at the beginning of the plasma target, and matched to the focusing strength of the plasma blowout (the ion channel). With this configuration, the system is designed to operate under quasi-ideal conditions in order to explore the theoretical limits for achieving 6 GeV beam energy with minimal energy spread and maximal energy transfer efficiency. For a given set of laser and plasma parameters, each optimization task searches the witness beam parameters that minimize the quantity $f = -Q_\Delta/\hat{\sigma}_p$ (see definitions in Sec. A.1.1), by varying the front and rear currents, and the phase position of the beam. Fig. 18 shows a representative snapshot of one of the optimal simulation cases.

Three sets of optimization tasks have been performed for three laser guiding channels with matched spot sizes of 80 μm, 50 μm and 40 μm, all of them at a plasma plateau density of $2 \times 10^{17}\text{cm}^{-3}$. The 80 μm case represents the maximum waveguide strength attainable by a capillary discharge at the design density. The 50 μm and 40 μm cases are representative of the higher waveguide strength attainable with HOFI channels. For each set, different optimization tasks were performed for different values of the laser pulse energy. The laser pulse duration was fixed to 33.6 fs (fwhm) and the initial length of the witness beam to 10 μm in all cases. Fig. 19 shows a summary of the results. For all cases shown, the final average energy of the witness beam is 6 GeV and the relative energy spread is below 0.5%. We observe a clear dependency of the energy transfer efficiency on the initial peak vector potential of the drive laser. Above 5% efficiency is achieved at $a_0 \sim 2.5$ for the 40 and 50 μm matched spot size cases, which corresponds to a laser energy of 12 J and 19 J, respectively. The cases with 80 μm spot size did not reach a high efficiency in the laser energy range below 35 J. This result demonstrates the importance of narrow HOFI channels to reach a high energy efficiency with a reduced laser pulse energy.

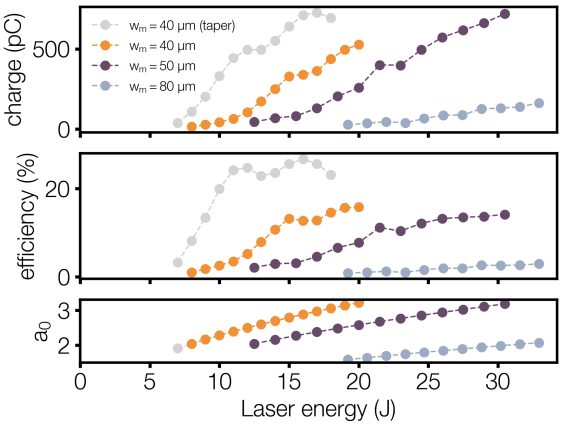

Figure 19. Summary of the optimizations performed with WAKE-T. Witness bunch charge (top), energy transfer efficiency (middle) and initial peak vector potential of the laser (bottom), as a function of the initial laser energy, for 80 μm, 50 μm and 40 μm matched spot sizes. An additional case with a 40 μm matched spot size and a linear density taper is also shown.

In order to further exploit the limits on laser energy to achieve 6 GeV energy beams with low energy spread and high energy transfer efficiency, we added a linear plasma density taper as variable parameter to the optimizations for the 40 μm matched spot size case. The results are also shown in Fig. 19 as a function of the laser energy. Because the plasma wavelength scales inversely proportional to the square root of the plasma density, tapering the plasma density allows the witness beam to stay longer in the highly-accelerating phase of the wakefield, partially compensating for the dephasing effect. In this way, higher energy gains can be attained with lower energy lasers and more charge can be accelerated under average beam-loading conditions. The simulations show that efficiencies above 5% could be achieved with 8 J laser pulses.

These idealized simulations confirm our previous findings that narrow plasma channels enable higher efficiency (see Sec. A.2). Furthermore, they demonstrate that adding a longitudinal taper to the density profile would allow for a substantial increase of the energy-transfer efficiency.

A.4. Beamline design

Tracking of the LPA beams through the beamline has been performed using the OCELOT tracking code [79], taking into account up to second-order beam optics, RF, collimation, and coherent synchrotron radiation (CSR) effects. The beams are modeled as an ensemble of macroparticles of variable charge, imported directly from the FBPIC [70] LPA simulations. Lattice elements: quadrupoles, dipoles, sextupoles, and the RF cavity were modeled by linear and second order maps with the transverse focusing of the RF taken into account. For the present conceptual design we neglected magnetic errors and imperfections. Lattice layout and optics functions are shown in Fig. 5(b). CSR effects were simulated using a 'projected' 1D model [108] which calculates the longitudinal wakefield of the beam by projecting the real 3D beam distribution onto the reference trajectory. The space charge (SC) interaction of the beam is negligible at 6 GeV energy. At the exit of the LPA the SC parameter (SC tune shift per unit length) is already $\delta Q_{\mathrm{SC}} < 10^{-6}\ \mathrm{m}^{-1}$ and rapidly decreases as the beam expands into free space. Thus, SC is not expected to play a significant role, after the beam exits the plasma cell.

Beam capture: Both permanent and electromagnetic (EM) quadrupoles have been considered for beam capture. In our design we have chosen a triplet of conventional high-field EM quadrupoles, which are now becoming readily available thanks to their usage in advanced 4th generation light sources, such as ESRF-EBS or PETRA IV. With conventional EM quadrupoles the full beam radius does not exceed 2 mm in the capture triplet (Fig. 20). This is well within the physical aperture and the expected good field region of high-field capture quadrupoles. For comparison, ESRF-EBS quadrupoles have a good field region radius of 7 mm where the relative deviation of the focusing gradient $\Delta G/G < 10^{-3}$ [109]. This justifies our idealized lattice model. A more thorough analysis of the capture process including multipole errors and misalignment can be done at the technical design stage.

Strong focusing inside the plasma cell together with a large energy spread might lead to a considerable chromatic emittance growth in the capture triplet. To highlight this issue its impact has been simulated for three non-baseline early estimate beam distributions of different initial transverse emittance and divergence. The distributions were modeled as Gaussian beams with the relative energy spread being a free parameter. Figure 21 shows the resulting relative increase of the transverse emittance in the capture triplet. As expected from Eq. (B.11), it is quadratic with relative energy spread and $\hat{\gamma}_x$. Therefore, in order to keep the chromatic emittance growth under control, the LPA must be optimized to provide small energy spread and small divergence beams. The former can be achieved by meeting the average beam-loading conditions to minimize the energy chirp of the beam. For the latter, appropriate plasma exit downramps shall be deployed to minimize the divergence of the beam at the exit of the plasma cell (see App. B.7).

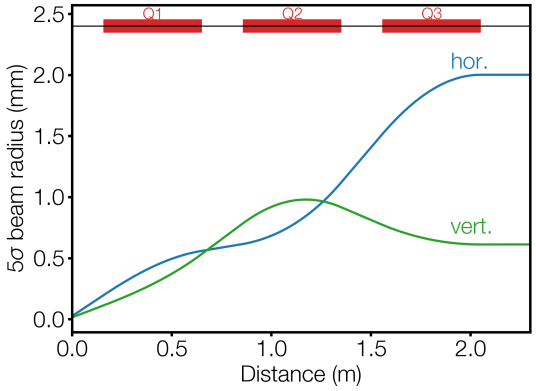

Figure 20. Evolution of the transverse beam size in the capture triplet. 5 rms beam radii are plotted together with locations of triplet quadrupoles Q1–3. The transverse size remains relatively small during the capture process allowing using conventional electromagnetic quadrupoles.

Chromatic correction: The chromaticity in the capture triplet can significantly degrade the beam emittance (Fig. 21). To keep the emittance growth under control one has to ensure both small energy spread and small beam divergence. On top of that, several chromatic correction options have been considered. The overall chromatic correction strategy is to minimize the increase of the larger horizontal emittance, while limiting the increase of the vertical emittance and keeping the footprint of the chromatic corrector compact. Two designs were studied:

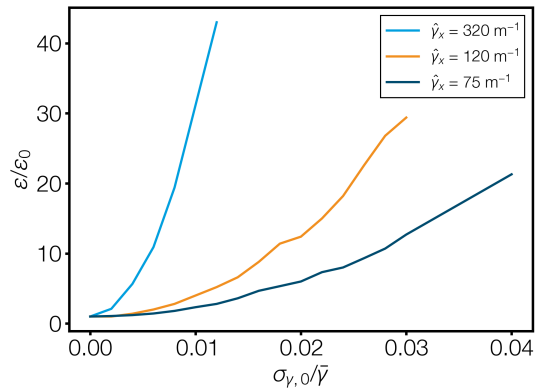

Figure 21. Chromatic emittance increase as a function of relative energy spread for different initial Twiss $\hat{\gamma}_x$ beam parameters. Twiss $\hat{\gamma}_x$ is related to beam divergence as $\sigma'_x = \sqrt{\epsilon_x \hat{\gamma}_x}$ (for more detail see Sec. B.7). The orange line corresponds to $\hat{\gamma}_x$ of the simulated baseline LPA beam (Fig. 4).

a C-chicane and an S-chicane (Table 9). The optimized designs for our beam parameters are shown in Fig. 22(a, b). The S-chicane, while slightly larger, offers a cancellation of nonlinear aberrations to a higher order.

Numerical tracking with semi-realistic electron beam distribution has demonstrated that the S-chicane has overall a larger tolerance to higher energy spread from the LPA [Fig. 22(c, d)]. In this study only the energy spread of the beam was varied by adjusting the energy deviations of individual macroparticles, while keeping the rest of the beam parameters, such as emittance or bunch length, fixed.

Option	C-chicane	S-chicane
R_{56}	5 mm	5 mm
Bending angle	2.7 deg	2.0 deg
Max dispersion	6 cm	4 cm
Max sext. field	670 T/m^2	550 T/m^2
Total length	6 m	8.5 m

Table 9. Summary of chromatic correction options

CSR suppression: An important physical effect that might change the quality of the electron beam is CSR. Its characteristic scale, the energy change per unit length, can be estimated as [110]:

$$W_{\mathrm{CSR}} = mc^2 N_b r_e \left(\frac{\kappa}{\sigma_z^2}\right)^{2/3}, \qquad \text{(A.3)}$$

with N_b the number of electrons in the bunch, r_e the classical electron radius, κ the curvature of the bending field and σ_z the

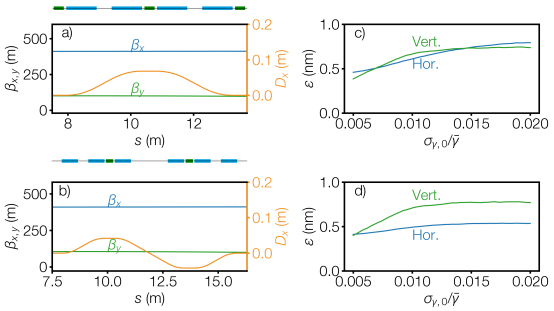

Figure 22. Layout and optics functions (a, b) and final rms physical emittances (c, d) for an S-chicane and more compact C-chicane vs the initial rms relative energy spread. The S-chicane offers a better correction of the chromatic emittance increase in the horizontal plane. CSR effects included in the simulation.

bunch length. For an un-stretched bunch, Eq. (A.3) predicts a non-negligible CSR wakefield of ~3 MV/m in the strong dipoles of the main chicane. For a dipole length of 175 cm, the CSR wakefield would induce an energy kick of ~5 MeV in the tail of the un-stretched bunch. Although the magnitude of the energy variation induced by CSR is at the permille level, it could have a sizeable effect in the energy spread of the bunch after energy compression. In addition, CSR could have an additional impact on the beam's emittance, not accounted for directly by Eq. (A.3).

Parameter	Chicane		
	Chromatic	Main	
Bending angle / deg	2.0	7.25	
Bending field / T	1.0	1.45	
Dipole length / cm	70	175	
		direct	*prestr.*
Bunch length / µm	3.2	3.2	30
CSR wake / MV/m	2.1	2.7	0.14
CSR kick / MeV	1.5	4.7	0.2

Table 10. Steady-state CSR-kick estimate in the first dipole of the main and chromatic chicanes, respectively. For the main chicane two cases are shown: with and without a previous bunch stretching in the chromatic chicane.

Nevertheless, by lengthening the bunch before it reaches the first strong dipole of the main chicane, the chromatic chicane allows for a significant mitigation of the CSR effect. Since the chromatic chicane does not need a large R_{56}, it is made of relatively weak dipoles, with a smaller κ and shorter in length (Tab. 10). Thus, the integrated CSR kick after the first dipole of the chromatic chicane is just ~1.5 MeV, a 70% smaller than that calculated for the main chicane. With an R_{56} = 5 mm, the chro-

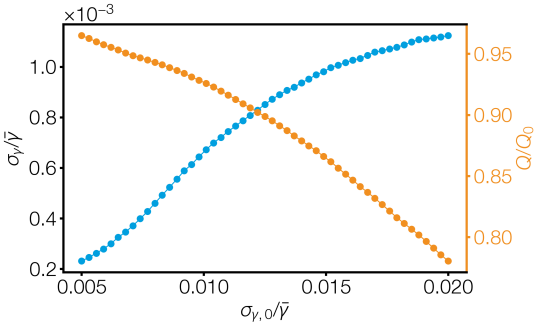

Figure 23. The final energy spread increases and the charge transmission decreases with the initial energy spread. No variation of the initial beam energy is assumed.

matic chicane stretches the bunch longitudinally by a factor 10 (from $\sim$ 3 to $\sim$ 30 μm), rendering negligible the CSR effects in the main chicane: a factor $10^{4/3}$ smaller after pre-stretching in the chromatic chicane.

Tolerance to energy spread: With the chromatic correction and CSR suppression in place the beamline features a relatively large tolerance to the initial energy spread from the plasma cell. In order to test the limits of acceptable energy spread we performed a numerical study artificially scaling the energy spread in a realistic LPA beam, while keeping all the other parameters constant. The results show an acceptable permille-level final energy spread and beam transmission of ~80%, for up to 2% relative energy spread in the initial LPA beam (Fig. 23).

B. Laser-plasma accelerators

B.1. Overview of experiments

In 1979, Tajima and Dawson first proposed the idea of using a laser pulse to accelerate electrons in a plasma medium. In their seminal paper [5], they showed that an intense electromagnetic pulse can create a wake of plasma oscillations through the action of the ponderomotive force. Laser pulses with a central wavelength of about 1 μm and peak intensities above 10^{18} W/cm^2 could be used to generate large electric amplitude wakes of ∼30 (100) GV/m in plasmas of 10^{17} (10^{18}) cm^{-3} density, suitable for the acceleration of electron bunches up to 10 (1) GeV energy over 30 cm (1 cm) distance. This new type of laser-plasma accelerator (LPA) outperforms the accelerating gradient of RF-based technology by several orders of magnitude, thus opening the possibility for accelerator facilities with a much-reduced size and cost.

LPAs were proposed over 40 years ago, but it was only after the invention of chirped pulse amplification (CPA) [111] and the rapid progress in high-power laser technology, that relevant experimentation with LPAs could prosper. In particular, the use of modern titanium-doped sapphire (Ti:Sa) lasers with ∼800 nm wavelength, short pulse durations of ∼30 fs and moderate energy around 1 J, led to a series of milestone experiments during the early 2000's, demonstrating extreme accelerating gradients of $\gtrsim$ 100 GV/m, and the production of electron bunches with ∼100 MeV energies [112] and few-percent energy spread [9–11]. In the subsequent years, the development of plasma targets embedded in gas-filled capillaries enabled, on the one hand, laser guiding capabilities through a capillary discharge waveguide for the generation of GeV-class electron beams [6]; and on the other hand, largely improved stability of the produced electron bunch parameters [113]. Besides, improved control over the electron bunch injection event was attained through newly designed techniques [114–120], and beam emittances comparable or superior to state-of-the-art RF accelerators were demonstrated [12–15].

During the next decade (2010's), new LPA experiments powered by higher-power laser systems (subpetawatt class) with pulse energies in the tens of joules range demonstrated up to 2 GeV energy gain in the self-guided regime [121, 122], and 4.2 GeV by deploying capillary discharge waveguides [7]. The current energy gain record of 7.8 GeV was demonstrated later on by increasing the focusing strength of the waveguide using a capillary discharge in conjunction with a laser heater [8]. Few years ago, a new technique using hydrodynamic optical-field-ionized (HOFI) plasma channels for guiding high-power lasers was proposed and demonstrated [26, 27, 58, 59]. First experimental results for LPAs using HOFI channels were published in 2022, demonstrating electron beams at 1.1 GeV using 1.7 J laser pulses [60] and up to 5 GeV with 11 J [61].

Despite these major advances, a number of challenges still remain which prevent the use of LPAs as a viable alternative to RF technology. One of the current most pressing issues is achieving beams with sub-percent energy spread, as required by applications such as free-electron lasers (FELs) or storage rings. Recently, free-electron lasing by an LPA beam has been demonstrated in a landmark experiment [22], by virtue of its excellent beam quality: average energy 490 MeV with a spread of 0.5% and an average integrated charge of around 30 pC. Equally crucial for applications are the shot-to-shot stability of the LPA beams, the reproducibility of the results and the capability for continuous operation. Recent LPA experiments at LUX (DESY) have shown enormous progress towards enhanced beam quality and practical functionality; demonstrating 1% energy spread at ∼300 MeV [17] and a continuous energy stability of 1.8% for about 29 consecutive hours [16].

Experiment	Laser		Plasma	Electron bunch		
	Energy (J)	Duration (fs)	Density (10^{18} cm^{-3})	Energy (MeV)	Spread (%)	Charge (pC)
Mangles (2004) [9]	0.50	40	20	70	3	22
Geddes (2004) [10]	0.50	55	45	86	2	320
Faure (2006) [11]	0.72	30	7.5	125	9	25
Leemans (2006) [6]	1.5	38	4.3	1000	2.5	30
Osterhoff (2008) [113]	0.85	42	7.3	200	6	32
Kneip (2009) [123]	10	55	5.5	800	10	250
Wang (2013) [122]	100	160	0.48	2000	6	63
Leemans (2014) [7]	16	40	0.70	4200	6	6
Couperus (2017) [83]	2.5	30	4.40	310	6	300
Gonsalves (2019) [8]	31	35	0.27	7800	10	5
Gonsalves (2019) [8]	31	35	0.34	6000	10	62
Wang (2021) [22]	2.0	25	2.0	490	0.5	30
Kirchen (2021) [17]	2.5	33	1.0	282	1.2	44
Oubrerie (2022) [60]	1.7	30	1.4	980	2	12
Miao (2022) [61]	11	45	0.16	5000	15	10
Grafenst. (2023) [124]	6	30	1.0	1000	10	92

Table 11. Summary of LPA experiments.

B.2. Working principle

In a LPA a high-intensity laser pulse excites wakefields in a plasma by means of its ponderomotive force [62, 63],

$$\mathbf{F}_p = -mc^2 \frac{\nabla a^2}{2\gamma}, \tag{B.1}$$

where $a = eA/mc^2$ is the normalized amplitude of the vector potential of the laser[1], $\gamma = \sqrt{1 + (\mathbf{p}/mc)^2 + a^2}$ is the relativistic factor of a plasma electron with momentum $\mathbf{p}$ and rest mass m, e is the elementary charge and c is the speed of light in vacuum. The intensity of the laser pulse is related with a by $I = (P_A/8\pi)\, k_0^2 a^2$, with $k_0 = 2\pi/\lambda_0$ the laser wavenumber and λ_0 the laser wavelength. $P_A = I_A(mc^2/e) \simeq 8.7$ GW is a constant with units of power and $I_A = 4\pi\epsilon_0 mc^3/e \simeq 17$ kA is the Alfvèn current, with ϵ_0 the vacuum permittivity. The ponderomotive force can be viewed as radiation pressure (i.e., the gradient of the electromagnetic energy density, $\mathbf{F}_p \propto -\nabla I$). Hence, the laser pushes away the plasma electrons from its high-intensity center as it propagates through the plasma with a group velocity given by $v_g = c\sqrt{1 - (k_p/k_0)^2}$, where $k_p = \sqrt{n_p e^2/m\epsilon_0 c^2}$ is the plasma wavenumber associated to n_p, the density of the unperturbed plasma.

As the laser passes, the pushed electrons are attracted back by the space-charge field of the plasma-ion background[2], generating in this way a trailing plasma wake of electrons (see Fig. 24) with highly intense associated wakefields. These wakefields propagate at the velocity of the drive laser and oscillate at the plasma frequency, $\omega_p = k_p c$.

Gaussian beam: The laser envelope is usually modeled as a Gaussian beam

$$a = a_0 \left(\frac{w_0}{w}\right) \exp\left(-\frac{r^2}{w^2} - \frac{\zeta^2}{c^2\tau^2}\right), \tag{B.2}$$

where $\zeta = z - ct$ is the (speed-of-light) comoving variable. $w = w(z)$ is commonly used as the definition of the laser spot size, with w_0 its value at focus (waist). In vacuum, the laser spot size evolves as $w(z) = w_0\sqrt{1 + (z/z_R)^2}$, with $z_R = \pi w_0^2/\lambda_0$ known as the Rayleigh length — the distance from the beam waist at which the laser intensity halves. τ refers to the laser pulse duration and equals to two times the rms pulse length of the intensity[3]. The peak power of the laser beam is given by $P_0 = (\pi/2)\, I_0 w_0^2 = (P_A/16)\, (k_0 w_0)^2\, a_0^2$ and the total energy contained in the pulse by $\mathcal{E}_l = (\sqrt{2\pi}/2)\, P_0 \tau$.

[1] The vector potential of a linearly polarized laser propagating in the z direction can be decomposed into a fast phase and a slow envelope according to $\mathbf{A} = A\, \cos(kz - \omega t)\, \hat{\mathbf{x}}$

[2] The ions, being much more massive than the electrons, can be considered immobile during the time scale of the plasma oscillation period

[3] The FWHM of the intensity, $\tau_{\text{fwhm}} = \sqrt{2\ln 2}\,\tau \approx 1.12\,\tau$, is used more frequently as the pulse duration.

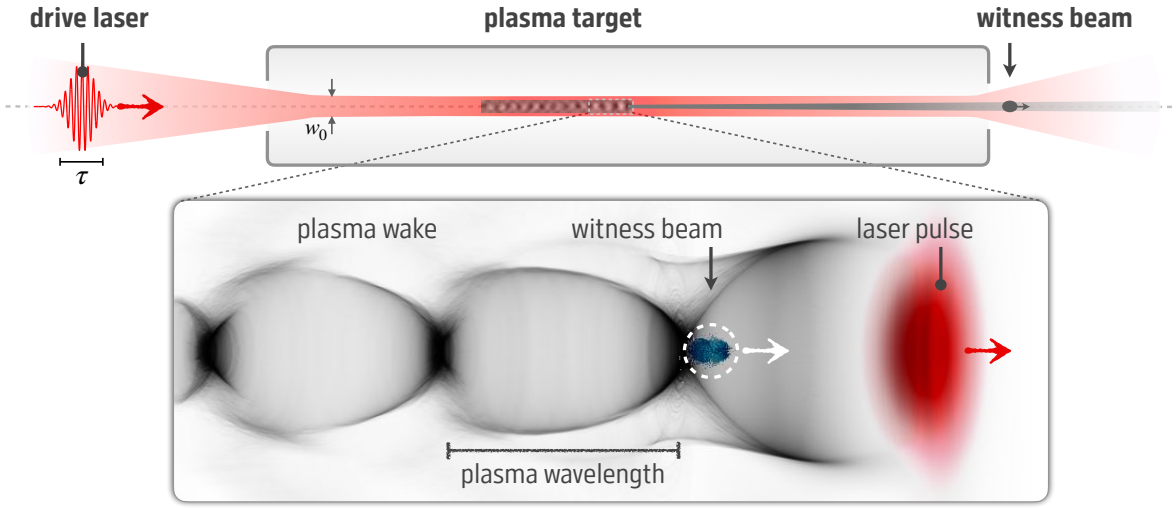

Figure 24. Schematics of a generic LPA. A laser is strongly focused into a plasma target to excite a strong electromagnetic wake for the acceleration electron beams to GeV energies within cm-scale distances.

B.3. The blowout regime

Sufficiently intense lasers ($a_0^2 \gg 1$) excite the wakefields in the so-called *blowout* regime, completely expelling all plasma electrons from their propagation path, and forming a clear ion cavity (or ion channel) surrounded by a sheath of plasma electrons (see Fig. 24). The length of this cavity is given approximately by $\lambda_p = 2\pi/k_p \simeq 33\,\mu\text{m}\; n_p(10^{18}\,\text{cm}^{-3})^{-1/2}$, while its width, commonly referred to as the blowout radius, R_b, is approximately defined by the radial extent of the laser, w_0. Inside this cavity accelerating fields exceeding the cold non-relativistic wave-breaking limit,

$$E_0 = (mc^2/e)\,k_p \simeq 96\,\text{GV/m}\sqrt{n_p[10^{18}\text{cm}^{-3}]}\,, \tag{B.3}$$

are generated, as well as an uniform focusing gradient $K = (mc/2e)\,k_p^2 \simeq 30\,\text{MT/m}\,n_p[10^{18}\text{cm}^{-3}]$, enabling ideal conditions for the acceleration and transport of electron beams [64–66] to GeV energies within cm-scale distances [125]. Operating in the blowout regime is therefore convenient for an efficient, emittance preserving, acceleration. Reaching $a_0^2 > 1$ with the commonly used Ti:Sa laser systems ($\lambda_0 = 800$ nm) requires peak intensities $I_0 > 2.1\times10^{18}\,\text{W/cm}^2$.

Resonant length: The wakefield is driven most efficiently when the laser pulse length, $c\tau$, is comparable but shorter than the plasma wavelength [63], i.e. $c\tau \lesssim \lambda_p$. For the Gaussian beam of Eq. (B.2), it was found that, for $a_0^2 \sim 1$, an optimal accelerating gradient [126, 127] is reached when $k_p c\tau = 2\sqrt{2}$.[4]

Matched radius: Full electron plasma cavitation by means of the laser ponderomotive force occurs when this becomes stronger than the attraction of the ion channel. Evaluating Eq. (B.1) for the Gaussian beam of Eq. (B.2) at the radial position $r = w_0$ and equaling to the electrostatic force of the ion channel $F_{\text{ion}}(r) = -(mc^2k_p^2/2)\,r$ at the same position, it is found that $k_p w_0 = 2\sqrt{a_0}$. It has been shown that this condition leads to the self-guided propagation of the laser beam, without significant variations of the pulse profile over the interaction distance [125]. Therefore, the laser spot size that satisfies this condition is usually refer to as the *matched radius*. In terms of the peak power, P_0, the matching condition can be written as $a_0 = 2(P_0/P_c)^{1/3}$ with

$$P_c \simeq 17.4\,\text{GW}\left(\frac{k_0}{k_p}\right)^2 \simeq \frac{30\,\text{TW}}{n_p[10^{18}\text{cm}^{-3}]}\,, \tag{B.4}$$

the critical power for relativistic self-focusing[5] [128, 129].

[4] Maximizing the accelerating amplitude for a fixed a_0, in the linear regime, yields $k_p c\tau = 2$, which is perhaps more often quoted as the resonant length.

[5] Self-focusing occurs as a result of an increase of the wave refractive index arising from two effects: the mass increase of electrons caused by their relativistic quiver velocity in the light wave, and the reduction of the electron density as a result of ponderomotive force expulsion of the electrons.

Wakefields: Inside the blown-out region, free of plasma electrons, a constant focusing strength is generated by the uniform background of ions [64], such that $W_r \equiv E_r - cB_\phi = cKr$ for all ζ. Therefore, by virtue of the Panofsky-Wenzel theorem [130], inside the cavity, the longitudinal electric field is uniform along the radius, i.e. $= \partial_r E_z = \partial_\zeta W_r = 0$. The calculation of E_z as a function of ζ inside the cavity is non trivial as it directly depends on the dynamics of the plasma electron current, j_p, in the plasma sheath [65]: $E_z = -\int_0^\infty (j_{p,r}/c\epsilon_0)\,\mathrm{d}r$. Several models to calculate E_z in the blowout exist in literature [65, 66, 131, 132]. It was shown in [133] that for sufficently intense laser drivers ($a_0 \gtrsim 4$) at approximately the matched radius, the sheath of plasma electrons approximates a sphere around its center and $E_z \simeq (E_0/2)\, k_p(\zeta - \zeta_c)$, with ζ_c the longitudinal position of the cavity center. Evaluating E_z at one blowout radius upstream the cavity center and using the matching condition $k_p R_b = k_p w_0 = 2\sqrt{a_0}$, one gets the following estimation for the maximum accelerating field that is reached at the back of the cavity

$$E_{z,\max} \simeq -E_0\sqrt{a_0}\,. \tag{B.5}$$

Electron trapping: In the blowout regime, the plasma electrons acquire relativistic velocities. In particular, they feature highest longitudinal momentum after the first oscillation, where the plasma electron sheath closes at the end of the ion cavity. When these electrons become faster than the wake, they can be *trapped* into the cavity forming a *witness* beam that can be further accelerated to high energies. This process is referred to as *wave-breaking* [134, 135] and it has been the mechanism behind the production of first high energy electron beams from LPAs [9–11, 112]. However, relying on wave-breaking to control the properties of the witness beam is cumbersome and more refined techniques to control the injection of witness beam have been developed with the years. Among these techniques, we highlight density downramp injection, which confines wave-breaking to a sharp, localized, downward density transition [115, 118, 119, 136]; and ionization injection, where injection is triggered by ionization of deeper electronic levels contained in a dopant species [83, 116, 117].

Beam loading: The space-charge field of the witness beam acts on the plasma electron current thus modifying E_z. This effect is known as *beam loading*. In principle, it is possible to find a certain current profile for the witness beam that flattens E_z along its length. This optimal beam loading leads to an uniform acceleration of the witness beam and therefore to a virtually zero correlated energy spread. For the strong blowout regime described in [66], such optimally beam loading profile was calculated [137] to be trapezoidal with the peak current (at the front) given by $I_{b,\max} = (I_A/2)\sqrt{(E_{z,b}/E_0)^4 + (k_p R_b/2)^4}$, with $E_{z,b}$ the accelerating field at the front of the witness beam. The total charge in the witness bunch, Q_b, which optimally loads the wakefield in this regime satisfies the following relation [137]

$$Q_b E_{z,b} = \frac{I_A mc}{e}\,\frac{(k_p R_b)^4}{64}\,. \tag{B.6}$$

Using Eq. (B.5) for $E_{z,b}$ and matching conditions for the laser spot size in Eq. (B.6), we get the following expression for the beam-loading charge: $Q_b = I_A a_0^{3/2}/2ck_p \propto a_0^{3/2} n_p^{-1/2}$.

B.4. Acceleration length

The energy gain of the witness beam is limited by the distance at which the conditions for the acceleration can be maintained.

Diffraction: Primarily, the acceleration distance is limited by the natural diffraction of the laser. Although the relativistic self-focusing effect can help to extend the acceleration for a few Rayleigh lengths, it is ineffective for short pulses [62] [6], such as those needed to resonantly driver a wake. The acceleration process in this case will be still limited by diffraction to a characteristic length given by: $L_{\mathrm{diff}} \approx 2z_R = w_0^2 k_0$. To maintain the acceleration far beyond the diffraction length, external guiding channels shall be deployed (see Sec. B.6). However, the eventual energy gain of electrons by the wakefield is limited either by depletion or by dephasing of the driving laser pulse.

[6] The diffraction of the frontal edge weakens the strength of the waveguide.

Depletion: The energy gain is ultimately limited by the distance at which the drive laser (the pump) can still transfer energy to the electron beam through the plasma in an effective way. As the laser drives the wakefield, local pump depletion occurs at the front of the pulse and the laser evolves to have a sharp rising edge, which *etches* back through the pulse [77, 138, 139], causing pulse length compression and power amplification [77]. After the pulse reaches a minimum length, it rapidly lengthens, losing resonance with the plasma [139]. At this point, the conditions for the acceleration of the witness beam are terminated[7]. An estimation of the depletion length can be obtained by considering the etching velocity of the laser pulse [138], $v_{\rm etch} \simeq c(k_p/k_0)^2$, and the distance needed for the pulse to etch over its length [125], $L_{\rm depl} \approx c\tau\,(k_0/k_p)^2$.

Dephasing: Dephasing occurs when the highly relativistic witness beam (moving at $\sim c$) outruns the accelerating region of the plasma wake. It is is usually said that the plasma wake moves at the group velocity of the drive laser, $v_g = c\sqrt{1-(k_p/k_0)^2}$. However, because of pulse front etching, the effective laser pulse velocity is reduced, such that the plasma wave phase velocity becomes $v_\phi = v_g - v_{\rm etch} \simeq c\,(1-(3/2)(k_p/k_0)^2)$. Thus the dephasing length becomes $L_{\rm deph} \approx (2/3)(k_0/k_p)^2 R_b$.

B.5. Energy gain

The energy gain of the witness beam is given by $\Delta W = -e\bar{E}_{z,b}L_{\rm acc}$, where $\bar{E}_{z,b}$ is the accelerating field on the witness beam averaged over the acceleration distance, $L_{\rm acc}$. The following equations are estimations for the energy gain when the acceleration is limited by diffraction, depletion and dephasing, respectively

$$\Delta W_{\rm diff} \approx mc^2\sqrt{a_0}\,(k_p w_0)^2\,(k_0/k_p)\,. \quad \text{(B.7a)}$$

$$\Delta W_{\rm depl} \approx mc^2\,(\sqrt{a_0}/2)\,(k_p c\tau)\,(k_0/k_p)^2\,. \quad \text{(B.7b)}$$

$$\Delta W_{\rm deph} \approx mc^2\,(\sqrt{a_0}/3)\,(k_p R_b)\,(k_0/k_p)^2\,. \quad \text{(B.7c)}$$

We shall note that $\bar{E}_{z,b} \simeq -E_0\sqrt{a_0}$ is used in Eq. (B.7a), as no significant dephasing happens by the diffraction length[8]. By contrast, the depletion length is comparable to the dephasing length and we use $\bar{E}_{z,b} \simeq -E_0\sqrt{a_0}/2$ in Eqs. (B.7b)–(B.7c).

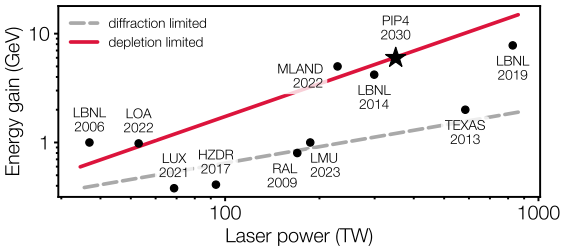

Figure 25. Basic scaling of the electron energy gain with the laser peak power in the diffraction limited (dashed line) and the depletion limited (crimson line) regimes. The operating plasma density scales inversely proportional to the laser power. Results from key experiments are shown as dots for a reference. The star indicates the base design power of PIP4.

Basic scalings: The Eqs. (B.7) are useful to estimate the energy gain achievable by an LPA driven by a laser pulse characterized by its peak intensity, a_0, and normalized sizes, $k_p w_0$ and $k_p c\tau$, at focus. Fixing these parameters and scaling the plasma density, we have that the peak power of the laser goes as $P_0 \propto a_0^2 w_0^2 \propto n_p^{-1}$ and its energy as $\mathcal{E}_l \propto a_0^2 w_0^2 c\tau \propto n_p^{-3/2}$. The energy gain scales as $\Delta W \propto n_p^{-1}$, when the acceleration length is limited by depletion. The energy gain relative to the initial laser energy goes as $\Delta W/\mathcal{E}_l \propto n_p^{1/2}$, while the witness beam charge that can be accelerated at optimal beam loading conditions scales as $Q_b \propto n_p^{-1/2}$ (from Eq. (B.6)). This means that the total energy transfer balance (efficiency), $Q_b\Delta W/\mathcal{E}_l$, does not change with the plasma density.

Ballpark estimates for PIP4: We use these basic scalings to estimate the leading param-

[7] Numerical solutions indicate that significant depletion ($\sim$ 50%) is possible for $a_0 \sim$ 1–2 before pulse lengthening causes loss of resonance with the plasma, a reduction in the plasma wave amplitude and a complete detuning with the witness beam [139]

[8] The diffraction length is much smaller than the dephasing length for the parameters of interest

eters of the LPA that will be needed to produce 6 GeV beams for PIP4: Imposing matching conditions for the laser driver at focus ($k_p c\tau = 2$ and $k_p w_0 = 2\sqrt{a_0}$), a moderately high peak intensity of $I_0 = 1\times10^{19}$ W/cm^2 ($a_0 = 2.2$), and a plasma density of $n_p = 2\times10^{17}$ cm^{-3}, Eq. (B.7b) can be used to estimate an energy gain of 6.5 GeV. With these parameters, the energy content of the laser pulse would be 20 J and its peak power 202 TW. The total acceleration length is limited by dephasing in this case to 20 cm. The charge of an optimally loaded witness beam can be estimated[9] using Eq. (B.6) to ~500 pC, which would result in an energy transfer efficiency of 16%.

Another example of interest that we use for reference (see Sec. A.1) results from rescaling the laser parameters of the LUX experiment in [17] to a plasma density of $n_p = 2\times10^{17}$ cm^{-3}, i.e., 5 times smaller than the original. With $a_0 = 2.0$, $w_0 = 50$ μm and $\tau = 63$ fs, the laser pulse energy is 27.5 J and the peak power 345 TW. In this case, the acceleration distance is limited by laser depletion to 19.5 cm. The energy gain given by Eq. (B.7b) is 6.0 GeV. Figure 25 shows the scaling of the energy gain with the peak power of the laser (inversely proportional to the plasma density), taking this case as reference, and using Eqs. (B.7a) and (B.7b) for a diffraction and depletion limited scenario, respectively.

B.6. Laser guiding channels

In order to extend the acceleration up to the depletion length, the laser must remain tightly focused and intense over distances far exceeding the Rayleigh length. External guiding is the preferred method of extending the acceleration length owing to its ability to produce multi-GeV energy gains from LPAs driven by sub-petawatts class lasers with pulse energies in the 10–20 J range (see Fig. 25).

A parabolic plasma density profile of the type $n_p(r) = n_{p,0} + \Delta n\,(r/w_m)^2$ is shown to optimally guide Gaussian beams [140] (in the low intensity limit) when $w_0 = w_m$ and $\Delta n = \Delta n_c \equiv 1/\pi r_e w_m^2$, with r_e the classical electron radius. When this condition is fulfilled

[9]This expression for the beam-loaded charge is obtained for the strong blowout regime ($a_0 \gg 1$) and it is known to overestimate the charge amount for milder regimes ($a_0 \lesssim 2$).

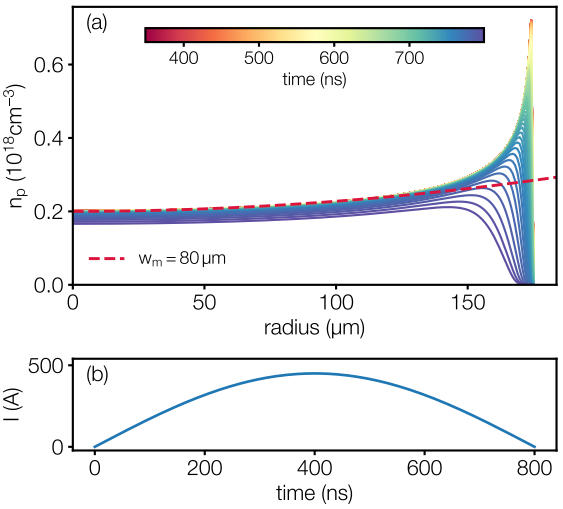

Figure 26. Simulated evolution of the plasma density profile generated in a hydrogen-filled capillary of radius $R_0 = 175$ μm by an electric discharge. (a) The plasma density profile as a function of time (colored lines) calculated using the QUEST model [142]. The ideal parabolic profile with $n_{p,0} = 2\times10^{17}$ cm^{-3} and $w_m = 80$ μm is also shown (dashed line) for reference. (b) Electric discharge current.

the laser propagates at waist with no transverse oscillations of the envelope: the laser beam is said to be matched to the guiding channel. When the laser is not matched, its spot size oscillates between $w = w_0$ and $w = \sqrt{\Delta n_c/\Delta n}\,(w_m^2/w_0)$ with a period given by $\lambda_{osc} = \pi z_R\sqrt{\Delta n_c/\Delta n}$ [141].

There are several methods of guiding high-intensity laser pulses, although two guiding techniques stand out for their suitability to multi-GeV electron acceleration and have experimentally demonstrated the generation of such beams. Capillary discharge waveguides were the basis of the first multi-GeV gain LPA experiments at LBNL [6–8]. Hydrodynamic optical-field-ionized (HOFI) waveguides have been developed more recently for LPAs [26, 27] and first experiments demonstrating multi-GeV acceleration have been published [60, 61].

B.6.1. Capillary discharge waveguides

In this method, an electric current of few hundred amperes discharges over a gas-filled capillary (typically with hydrogen), inducing ionization and Ohmic heating of the plasma, and thus generating a radial temperature gradient between the on-axis plasma and the cooler capillary walls. In quasistatic equilibrium, the balance between Ohmic heating and bound-

ary heat loss results in distinctive temperature and electron density profiles, which can be exploited for guiding high intensity laser pulses [143]. Near the capillary axis, the electron density profile approximates a parabolic shape parameterized by its on-axis value, $n_{p,0}$, and curvature, $n''_{p,0}$. The focusing strength of the waveguide is characterized by the matched spot size, w_m, which relates to the curvature by $w_m = (2/\pi r_e n''_{p,0})^{1/4}$. A useful approximate expression for w_m in the steady state equilibrium of the plasma after the discharge is given in [143] as

$$w_m[\mu m] \approx 1.48 \times 10^5 \frac{\sqrt{R_0[\mu m]}}{(n_{p,0}[cm^{-3}])^{1/4}}. \quad (B.8)$$

This equation stress the importance of the capillary radius, R_0, to achieve a small w_m suitable for the guiding of high-intensity laser pulses. As an example of interest, for $n_{p,0} = 2 \times 10^{17}$ cm^{-3} and $R_0 = 130$ µm, we get $w_m = 80$ µm from Eq. (B.8). Due to the proximity of the match spot size to the capillary radius, this configuration is susceptible of causing laser damage in the capillary [7]. Recently, cryogenically formed discharge waveguides have been proposed as a way to adjust the capillary radius *in situ*, alleviate the laser damage and increase the waveguide lifetime [144]. However, as it can be seen from Eq. (B.8), achieving yet smaller matched spot sizes for the plasma densities of interest would require capillaries smaller than the matched spot size. Figure 26 shows an example of the evolution of the plasma density radial profile inside a hydrogen discharge capillary, calculated using an accurate reduced model recently developed (QUEST) [142].

B.6.2. HOFI channels

This method utilizes an auxiliary low-energy laser to generate and heat a long and thin column of plasma by optical field ionization. This column expands hydrodynamically into the surrounding cold, unionized gas, driving a radial shock wave and forming a plasma channel along the axis of the plasma column. Near the axis, the radial profile of the plasma channel has a quasi-parabolic shape suitable to guide the drive laser for plasma acceleration [26, 27]. Channels of this type are a promising solution

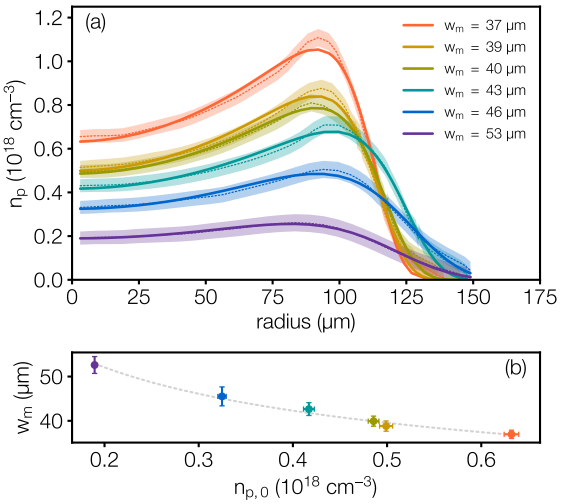

Figure 27. Measured plasma density profiles generated using the HOFI technique in [26]. (a) Electron density 3.9 ns after ionization for a range of different cell fill pressures (shaded dotted lines). Analytical fit to the measurements (solid lines). (b) Matched spot size versus on-axis electron density extracted from fits to the measurements.

for practical plasma accelerators capable of operation at high (multi-kilohertz) repetition rates, since the plasma channels are isolated from any physical structure which could be damaged by the driving laser pulse [26, 27]. Moreover, triggering the plasma channel formation by means of optical field ionization permits operation at relatively low axial plasma densities and so the generation of channels with a sufficiently low matched spot size.

Figure 27 (a) shows a series of HOFI plasma channels generated experimentally at University of Oxford [26] in hydrogen gas at different pressures. All profiles are measured 3.9 ns after ionization. By fitting the profiles near the axis to a parabolic function, the matched spot size, w_m, can be obtained as a function of the on-axis plasma density, $n_{p,0}$ (Fig. 27 (b)). For example, for $n_{p,0} \simeq 2 \times 10^{17}$ cm^{-3} waveguides with $w_m \simeq 50$ µm were generated [26].

Subsequent experiments with HOFI channels at Rutherford Appleton Laboratory [27] have demonstrated matched spot sizes of 40 µm for on-axis densities as low as 1.5×10^{17} cm^{-3}. Fits of the measured matched spot size as a function of the gas pressure revealed a $w_m \propto n_{p,0}^{-1/2}$ scaling. This scaling is ideal to keep the appropriate laser spot size, relative to the plasma wavelength, for a large range of plasma densities. Besides, it is also shown in [27] that, by adjust-

ing the initial gas pressure and the delay after the arrival of the channel-forming pulse, the matched spot size can be tuned.

B.7. Witness beam dynamics

The motion of a relativistic electron subject to the wakefields in the blowout cavity (see Sec. B.3) is ruled by the equations $\gamma' \simeq -(e/m)\,E_z$ and $x'' + (\gamma'/\gamma)\,x' + k_\beta^2\,x = 0$, which describe the transverse *betatron oscillations* of the electron with wavenumber

$$k_\beta = \sqrt{\frac{eK}{mc\gamma}} = \frac{k_p}{\sqrt{2\gamma}}\,. \tag{B.9}$$

Analytical solutions are known when k_β is a slowly varying function, i.e., $x = A_x\,(\gamma/\gamma_0)^{-1/4}\cos(\phi+\phi_0)$, with $\phi = \int_0^z k_\beta(z')\,\mathrm{d}z'$, the phase advance. The amplitude of the oscillation is given by $A_x = \sqrt{x_0^2 + (v_{x,0}/\omega_{\beta,0})^2}$, with x_0 and $v_{x,0}$ the initial transverse position and velocity of the electron, respectively.

The dynamics of an electron beam is usually characterized by the evolution of its statistical moments, which can be obtained from the one-particle solutions to the equations of motion [145]. Considering a mono-energetic slice of the beam, the centroid position, $\bar{x} \equiv \langle x\rangle$ (first beam moment), behaves analogously to a single particle, describing transverse betatron oscillations with frequency ω_β and an amplitude defined by its initial offset. The transverse size (rms) of the slice (second beam moment), $\sigma_x \equiv \sqrt{\langle x^2\rangle}$, obeys the so-called beam-envelope equation [145]

$$\sigma_x'' + \left(k_\beta^2 - \frac{1}{\hat{\beta}_x^2}\right)\sigma_x = 0\,, \tag{B.10}$$

with, $\hat{\beta}_x \equiv \sigma_x^2/\epsilon_x$, the *beta function* of the beam and $\epsilon_x \equiv \sqrt{\sigma_x^2\sigma_{x'}^2 - \sigma_{xx'}^2}$, its trace-space emittance. Provided that the focusing strength, $K = (mc/2e)\,k_p^2$, is constant in the blowout, the normalized emittance, $\epsilon_{n,x} \equiv \sqrt{\sigma_x^2\sigma_{p_x}^2 - \sigma_{xp_x}^2}/mc \simeq \gamma\epsilon_x$, of the mono-energetic slice is preserved through the acceleration process. In general, the solution to Eq. (B.10) describes the oscillation of the beam envelope with a spatial period equal to half the betatron wavelength. In phase-space, the motion is characterized by the (rigid) rotation of the beam distribution at the betatron frequency. Such rotation is usually described by the Courant-Snyder *phase-space ellipse* [146], parameterized by the quantities (usually referred to as *Twiss* parameters) $\hat{\alpha}_x \equiv \sigma_{xx'}/\epsilon_x$, $\hat{\beta}_x \equiv \sigma_x^2/\epsilon_x$ and $\hat{\gamma}_x \equiv \sigma_{x'}^2/\epsilon_x$, which satisfy the relation $\hat{\beta}_x\hat{\gamma}_x - \hat{\alpha}_x^2 = 1$ and $\hat{\beta}_x' = -2\hat{\alpha}_x$.

A real beam can be thought as a collection of different mono-energetic slices. Thus, because the betatron frequency $\omega_\beta = ck_\beta \propto \gamma^{-1/2}$ is energy-dependent, beams with a sizeable energy spread experience the detuning of different mono-energetic phase-space ellipses, resulting in a projected emittance growth [147]. However, for a matched beam such that, $\hat{\beta}_{x,0} = k_\beta^{-1} = \sqrt{2\gamma}\;k_p^{-1}$ and $\sigma_{x,0}' = 0$ (or $\hat{\alpha}_{x,0} = 0$), it can be seen from Eq. (B.10) that there are no oscillations of the envelope and the projected emittance growth is effectively suppressed, even for a finite energy spread. Besides, it has been shown that adiabatic changes of the betatron frequency will not alter the matching conditions[10] and thus not lead to emittance growth through the acceleration [147]. If the beam is not matched, however, the emittance will increase to a saturation value given by $\epsilon_{n,x}^{\mathrm{f}} = (\epsilon_{n,x}/2)\;((1+\hat{\alpha}_{x,0}^2)/k_\beta\hat{\beta}_{x,0} + k_\beta\hat{\beta}_{x,0})$, which is reached when the different mono-energetic slices completely detune (full decoherence or full phase mixing). This phase mixing process will eventually match the beam at $\hat{\beta}_x = 1/k_\beta = \sqrt{2\gamma}/k_p$ and $\hat{\alpha}_x = 0$ with the new saturated emittance value.

Chromatic emittance growth can also occur after acceleration, when the beam leaves the plasma. For a beam with finite relative energy spread, σ_γ, the normalized emittance is related to the trace-space emittance [148, 149] by $\epsilon_{n,x}^2 = \bar{\gamma}^2(\sigma_\gamma^2\sigma_x^2\sigma_{x'}^2 + \epsilon_x^2) = \bar{\gamma}^2\epsilon_x^2(\sigma_\gamma^2\hat{\beta}_x\hat{\gamma}_x + 1)$. Since in a free drift, $\hat{\beta}_x = \hat{\beta}_x^* + (z-z_0)^2/\hat{\beta}_x^*$ and $\hat{\gamma}_x = 1/\hat{\beta}_x^*$ with $\hat{\beta}_x^*$ the value of the beta-function at waist[11], we have for the relative

[10] This means that the beam envelope evolves as $\sigma_x = \sqrt{\epsilon_{n,x}/\gamma\,k_\beta} \propto \gamma^{-1/4}$.

[11] Note that $\hat{\beta}_x^* = \epsilon_x/\sigma_{x'}^2$, inversely proportional to the beam divergence squared.

normalized emittance growth

$$\frac{\epsilon_{n,x}^{\mathrm{f}}}{\epsilon_{n,x}} = \sqrt{1+\sigma_\gamma^2\left(1+\frac{L^2}{\hat{\beta}_x^{*2}}\right)} \approx 1+\frac{1}{2}\sigma_\gamma^2\frac{L^2}{\hat{\beta}_x^{*2}}\,, \tag{B.11}$$

with L the free drift distance. The approximation holds for $\sigma_\gamma L/\beta_x^* \ll 1$; it remains valid for all practical cases where $L < 1$ m, considering $\sigma_\gamma \simeq 10^{-2}$ and $\beta_x^* \simeq 1$ cm. Assuming that the beam is matched to the local density when it leaves the plasma, we can take $\hat{\beta}_x^* = 1/k_\beta = \sqrt{2\gamma}/k_p \propto \sqrt{\gamma/n_p}$ in Eq. (B.11) to estimate the emittance growth. Clearly, increasing $\hat{\beta}_x^*$ at the exit of the plasma is key to mitigate the chromatic emittance growth in beam transport sections that follow. Deploying properly tailored plasma-to-vacuum transitions (or plasma down-ramps) has been shown to be an effective method [73–75] to reduce $\hat{\beta}_x^*$ and the emittance growth. Another option is to install focusing elements that reduce the beam divergence as close as possible to the plasma exit. Such elements include compact permanent magnet quadrupoles [150, 151] and plasma lenses [152–154]. Finally, reducing the relative energy spread is crucial to minimize the chromatic emittance growth.

References

[1] C. G. Schroer et al., *PETRA IV: upgrade of PETRA III to the Ultimate 3D X-ray microscope. Conceptual Design Report* (Deutsches Elektronen-Synchrotron DESY, 2019),

[2] C. G. Schroer et al., "PETRA IV: the ultralow-emittance source project at DESY", Journal of Synchrotron Radiation **25**, 1277–1290 (2018),

[3] C. G. Schroer et al., "The synchrotron radiation source PETRA III and its future ultra-low-emittance upgrade PETRA IV", European Physical Journal Plus **137**, 1312 (2022),

[4] W. Leemans, Presentation at DESY Scientific Committee, May 19, 2019.

[5] T. Tajima and J. M. Dawson, "Laser Electron Accelerator", Physical Review Letters **43**, 267–270 (1979),

[6] W. P. Leemans et al., "GeV electron beams from a centimetre-scale accelerator", Nature Physics **2**, 696–699 (2006),

[7] W. P. Leemans et al., "Multi-GeV Electron Beams from Capillary-Discharge-Guided Subpetawatt Laser Pulses in the Self-Trapping Regime", Physical Review Letters **113**, 245002 (2014),

[8] A. J. Gonsalves et al., "Petawatt Laser Guiding and Electron Beam Acceleration to 8 GeV in a Laser-Heated Capillary Discharge Waveguide", Physical Review Letters **122**, 084801 (2019),

[9] S. P. D. Mangles et al., "Monoenergetic beams of relativistic electrons from intense laser–plasma interactions", Nature **431**, 535–538 (2004),

[10] C. G. R. Geddes et al., "High-quality electron beams from a laser wakefield accelerator using plasma-channel guiding", Nature **431**, 538–541 (2004),

[11] J. Faure et al., "A laser–plasma accelerator producing monoenergetic electron beams", Nature **431**, 541–544 (2004),

[12] S. Fritzler et al., "Emittance Measurements of a Laser-Wakefield-Accelerated Electron Beam", Physical Review Letters **92**, 165006 (2004),

[13] E. Brunetti et al., "Low Emittance, High Brilliance Relativistic Electron Beams from a Laser-Plasma Accelerator", Physical Review Letters **105**, 215007 (2010),

[14] R. Weingartner et al., "Ultralow emittance electron beams from a laser-wakefield accelerator", Physical Review Special Topics - Accelerators and Beams **15**, 111302 (2012),

[15] G. R. Plateau et al., "Low-Emittance Electron Bunches from a Laser-Plasma Accelerator Measured using Single-Shot X-Ray Spectroscopy", Physical Review Letters **109**, 064802 (2012),

[16] A. R. Maier et al., "Decoding Sources of Energy Variability in a Laser-Plasma Accelerator", Physical Review X **10**, 031039 (2020),

[17] M. Kirchen et al., "Optimal Beam Loading in a Laser-Plasma Accelerator", Physical Review Letters **126**, 174801 (2021),

[18] S. Jalas et al., "Bayesian Optimization of a Laser-Plasma Accelerator", Physical Review Letters **126**, 104801 (2021),

[19] F. Grüner et al., "Design considerations for table-top, laser-based VUV and X-ray free electron lasers", Applied Physics B **86**, 431–435 (2007),

[20] K. Nakajima, "Towards a table-top free-electron laser", Nature Physics **4**, 92–93 (2008),

[21] A. R. Maier et al., "Demonstration Scheme for a Laser-Plasma-Driven Free-Electron Laser", Physical Review X **2**, 031019 (2012),

[22] W. Wang et al., "Free-electron lasing at 27 nanometres based on a laser wakefield accelerator", Nature **595**, 516–520 (2021),

[23] M. Labat et al., "Seeded free-electron laser driven by a compact laser plasma accelerator", Nature Photonics **17**, 150–156 (2023),

[24] S. Hillenbrand et al., "Study of Laser Wakefield Accelerators as injectors for Synchrotron light sources", Nuclear Instruments and Methods in Physics Research Section A **740**, 153–157 (2014),

[25] S. A. Antipov et al., "Design of a prototype laser-plasma injector for an electron synchrotron", Physical Review Accelerators and Beams **24**, 111301 (2021),

[26] R. J. Shalloo et al., "Hydrodynamic optical-field-ionized plasma channels", Physical Review E **97**, 053203 (2018),

[27] R. J. Shalloo et al., "Low-density hydrodynamic optical-field-ionized plasma channels generated with an axicon lens", Physical Review Accelerators and Beams **22**, 41302 (2019),

[28] W. P. Leemans and A. R. Maier, "Kaldera", https://mls.desy.de/kaldera (2022),

[29] A. Ferran Pousa et al., "Energy Compression and Stabilization of Laser-Plasma Accelerators", Physical Review Letters **129**, 094801 (2022),

[30] P. Söding, "On the discovery of the gluon", The European Physical Journal H **35**, 3–28 (2010),

[31] G. A. Voss and B. H. Wiik, "The electron-proton collider hera", Annual Review of Nuclear and Particle Science **44**, 413–452 (1994),

[32] H. Franz et al., "Technical Report: PETRA III: DESY's New High Brilliance Third Generation Synchrotron Radiation Source", Synchrotron Radiation News **19**, 25–29 (2006).

[33] H. Yavaş et al., "Direct imaging of orbitals in quantum materials", Nature Physics **15**, 559–562 (2019),

[34] S. Grundmann et al., "Zeptosecond birth time delay in molecular photoionization", Science **370**, 339–341 (2020),

[35] S. Weber et al., "Evolution of hierarchically porous nickel alumina catalysts studied by x-ray ptychography", Advanced Science **9**, 2105432 (2022),

[36] F. Maurer et al., "Tracking the formation, fate and consequence for catalytic activity of pt single sites on ceo2", Nature Catalysis **3**, 824–833 (2020),

[37] J. Engström et al., "Core–shell nanoparticle interface and wetting properties", Advanced Functional Materials **30**, 1907720 (2020),

[38] C. J. Brett et al., “Water-induced structural rearrangements on the nanoscale in ultrathin nanocellulose films”, Macromolecules **52**, 4721–4728 (2019),

[39] M. Eckermann et al., “Three-dimensional virtual histology of the human hippocampus based on phase-contrast computed tomography”, Proceedings of the National Academy of Sciences **118**, e2113835118 (2021),

[40] S. Pazicky et al., “Structural role of essential light chains in the apicomplexan glideosome”, Communications Biology **3**, 568 (2020),

[41] S. Günther et al., “X-ray screening identifies active site and allosteric inhibitors of sars-cov-2 main protease”, Science **372**, 642–646 (2021),

[42] T. F. Custódio et al., “Selection, biophysical and structural analysis of synthetic nanobodies that effectively neutralize sars-cov-2”, Nature Communications **11**, 5588 (2020),

[43] D. Einfeld et al., “First multi-bend achromat lattice consideration”, Journal of synchrotron radiation **21**, 856–861 (2014).

[44] R. Coisson, “Effective Phase Space Widths Of Undulator Radiation”, Optical Engineering **27**, 273250 (1988),

[45] H. Wiedemann, “Synchrotron radiation”, in *Particle accelerator physics* (Springer Berlin Heidelberg, Berlin, Heidelberg, 2003), pp. 647–686,

[46] I. Agapov et al., “PETRA IV storage ring design”, Proceedings of IPAC2022, 1431–1434 (2022),

[47] I. Agapov et al., “The PETRA IV storage ring design based on multi-bend achromat optics”, Submitted for publication (2022).

[48] C. Bernardini et al., “Lifetime and beam size in a storage ring”, Physical Review Letters **10**, 407–409 (1963),

[49] H.-C. Chao et al., “Design considerations of a high intensity booster for PETRA IV”, Proceedings of IPAC2021, 1386–1389 (2021),

[50] M. A. Jebramcik et al., “Injection design options for the low-emittance PETRA IV storage ring”, Proceedings of IPAC2022, 2689–2692 (2022),

[51] W. Kook, priv. comm. 2022.

[52] R. Onken, priv. comm. 2022.

[53] H. Ehrlichmann, priv. comm. 2022.

[54] B. Zeitler, priv. comm. 2022.

[55] S. Sievers, priv. comm. 2023.

[56] R. J. Shalloo et al., “Automation and control of laser wakefield accelerators using Bayesian optimization”, Nature Communications **11**, 6355 (2020),

[57] S. Jalas et al., “Tuning curves for a laser-plasma accelerator”, Physical Review Accelerators and Beams **26**, 071302 (2023),

[58] A. Picksley et al., “Meter-scale conditioned hydrodynamic optical-field-ionized plasma channels”, Physical Review E **102**, 053201 (2020),

[59] B. Miao et al., “Optical Guiding in Meter-Scale Plasma Waveguides”, Physical Review Letters **125**, 074801 (2020),

[60] K. Oubrerie et al., “Controlled acceleration of GeV electron beams in an all-optical plasma waveguide”, Light: Science & Applications **11**, 180 (2022),

[61] B. Miao et al., “Multi-GeV Electron Bunches from an All-Optical Laser Wakefield Accelerator”, Physical Review X **12**, 031038 (2022),

[62] E. Esarey et al., “Overview of plasma-based accelerator concepts”, IEEE Transactions on Plasma Science **24**, 252–288 (1996),

[63] E. Esarey et al., “Physics of laser-driven plasma-based electron accelerators”, Reviews of Modern Physics **81**, 1229–1285 (2009),

[64] J. B. Rosenzweig et al., “Acceleration and focusing of electrons in two-dimensional nonlinear plasma wake fields”, Physical Review A **44**, R6189–R6192 (1991),

[65] K. V. Lotov, “Blowout regimes of plasma wakefield acceleration”, Physical Review E **69**, 046405 (2004),

[66] W. Lu et al., “Nonlinear Theory for Relativistic Plasma Wakefields in the Blowout Regime”, Physical Review Letters **96**, 165002 (2006),

[67] C. Benedetti et al., “INF&RNO Modeling of 10 GeV-Class Electron Beams from a Laser-Plasma Accelerator Driven by the BELLA Laser”, Proceedings of AAC2018, 1–5 (2018),

[68] C. N. Danson et al., “Petawatt and exawatt class lasers worldwide”, High Power Laser Science and Engineering **7**, e54 (2019),

[69] S. M. Mewes et al., “Demonstration of tunability of hofi waveguides via start-to-end simulations”, Physical Review Research **5**, 033112 (2023),

[70] R. Lehe et al., “A spectral, quasi-cylindrical and dispersion-free Particle-In-Cell algorithm”, Computer Physics Communications **203**, 66–82 (2016),

[71] A. Ferran Pousa et al., “Multitask optimization of laser-plasma accelerators using simulation codes with different fidelities”, Proceedings of IPAC2022, 1761–1764 (2022).

[72] A. Ferran Pousa et al., “Bayesian optimization of laser-plasma accelerators assisted by reduced physical models”, Physical Review Accelerators and Beams **26**, 084601 (2023),

[73] K. Floettmann, “Adiabatic matching section for plasma accelerated beams”, Physical Review Special Topics - Accelerators and Beams **17**, 054402 (2014),

[74] I. Dornmair et al., “Emittance conservation by tailored focusing profiles in a plasma accelerator”, Physical Review Special Topics - Accelerators and Beams **18**, 041302 (2015),

[75] X. L. Xu et al., “Physics of Phase Space Matching for Staging Plasma and Traditional Accelerator Components Using Longitudinally Tailored Plasma Profiles”, Physical Review Letters **116**, 124801 (2016),

[76] M. Santarsiero et al., “Focusing of axially symmetric flattened Gaussian beams”, Journal of Modern Optics **44**, 633–650 (1997),

[77] M. J. V. Streeter et al., “Observation of Laser Power Amplification in a Self-Injecting Laser Wakefield Accelerator”, Physical Review Letters **120**, 254801 (2018),

[78] G. D’Auria et al., “Conceptual Design Report of the CompactLight X-ray FEL”, XLS Deliverable **D2.3** (2021),

[79] I. Agapov et al., “OCELOT: A software framework for synchrotron light source and FEL studies”, Nuclear Instruments and Methods in Physics Research Section A **768**, 151–156 (2014).

[80] B. Marchetti et al., “Experimental demonstration of novel beam characterization using a polarizable X-band transverse deflection structure”, Scientific Reports **11**, 3560 (2021),

[81] M. Borland, "ELEGANT: A Flexible SDDS-Compliant Code for Accelerator Simulation", Technical Report Argonne National Lab (2000),

[82] S. A. Antipov et al., "First start-to-end simulations of the 6 GeV laser-plasma injector at DESY", Proceedings of IPAC2022, 1757–1760 (2022),

[83] J. P. Couperus et al., "Demonstration of a beam loaded nanocoulomb-class laser wakefield accelerator", Nature Communications **8**, 487 (2017),

[84] J. Götzfried et al., "Physics of High-Charge Electron Beams in Laser-Plasma Wakefields", Physical Review X **10**, 041015 (2020),

[85] W. Leemans, "Report of Workshop on Laser Technology for k-BELLA and Beyond", Workshop LBNL, 1–60 (2017),

[86] C. L. Haefner et al., "High average power, diode pumped petawatt laser systems: a new generation of lasers enabling precision science and commercial applications", Proceedings of SPIE **10241**, edited by G. Korn and L. O. Silva, 1024102 (2017),

[87] C. Siders, "New Architectures for PW-Scale High Peak Power Lasers Scalable to Near-MW Average Powers and Their Application to EUV Generation", Proceedings of ALPS (2018),

[88] R. Jonas and I. Peperkorn, priv. comm. 2022.

[89] B. Belusic, priv. comm. 2023.

[90] *PETRA log book*, https://ttfinfo.desy.de/petraelog-sec/index.jsp.

[91] A. Picksley et al., "Guiding of high-intensity laser pulses in 100-mm-long hydrodynamic optical-field-ionized plasma channels", Physical Review Accelerators and Beams **23**, 081303 (2020),

[92] L. Feder et al., "Self-waveguiding of relativistic laser pulses in neutral gas channels", Physical Review Research **2**, 043173 (2020),

[93] M. Dehler et al., "X-band rf structure with integrated alignment monitors", Physical Review Special Topics - Accelerators and Beams **12**, 062001 (2009),

[94] L. Cowie et al., "An X-Band Lineariser for the CLARA FEL", Proceedings of IPAC2018, 3848–3851 (2018),

[95] F. Burkart et al., "The ARES Linac at DESY", Proc. LINAC2022, 691–694 (2022).

[96] H. Schlarb, priv. comm. 2023.

[97] G. Kube, priv. comm. 2022.

[98] https://www.gauss-centre.eu/.

[99] J.-L. Vay, "Noninvariance of space- and time-scale ranges under a Lorentz transformation and the implications for the study of relativistic interactions", Physical Review Letters **98**, 2–5 (2007).

[100] M. Kirchen et al., "Stable discrete representation of relativistically drifting plasmas", Physics of Plasmas **23**, 100704 (2016),

[101] https://github.com/optimas-org/optimas.

[102] E. Bakshy et al., "AE: a domain-agnostic platform for adaptive experimentation", in Advances in neural information processing systems (2018),

[103] S. Hudson et al., "libEnsemble: A library to coordinate the concurrent evaluation of dynamic ensembles of calculations", IEEE Transactions on Parallel and Distributed Systems **33**, 977–988 (2022).

[104] C. E. Rasmussen and C. K. I. Williams, *Gaussian processes for machine learning* (MIT Press, 2006).

[105] A. Ferran Pousa et al., "Wake-T: a fast particle tracking code for plasma-based accelerators", Journal of Physics: Conference Series **1350**, 012056 (2019),

[106] P. Baxevanis and G. Stupakov, "Novel fast simulation technique for axisymmetric plasma wakefield acceleration configurations in the blowout regime", Physical Review Accelerators and Beams **21**, 071301 (2018),

[107] C. Benedetti et al., "An accurate and efficient laser-envelope solver for the modeling of laser-plasma accelerators", Plasma Physics and Controlled Fusion **60**, 014002 (2017),

[108] E. L. Saldin et al., "Radiative interaction of electrons in a bunch moving in an undulator", Nuclear Instruments and Methods in Physics Research Section A **417**, 158–168 (1998).

[109] C. Benabderrahmane et al., "Magnets for the ESRF-EBS Project", Proceedings of IPAC2016, 1096–1099 (2016),

[110] C. Mayes and G. Hoffstaetter, "Exact 1-D Model for Coherent Synchrotron Radiation with Shielding and Bunch Compression", Physical Review Special Topics - Accelerators and Beams **12**, 024401 (2009).

[111] D. Strickland and G. Mourou, "Compression of amplified chirped optical pulses", Optics Communications **56**, 219–221 (1985),

[112] V. Malka et al., "Electron Acceleration by a Wake Field Forced by an Intense Ultrashort Laser Pulse", Science **298**, 1596–1600 (2002),

[113] J. Osterhoff et al., "Generation of Stable, Low-Divergence Electron Beams by Laser-Wakefield Acceleration in a Steady-State-Flow Gas Cell", Physical Review Letters **101**, 085002 (2008),

[114] J. Faure et al., "Controlled injection and acceleration of electrons in plasma wakefields by colliding laser pulses", Nature **444**, 737–739 (2006),

[115] C. G. R. Geddes et al., "Plasma-Density-Gradient Injection of Low Absolute-Momentum-Spread Electron Bunches", Physical Review Letters **100**, 215004 (2008),

[116] A. Pak et al., "Injection and Trapping of Tunnel-Ionized Electrons into Laser-Produced Wakes", Physical Review Letters **104**, 025003 (2010),

[117] C. McGuffey et al., "Ionization Induced Trapping in a Laser Wakefield Accelerator", Physical Review Letters **104**, 025004 (2010),

[118] K. Schmid et al., "Density-transition based electron injector for laser driven wakefield accelerators", Physical Review Special Topics - Accelerators and Beams **13**, 091301 (2010),

[119] A. J. Gonsalves et al., "Tunable laser plasma accelerator based on longitudinal density tailoring", Nature Physics **7**, 862–866 (2011),

[120] B. B. Pollock et al., "Demonstration of a Narrow Energy Spread, 0.5 GeV Electron Beam from a Two-Stage Laser Wakefield Accelerator", Physical Review Letters **107**, 045001 (2011),

[121] C. E. Clayton et al., "Self-Guided Laser Wakefield Acceleration beyond 1 GeV Using Ionization-Induced Injection", Physical Review Letters **105**, 105003 (2010),

[122] X. Wang et al., "Quasi-monoenergetic laser-plasma acceleration of electrons to 2 GeV", Nature Communications **4** (2013),

[123] S. Kneip et al., “Near-GeV Acceleration of Electrons by a Nonlinear Plasma Wave Driven by a Self-Guided Laser Pulse”, Physical Review Letters **103**, 035002 (2009),

[124] K. V. Grafenstein et al., “Laser-accelerated electron beams at 1 GeV using optically-induced shock injection”, Scientific Reports **13**, 11680 (2023),

[125] W. Lu et al., “Generating multi-GeV electron bunches using single stage laser wakefield acceleration in a 3D nonlinear regime”, Physical Review Special Topics - Accelerators and Beams **10**, 061301 (2007),

[126] W. Lu et al., “Limits of linear plasma wakefield theory for electron or positron beams”, Physics of Plasmas **12**, 063101 (2005),

[127] W. Lu et al., “The optimum plasma density for plasma wakefield excitation in the blowout regime”, New Journal of Physics **12**, 085002 (2010),

[128] G.-Z. Sun et al., “Self-focusing of short intense pulses in plasmas”, Physics of Fluids **30**, 526 (1987),

[129] P. Sprangle et al., “Relativistic Self-Focusing of Short-Pulse Radiation Beams in Plasmas”, IEEE Transactions on Plasma Science **15**, 145–153 (1987),

[130] W. K. H. Panofsky and W. A. Wenzel, “Some Considerations Concerning the Transverse Deflection of Charged Particles in Radio-Frequency Fields”, Review of Scientific Instruments **27**, 967–967 (1956),

[131] I. Kostyukov et al., “Phenomenological theory of laser-plasma interaction in “bubble” regime”, Physics of Plasmas **11**, 5256 (2004),

[132] S. A. Yi et al., “Analytic model of electromagnetic fields around a plasma bubble in the blow-out regime”, Physics of Plasmas **20**, 013108 (2013),

[133] W. Lu et al., “A nonlinear theory for multidimensional relativistic plasma wave wakefields”, Physics of Plasmas **13**, 056709 (2006),

[134] S. Bulanov et al., “Particle injection into the wave acceleration phase due to nonlinear wake wave breaking”, Physical Review E **58**, R5257–R5260 (1998).

[135] A. Modena et al., “Electron acceleration from the breaking of relativistic plasma waves”, Nature **377**, 606–608 (1995),

[136] H. Suk et al., “Plasma Electron Trapping and Acceleration in a Plasma Wake Field Using a Density Transition”, Physical Review Letters **86**, 1011–1014 (2001),

[137] M. Tzoufras et al., “Beam Loading in the Nonlinear Regime of Plasma-Based Acceleration”, Physical Review Letters **101**, 145002 (2008),

[138] C. D. Decker et al., “The evolution of ultra-intense, short-pulse lasers in underdense plasmas”, Physics of Plasmas **3**, 2047–2056 (1996),

[139] B. A. Shadwick et al., “Nonlinear laser energy depletion in laser-plasma accelerators”, Physics of Plasmas **16**, 056704 (2009),

[140] E. Esarey et al., “Envelope analysis of intense laser pulse self-modulation in plasmas”, Physical Review Letters **72**, 2887–2890 (1994),

[141] C. Benedetti et al., “Quasi-matched propagation of ultra-short, intense laser pulses in plasma channels”, Physics of Plasmas **19**, 053101 (2012),

[142] G. J. Boyle et al., “Reduced model of plasma evolution in hydrogen discharge capillary plasmas”, Physical Review E **104**, 015211 (2021),

[143] N. A. Bobrova et al., “Simulations of a hydrogen-filled capillary discharge waveguide”, Physical Review E **65**, 016407 (2001),

[144] K. K. Swanson et al., “Cryogenically formed discharge waveguide”, Physical Review Accelerators and Beams **24**, 091301 (2021),

[145] “Beam optics and focusing systems without space charge: sections 3.6 - 3.9”, in *Theory and design of charged particle beams* (John Wiley & Sons, Ltd, 2008) Chap. 3, pp. 103–161,

[146] E. D. Courant and H. S. Snyder, “Theory of the alternating gradient synchrotron”, Annals of Physics **3**, 1–48 (1958).

[147] T. Mehrling et al., “Transverse emittance growth in staged laser-wakefield acceleration”, Physical Review Special Topics - Accelerators and Beams **15**, 111303 (2012),

[148] K. Floettmann, “Some basic features of the beam emittance”, Physical Review Special Topics - Accelerators and Beams **6**, 034202 (2003),

[149] M. Migliorati et al., “Intrinsic normalized emittance growth in laser-driven electron accelerators”, Physical Review Special Topics - Accelerators and Beams **16**, 1–5 (2013).

[150] F. Marteau et al., “Variable high gradient permanent magnet quadrupole (QUAPEVA)”, Applied Physics Letters **111**, 253503 (2017),

[151] A. Ghaith et al., “Permanent Magnet-Based Quadrupoles for Plasma Acceleration Sources”, Instruments **3**, 27 (2019).

[152] J. van Tilborg et al., “Active Plasma Lensing for Relativistic Laser-Plasma-Accelerated Electron Beams”, Physical Review Letters **115**, 184802 (2015),

[153] S. Steinke et al., “Multistage coupling of independent laser-plasma accelerators”, Nature **530**, 190–193 (2016),

[154] C. A. Lindstrøm et al., “Emittance Preservation in an Aberration-Free Active Plasma Lens”, Physical Review Letters **121**, 194801 (2018),

Cover picture: MPA | Plasma Accelerators, DESY

Deutsches Elektronen-Synchrotron DESY
A Research Centre of the Helmholtz Association

Helmholtz contributes to solving major challenges facing society, science, and the economy through top-level scientific achievements in six Research Fields: Energy, Earth and Environment, Health, Information Matter, and Aeronautics, Space, and Transport. With more than 44.000 employees at 18 Research Centers and an annual budget of more than 5 billion euros, Helmholtz is Germany's largest scientific organization.

HELMHOLTZ

www.helmholtz.de